An Experimental Method for the Investigation of Indoor Airflows in a Reduced Scale Model Room: Development and Application

Dissertation
zur Erlangung des akademischen Grades

Doktoringenieur
(Dr.-Ing.)

vorgelegt der
Fakultät für Maschinenbau der
Technischen Universität Ilmenau

von Herrn
Dipl.-Ing. Max Konrad Körner

geboren am 08.12.1981 in Dresden

Gutachter

Prof. Dr. rer. nat. habil. André Thess

Prof. Dr.-Ing. habil. Dr. h. c. Bodo Ruck

Dr. habil. Olga Shishkina

Acknowledgement

Kurzfassung

Eine experimentelle Methode zur Untersuchung von Raumluftströmungen in einem stark verkleinerten Modellraum: Entwicklung und Anwendung

In der vorliegenden Arbeit wurde ein Verfahren zur experimentellen Untersuchung nicht-isothermer Raumluftströmungen in einem stark verkleinerten Modellraum unter Berücksichtigung aller Ähnlichkeitskennzahlen entwickelt. Mit diesem Verfahren konnte erstmals eine sehr hohe Genauigkeit bezüglich der Ähnlichkeitskennzahlen Reynolds-Zahl *Re*, Rayleigh-Zahl *Ra*, Prandtl-Zahl *Pr* sowie der Archimedes-Zahl *Ar* erreicht werden. Die Anpassung der Randbedingungen an den Modellmaßstab erfolgt bei dieser Methode über die Anpassung der Materialeigenschaften eines beliebigen Arbeitsgases durch Erhöhen des Drucks *p*. Dieses Verfahren konnte in der weltweit einzigartigen Experimentieranlage SCALEX (SCALEX = scaled convective airflow laboratory experiment) umgesetzt und auf zwei Beispielproblemstellungen der Raumluftströmung (isotherme sowie gemischte Konvektion) erfolgreich angewendet werden. Dazu wurden die Geschwindigkeitsverteilungen der groß-skaligen Strömungsstrukturen in einem im Maßstab von 1:10 verkleinerten Modellraum hinreichend komplexer Geometrie für den Fall isothermer sowie gemischter Konvektion untersucht. Die Geschwindigkeitsmessungen wurden mit einem 2D-laser Doppler velocimetry System durchgeführt. Als Arbeitsgas wurde Schwefelhexafluorid (SF_6) bei einem Druck von p = 4.517bar verwendet. Die Ergebnisse der vorliegenden Arbeit sowie die neu entstandene Anlage tragen zu einem umfangreichen Verständnis sowie einem vereinfachten experimentellen Zugang zum komplexen Themengebiet der Raumluftströmungen bei.

Abstract

An Experimental Method for the Investigation of Indoor Airflows in a Reduced Scale Model Room: Development and Application

In the present work a new experimental method for the investigation of non-isothermal indoor airflows in a reduced scale model room with respect to the full set of dimensionless numbers has been developed. The method provides a high accuracy with respect to the dimensionless numbers Reynolds number *Re*, Rayleigh number *Ra*, Prandtl number *Pr* and Archimedes number *Ar*. The adjustment of the boundary conditions to the chosen scale is achieved by adjusting the material properties of a working gas by increasing its pressure. The technical realization of this theoretical approach could be demonstrated by setting up the worldwide unique experimental setup, the SCALEX-facility (SCALEX = scaled convective airflow laboratory experiment) and applying it to two exemplary problems (isothermal and mixed convection) of indoor airflow research. For this purpose the velocity distributions of the large-scale flow structures have been investigated in a 1:10 scale model room with sufficient high complex geometry. The velocity measurements were performed using a 2D laser Doppler velocimetry system. Sulfur hexafluoride (SF_6) at a pressure of $p = 4.517$ bar have been used as working gas. The results of the present work as well as the set up SCALEX-facility account for a comprehensive understanding and an easy experimental access to the complex subject of indoor airflow research.

Contents

1 Introduction

Indoor airflows are relevant to the indoor air quality in offices, aircraft cabins or surgery rooms and can influence the ergonomics, security and energy efficiency of a room significantly. Problems concerning indoor airflows has been intensively studied since the 1970's [1–12], which originated a large variety of numerical and experimental investigation methods. But, although indoor airflows obviously have a much higher impact on our daily life than aerodynamic problems, there is no satisfying integrated experimental approach, which allows performing fundamental and applied research as realized in a wind tunnel for aerodynamic problems. The present work contributes to close this lack of methodology in indoor airflow research by introducing a new method permitting experimental research in a room that is reduced in size. The introduced novel method is based on the manipulation of the material properties of a working gas and promises comparable ranges of application and accuracy like the wind tunnel in aerodynamics. In order to support the theoretical approach, the realization of the new method in an experimental setup as well as its first application to a generic room is presented as a result of the present work. The following section 1.1 will give a short overview on the relevance of indoor airflow research. Section 1.2 will show the placement of the work with respect to recent experimental investigation methods and the explicit goals of the work are defined in section 1.3.

1.1 Indoor airflows and thermal comfort

Indoor airflows verifiably influence the wellness and the productivity but also the health of occupants within the room [13–15]. For instance, decreasing the draft risk ([10], [16]) or ensuring a fast removal of pollutions within the air like pathogenic gems [17] guarantees a healthy environment. A very significant feature of indoor airflows in terms of indoor air quality is the thermal comfort. Thermal comfort describes the individual wellness of occupants within a room with respect to their thermal environment. Particularly the heat transfer between the occupants and their environment is significant for thermal comfort. Beside the radiative and conductive heat transfer, the convective heat transfer has the highest impact on thermal comfort. The convective heat transfer again is mainly influenced by the temperature and velocity of the air within the room. But, especially the sensation of the air temperature and velocity is very subjective and depends on a lot of individual factors of each occupant.

So, in order to provide a universally valid measure for the thermal comfort, Fanger introduced several empirical models ([12], [18]) like the predicted mean vote PMV or the draft risk DR. These models were determined through experiments with test persons and are therefore based on velocity and temperature

properties of the flow in the immediate vicinity of the occupant, also called occupied zone. Thus, to determine the empirical values of Fanger and to make exact predictions of the thermal comfort of the room, the exact knowledge of the physical parameters like velocity or temperature of the indoor airflows is necessary. As a result, the determination of these parameters reflects a major goal of indoor airflow research. Moreover, a major aim of indoor airflow research is to answer the question: What are the characteristics of indoor airflows and what causes them?

In general, indoor airflows occur in every room that contains a heat source and a heat sink which produces an unstable temperature gradient. The unstable temperature gradient causes a motion of the fluid within the room, which is known as natural convection. The natural convection is based on the density differences between cold and warm air, which leads in combination with gravity to buoyancy. At sufficient high temperature differences ΔT, the convective flow forms large-scale structures with dimensions of the size of the room [19]. A flow within a room which contains a heated area that does not exceed the height of a cooler area is the simplest scenario of buoyancy driven flows. This type of flow is called Rayleigh-Bénard-Convection (RBC) and is well-known for simple room geometries like cylinders [20–24]. But, the more complex the room geometry or the distribution of the heat sources and sinks the more complex is the flow behavior within the room. For instance, typical heat sources in an office room are radiators, electrical devices or human bodies. Typical heat sinks are windows, doors or insufficiently insulated walls. The highly complex behavior of buoyancy driven indoor airflows can be extended to significantly higher complexity just by the simple operation of switching on a fan. A fan produces a mechanically driven flow, called forced convection, which temporally and spatially superimposes the buoyancy driven flow, the natural convection. This superposition is called mixed convection and makes it difficult or sometimes impossible to make a prediction on the flow behavior until now. But, because most of the indoor airflows, particularly in the transportation sector and in rooms in climate zones with high temperatures, are characterized by mixed convection, a precise prediction of the flow is very important.

However, the knowledge of the mechanisms of indoor airflows is especially based on the knowledge of the correlation between the boundary conditions, e.g. inlet velocity, global temperature difference and room geometry, and the large-scale flow structure. In order to provide correct predictions of the flow for arbitrary rooms, these correlations have to be sufficiently understood. The complexity of the flow and the broad variety of influences are a main reason why the mechanisms of indoor airflows are not sufficiently understood until now [25]. Furthermore, the limited possibility to study the behavior of the flow within the whole room, in particular the limited access to the large-scale flow structures, makes fundamental experimental investigations of indoor airflows very difficult. This is mainly caused by the large room dimensions and by the limitations of common measurement methods. Thus, the development of a new

experimental method for the fundamental investigation of large-scale flow structures in indoor airflows represents a main goal of the present work.

1.2 Recent methods for the investigation of indoor airflows

The methods for the investigation and therefore the prediction of indoor airflows have a broad range starting from analytical ([6], [26]) and empirical models over high performance experiments ([27], [28]) and ending up with high resolved direct numerical simulations (DNS) [29]. According to a review by Chen [30] the empirical and analytical models are methods for global prediction of indoor airflows for design purposes of simple room geometries. These methods are not or limited applicable for the detailed investigation of indoor airflows and are not regarded in the present work. Also zonal models and multi-zone models and its derivatives cannot provide a very detailed view on the flow.

Chen [30] further states, that the most common method for the investigation of indoor airflows are computational fluid dynamics (CFD) methods, which determines the velocity and temperature field of the flow by numerically solving the conservation equations of fluid dynamics, the Navier-Stokes-Equations (NSE). These numerical simulations promise the possibility to investigate every characteristic of indoor airflows in any arbitrary room geometry and for any arbitrary boundary conditions. But, due to the complexity of the NSE, a lot of assumptions have to be made concerning the temporal and spatial resolution and the fluid physics, like turbulence. Thus, the numerical simulations always need experimental data for validation. Moreover, very complex flows in complex domains are very expensive, i.e. it takes a lot of time and computing resources. Thus, CFD methods are of limited suitability for fundamental research of indoor airflows.

A widespread experimental method allowing the detailed investigation of indoor airflows are experimental measurements in the full-scale [30], i.e. the investigation of the flow in rooms of original size. Laboratory full-scale experiments are often conducted in climate chambers equal in size with respect to the prototype, which permits setting up well-controlled boundary conditions. If the size of the room is very large, i.e. comparable to a theater room or an atrium, laboratory full-scale experiments are often substituted by field measurements. Field measurements performed in the prototype room suffer from insufficiently controlled boundary conditions. Furthermore, the laboratory as well as the field measurements cannot provide a comprehensive access to the complete flow field within the whole room, because the currently available flow measurement systems for large measurement volumes of the order of several meters are still at the

beginning of development [31]. In addition, the full-scale experiments do not have the same variability of the boundary conditions like CFD methods have. This makes fundamental research very expensive.

The most promising method, combining high variability of the boundary conditions and high experimental accessibility, are small-scale experiments. Small-scale experiments are performed in a room with reduced size, hereinafter called model room. The high variability is due to the relatively low technical effort, which is again caused by the reduced size of the room and the possibility of applying common measurement techniques, often without any modification. For instance, the variation of the room geometry is very easy, when using a model room. By contrast, in full-scale experiments this would evoke a very high technical effort. Furthermore, small-scale experiments also allow a view on the flow throughout the whole room due to the small dimensions of the room. Moreover, due to the experimental approach, no assumptions have to be made to the physical behavior of the flow as often done in CFD methods. So, the method of small-scale experiments combines the key advantages of the CFD methods and the full-scale experiments.

The major challenge of small-scale experiments is to achieve similar physical behavior of the flow inside the model room with respect to the full-scale prototype, hereinafter called similarity. For aerodynamic problems, this is a well-known method and consequently applied in wind tunnels. There, similar flow conditions can be realized by simply adjusting the approach velocity. Achieving similar physical behavior of the flow in terms of indoor airflows is more complicated, because of the superposition of forced and natural convection. Particularly, the modeling of both convection types at the same time with respect to the reduced size represents a main problem. Consequently, this is the main reason, why small-scale experiments have a rather low significance in indoor airflow research. Although there have been several attempts, there is no satisfying solution for achieving similarity for the case of mixed convection in terms of indoor airflows until now [30].

Hitherto approaches often model similar physical behavior of the flow in the reduced scale by applying working fluids different from air. Thus, the material properties are modified in order to achieve similarity. Until now, the most common working fluid is water, as used in several investigations ([1], [26], [32–34]). Using water as the working fluid allows quite well the modeling of forced convection in the small-scale experiments in order to achieve similarity. Here, the changed density and viscosity have to be regarded, which is also often implemented in water channels for aerodynamic problems. Whereas modeling natural convection in water cannot be achieved by the simple implementation of a heat source without accepting high errors regarding the similarity. This is caused by the huge difference of the material properties between air and water with respect to the heat transfer properties, like thermal conductivity, volume expansion coefficient or the specific heat capacity. Thus, the natural convection due to temperature

4

differences inside the model room is mimicked through concentration differences. As often reported in the open literature, this is mainly realized by using saline-water solutions of different levels of salinity within the same room. In particular, the heat sources are modeled by water with a high level of salinity, the cold inlet flow is model by water of low salinity. The air inside the room is modeled by water with a medium level of salinity. Because the density of the saline-water solution is linearly correlated to the level of salinity, the experiments have to be performed upside-down, as shown by Kaye & Hunt, 2004 [26]. The heat transfer between the heat source and the cool inlet flow is mimicked by diffusion processes. Anyway, although the use of saline-water solutions is able to mimic the heat transfer and the major flow behavior, this approach is only applicable for fundamental research of more or less simple problems. This is mainly due to the fact that the heat sources are only realizable as point sources, which makes realistic heat source distributions impossible. The possibility of performing long term investigations is also very limited due to the fact that the recycling of the saline-solutions has a disproportional high effort. Thus, the development and implementation of a new approach for achieving similarity is another major motivation of the present work.
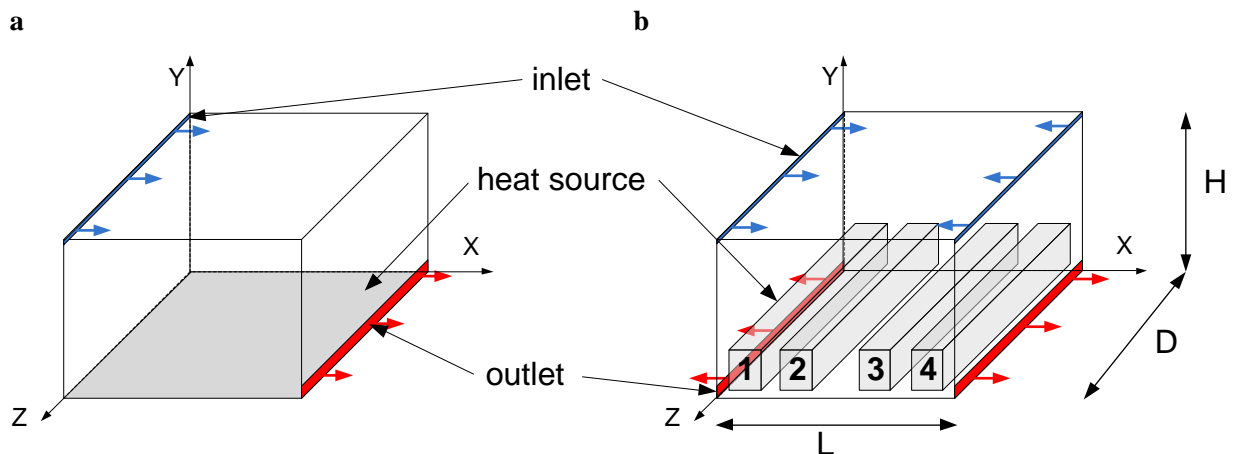
Fig. 1 Comparison between the simple and often used Nielsen room (**a**) and a more complex room used for the investigation in the present work (**b**)

Most studies are carried out in a simplified room, which is often used for the validation of CFD codes on experimental data and moreover for fundamental experimental research in small-scale experiments. This rectangular shaped room, shown in Fig. 1a, comprises one flow inlet at the ceiling and one outlet at the bottom on the opposite side. Furthermore, a heat source is distributed all-over the bottom of the room. This room is often called Nielsen room due to its first introduction by Nielsen in 1974 [1]. But for most cases, the simplification of the room is too high, i.e. the flow behavior found for this room geometry is difficult to apply to real indoor airflow problems. Therefore, a derivative of the Nielsen room, shown in Fig. 1b, is introduced in the present work. The higher complexity of the room arises from the

5

implementation of one additional inlet and outlet on contrariwise positions as in the Nielsen room. The heat source is change from a uniform distributed one to a more discrete distributed one. So, a model room of such complexity regarding its geometry is more comparable to rooms like passenger cabins or conference rooms. Moreover, this complexity has never been applied in small-scale experiment until now, because its realization would be very complicated when using a saline-water solution as working fluid. Thus, the application of this model room geometry seems to be a good measure for testing the capability of the new method introduced in this work.

1.3 The goals of the present work

Indeed, the small-scale experiment seemingly promises to be the most effective multi-purpose method for experimental indoor airflow research. But, the review on hitherto used approaches doubtless shows that the small-scale experiments are limited to relatively simple scientific questions, until now. In order to develop a new approach for small-scale experiments allowing the investigation of fundamental and applied problems of indoor airflows, it is important to answer the following basic questions:

1. Is there a possibility of adjusting the parameters of an arbitrary indoor airflow in order to reach full similarity for any arbitrary scale factor?
2. Can such an approach be realized in a technically feasible experimental setup allowing the usage of common measurement techniques?
3. What are the limits of the new method regarding the parameter range? Or in other words: Is it possible to apply the method to realistic indoor airflow problems, guaranteeing a low effort with respect to the experimental procedure?

With respect to these questions, the main goal of the work is the development of a new methodology for small-scale experiments, which allows achieving full similarity. This new method should allow the investigation of any arbitrary indoor airflow at a broad range of scale factors. Furthermore, the technical feasibility of the new method should be investigated by the development of a novel experimental setup allowing the investigation of the flow velocity within room geometry shown in Fig. 1b for the isothermal and the mixed convection case. The reliability of the found results should be proofed by a comparison with other investigation methods at equal boundary conditions.

The outline of the present work is as follows. Section 2 overviews the most important basics of indoor airflow research, similarity theory and the most common data evaluation methods used in this work.

The novel small-scale method as well as its realization in the experimental setup, which has to be regarded as a main result of the work, is described in section 3. The results of the first application of the new method, the new experimental setup and the introduced model room is described and discussed in section 4. A summary of the findings of the work and an outlook is given in section 5.

2 Basics in describing indoor airflows

2.1 Basic equations describing indoor airflows

Most investigations and subsequent predictions of the before mentioned indoor airflow properties, like *PMV* or *DR*, are based on analyzing the velocity and temperature field of the flow, $\boldsymbol{u} = (u, v, w)$ and T within an arbitrary enclosure with dimensions x, y, z. The velocity and the temperature field can be theoretically described using three conservation laws: the conservation of mass, momentum and energy. Although the theoretical analysis of the conservation laws is not part of the present work, they are the basic mathematical description of the flow behavior. Moreover, they have to be mentioned in order to understand the relevance of the presented and discussed velocity measurements in the following sections. The generic form of the three conservations laws are the Navier-Stokes-equations, which in the case of mixed convection are defined as

$$\nabla \cdot \boldsymbol{u} = 0 \tag{1}$$

$$\frac{\partial \boldsymbol{u}}{\partial t} + \boldsymbol{u} \cdot \nabla \boldsymbol{u} = -\rho^{-1} \nabla p + \nu \Delta \boldsymbol{u} + \boldsymbol{g} \tag{2}$$

$$\frac{\partial T}{\partial t} + \left(\boldsymbol{u} \cdot \nabla \right) T = \kappa \nabla^2 T \tag{3}$$

with $\boldsymbol{u} = (u,v,w)$ as the velocity vector, ρ as the fluid density, t as the time, p as the pressure, ν as the viscosity and $\boldsymbol{g} = (0,0,-g)$ as the gravitational acceleration. When comparing eq. (1)-(3), the velocity field $\boldsymbol{u}$ is obviously the most important property to describe the flow behavior, because it has an impact on each conservation law. In contrast the temperature field only affects the energy conservation law shown in eq. (3). Furthermore, the velocity field contains a scalar and a direction, but the temperature field only contains a scalar. Thus, the determination of the velocity field allows a more detailed characterization of the flow behavior than the temperature field. This issue depicts the major motivation of the conducted velocity measurements of the present work. But, although the velocity field has the major impact on the flow behavior, the description of the temperature field cannot be neglected in order to get the full information of the investigated flow. Thus, the velocity field allows a coarse characterization of the flow behavior but do not allow reliable predictions and a full understanding of the flow.

2.2 Characterizing indoor airflows

Due to the predominant usage of rooms as living rooms, offices or passenger cabins, the characterization of indoor air quality is often very subjective, which is mainly caused by the individual sensation of each occupant. Thermal comfort is a main feature of indoor air quality and therefore a main aspect for the design of ventilation systems [35]. Because of this, the thermal comfort will be determined from the velocity measurements in order to demonstrate the application of the new scaling method to common indoor airflow problems. The tools for describing thermal comfort and the flow properties of indoor airflows are described in following sections 2.2.1 and 2.2.2, respectively.

2.2.1 Thermal comfort

The three most important standard values characterizing thermal comfort are the predicted mean vote (*PMV*), the predicted percentage dissatisfied (*PPD*) and the draft risk (*DR*). All values are based on the findings of Fanger ([12], [18]), that are empirically determined by performing climate chamber experiments with numerous test persons. These found correlations are actually part of several today's standards like DIN EN ISO 7730 or DIN 1946. Further criteria for characterizing thermal comfort are the thermal radiation asymmetry, the vertical room temperature gradient and the humidity limit [35]. The *PMV* is a measure for the subjective sensation of room climate by the occupants. According to a suggestion of ASHRAE (American Society of Heating, Refrigerating and Air-Conditioning Engineers), a classification of different types of thermal sensation can be done in the range of $-3 \leq PMV \leq +3$, where $PMV \leq -3$ stands for cold and $PMV \geq +3$ for hot sensation of the room climate [35]. According to the Fanger-equation [12], the *PMV* is mainly influenced by the heat flow rates of the human body that are again influenced by clothing, activity, transpiration, passive evaporation, convection and thermal radiation. The determination of the PPD is based on the *PMV*-value and reflects the predicted percentage of all room users, which are dissatisfied with the actual room climate [35]. The PPD, which is defined as

$$PPD = 100 - 95 e^{\left(-0.03353 PMV^4 - 0.2179 PMV^2\right)} \tag{4}$$

shows that there are always at least 5% of all room users that are not satisfied with the room climate even if there is an optimal climate with respect to the *PMV*. Although the determination of *PMV* and *PPD* is not a part of the present work, this fact illustrates the subjectivity of thermal comfort quite well. But it also shows the applicability of its quantifications, *PMV* and *PPD*.

The third important quantification of thermal sensation, the draft risk (*DR*), reflects the percentage of room users, which feel uncomfortable due to draft in the draft sensitive body regions of neck and ankle [35]. In 1988, Fanger introduced another empirical determined equation [18], which describes the *DR* and reads as follows

$$DR = \left(34 - \vartheta_a\right)\left(|\overline{\boldsymbol{u}}| - 0.05\right)^{0.6223}\left(3.14 + 0.37|\overline{\boldsymbol{u}}|Tu\right) \tag{5}$$

with ϑ_a as the mean ambient temperature around the occupant, $|\overline{\boldsymbol{u}}|$ as the absolute velocity averaged in time, and *Tu* as the turbulence level, which is a measure for the intensity of the velocity fluctuations. Eq. (5) shows, that not only the temperature and the mean velocity have an influence on the draft risk, but also the turbulence level *Tu* of the flow, which is defined as

$$Tu = \frac{1}{\sqrt{3}}\frac{|\boldsymbol{u}'|}{|\overline{\boldsymbol{u}}|} \tag{6}$$

with $\boldsymbol{u}' = (u',v',w')$ as the fluctuation of the flow velocity around the mean velocity $\overline{\boldsymbol{u}} = (\overline{u}, \overline{v}, \overline{w})$, defined as

$$\boldsymbol{u}' = \boldsymbol{u} - \overline{\boldsymbol{u}} . \tag{7}$$

With respect to eq. (5), high turbulent flows do increase the risk of draft significantly, particularly at high mean velocities $\overline{\boldsymbol{u}}$. From eq. (5), one can also obtain the limits of the flow properties, which lead to $DR = 0$. These are a maximum absolute mean flow velocity of $\overline{\boldsymbol{u}} = 0.05$m/s and a minimum ambient temperature of $\vartheta_a = 34$°C and $Tu = 0$. So, a laminar flow with a maximum velocity of 0.05m/s at a temperature of 34°C would be necessary to guarantee a environment with $DR = 0$.

2.2.2 Stochastic tools for characterizing turbulent indoor airflows

Due to the fact that indoor airflows do occur in large scales of velocity (10^{-2}m/s – 10^{1}m/s), temperature difference (10^{1}K) and room dimensions (10^{0}m – 10^{1}m) they are often turbulent flows. Thus, turbulence is a main feature of the flow behavior of indoor airflows and has to be considered when characterizing the flow behavior. By definition, turbulence describes the stochastic and chaotic, high-frequency fluctuations of the flow properties like velocity, temperature or density around a mean value at constant boundary

conditions [36]. As already stated above, turbulence influences thermal comfort, but it is also mainly responsible for the dispersion of aerosols like dust, harmful substances or pathogenic gems. It is also accountable for higher energy dissipation within the flow, which can affect the energy efficiency of ventilation systems. Beside the ones in eq. (6) and (7), the most common tools for describing properties of turbulent flows are presented in the following in order to provide the basics of the analyzing tools used in the present work. Due to the presented investigation of the velocity field, the tools are all referred to the flow velocity $\boldsymbol{u}$.

Although the global velocity field is often depicted in vector fields, its turbulent behavior is most commonly reflected by distribution functions. Thus, a first tool for characterizing the turbulent behavior of the velocity field $\boldsymbol{u}$ is the probability density functions (PDF) $f(\boldsymbol{u})$, which reads

$$f(\boldsymbol{u}) = \frac{1}{\sigma(\boldsymbol{u})\sqrt{2\pi}} e^{-\frac{1}{2}\left(\frac{\boldsymbol{u}-\bar{\boldsymbol{u}}}{\sigma(\boldsymbol{u})}\right)^2} \tag{8}$$

With $\sigma(\boldsymbol{u})$ as the standard deviation of the fluctuating velocity $\boldsymbol{u}(t)$. Regarding particularly time-discrete measurement data, the PDF can also be described by the frequency distribution. The shape of the distribution allows an insight in the properties of the turbulent flow and can be described by the first few orders of statistical "central" moments. The first statistical moment of the fluctuating velocity $\boldsymbol{u}(t)$ is the mean value defined as

$$\bar{\boldsymbol{u}} = \frac{1}{n}\sum_{i=1}^{n}\boldsymbol{u}_i(t) \tag{9}$$

for discrete values of the velocity as usual for experimental or numerical velocity data. The mean value of the velocity reflects the time average of the flow velocity $\boldsymbol{u}(t)$ and gives information about the position of the distribution functions. Further, the fluctuating velocity $\boldsymbol{u}'(t)$ can be determined out of the mean velocity using eq. (7). The second central moment is the variance,

$$\text{var}(\boldsymbol{u}) = \frac{1}{n-1}\sum_{i=1}^{n}\left(\boldsymbol{u}_i - \bar{\boldsymbol{u}}\right)^2 \tag{10}$$

with n as the number of samples and the standard deviation as its square root,

$$\sigma(\boldsymbol{u}) = \sqrt{\text{var}(\boldsymbol{u})} \tag{11}$$

The standard deviation is a measure for the dispersion of the fluctuating velocity about the mean velocity, i.e. a high standard deviation stands for strong velocity fluctuation $\boldsymbol{u'}$ [37]. Another important tool for describing especially the temporal flow behavior of indoor airflows can be derived from the PDF, which is the correlation function $R(\phi)$ [38]. Especially the auto-correlation function, which is defined as

$$R_{\phi\phi} = \frac{\sum\limits_{i=k+1}^{n} \left(\phi_i - \phi\right)\left(\phi_{i-k} - \overline{\phi}\right)}{\sum\limits_{i=k+1}^{n} \left(\phi_i - \overline{\phi}\right)^2} \tag{12}$$

with $\phi = [u,v,w]$ and k as the time-lag [37], can be used to determine time dependent behavior of the flow, e.g. oscillations of the stationary large-scale flow structures, but can also be used for the determination of the minimum measurement time in order to get statistically independent data. A more detailed view on the oscillations of the flow can be achieved by the usage of the power spectral density (PSD) of the signal. The PSD give information about the frequencies and its amplitude within the fluctuating flow. According to the Wiener-Khinchin theorem [39], the PSD can be derived from the auto-correlation function using a fourier transformation. The most common method is the fast fourier transformation (FFT).

Due to the fact that the investigations of the present work are generally referred to the time-averaged values, $\overline{\boldsymbol{u}} \equiv \boldsymbol{u}$ is used throughout the complete following text.

2.3 Similarity theory

In order to draw conclusions with respect to reality from experiments performed in a small-scale model room, it is necessary to achieve physically similar conditions for both cases. Thus, the boundary conditions of the small-scale experiment, e.g. the inlet velocity, the temperature difference or the material properties of a working gas, have to be adjusted according to the chosen scale. This adjustment can be achieved by using the similarity theory, which is systematically introduced in the following and represents the main theoretical background of the present work.

A basic characterization of every flow type can be done by using a set of dimensionless numbers Π_i ($I = 1, 2, ..., p$). Here, a dimensionless number is the product of characteristic physical variables, which are necessary for describing the flow. The minimal number of dimensionless numbers $\Pi_{p \to min.}$, which is

relevant for the flow, can be determined using the *Π*-theorem, which was first formulated by Buckingham in 1914 [40]. In order to setup the *Π*-theorem, it is necessary to find the characteristic physical variables, which are important for the flow. The variables important for indoor airflows in the case of mixed convection are the inlet velocity $u = u_{in} = (u_{in}, 0, 0)$, the characteristic length L (usually the height of the room), and the temperature difference ΔT, the gravity acceleration g and the working gas properties density ρ, dynamic viscosity η and volume expansion coefficient β. They form the mathematical-physical relation

$$f\left(u, L, \Delta T, \rho, \eta, \beta, g\right) = 0 \tag{13}$$

According to Herwig, 2006 [41], if ρ = const. and η = const. within the fluid volume the influence of the thermal conductivity λ and the specific heat capacity c_p on the flow can be neglected as characteristic variables. Thus, the equation (13) gives $n = 7$ characteristic physical variables. All variables can be described by the $k = 4$ fundamental physical quantities: time, mass, length, and temperature. The minimum number of dimensionless numbers in order to characterize indoor airflows in the case of mixed convection can be determined as follows:

$$p = n - k = 7 - 4 = 3 \tag{14}$$

With respect to the Π-theorem and eq. (14), the flow in case of mixed convection can be characterized by $p = 3$ dimensionless numbers. These dimensionless numbers are the Reynolds number Re, the Rayleigh number Ra, and the Prandtl number Pr, which are defined as follows:

$$Re = \frac{\rho u L}{\eta} \tag{15}$$

$$Ra = \frac{\rho^2 c_p \beta g \Delta T L^3}{\eta \lambda} \tag{16}$$

$$Pr = \frac{\eta c_p}{\lambda} \tag{17}$$

13

The Reynolds number *Re* describes the relation between inertia and viscous forces [42] and is in the case of mixed convection a measure for characterizing forced convection. By contrast, the Rayleigh number *Ra*, which can be regarded as the relation between buoyancy and viscosity forces, can be used for characterizing the thermal convection. The Prandtl number *Pr* depicts the relation between thermal diffusivity and momentum diffusivity.

Another important and widely used dimensionless number for characterizing mixed convection is the Archimedes number *Ar*, which reads as follows:

$$Ar = \frac{Ra}{PrRe^2} = \frac{\beta g \Delta T L}{u^2} \, .$$

(18)

In simple terms and with respect to indoor airflows, the Archimedes number describes the relation between natural and forced convection. If $Ar = 1$, natural and forced convection have the same influence on the flow. Consequently, the flow is dominated by forced convection if $Ar < 1$ and by natural convection if $Ar < 1$. The characterization of the room geometry can be realized by the relation between the height and the characteristic horizontal dimension of the room, called aspect ratio Γ, which is defined as

$$\Gamma = \frac{H}{D}$$

(19)

with H as the height of the room and D as one of the horizontal dimensions of the room. In order to fully characterize the room it is necessary to specify every main aspect ratio, i.e. for a rectangular room in direction of the width and the length of the room. The dimensionless numbers can provide a characterization of the flow, e.g. whether the flow is turbulent or not. But they also provide the possibility of comparing flows with each other. Such a comparison is very important in indoor airflows, because the variety of rooms is very broad. But as a main aspect, similar flows in a small-scale model room and its prototype can be achieved, if the full set of dimensionless numbers agrees in both, the prototype (I) and the model room (II).

$$\frac{\Pi_{\mathrm{I,i}}}{\Pi_{\mathrm{II,i}}} = 1$$

(20)

With $\Pi_{I,i}$ and $\Pi_{II,i}$ as the set of dimensionless numbers of the prototype and the model room, eq. (20) is the basic definition of the similarity theory. Thus, to achieve similarity between the model room and the prototype, the physical variables of the model room have to be adjusted to reach equal dimensionless numbers. If only parts of the minimal set of dimensionless numbers fulfill eq. (20) only partial similarity [41] exists.

Indeed, the similarity theory allows comparing results from different independent experimental and numerical studies of indoor airflows. But more important, the similarity theory allows adjusting the boundary conditions of a small-scale experiment with respect to its prototype in order to perform precise investigations. Moreover, the similarity theory is the basis for applying the found results of the small-scale experiment to the reality.

3 Development of the new method and its technical realization

3.1 The model room

A sketch of the rectangular x-y-cross-section of the investigated model room, which was introduced in section 1.2, is depicted in Fig. 2a. The model room is equipped with two inlets in the side walls and close to the ceiling of the room. Two outlets are arranged in the same side walls like the inlets but at the bottom of the room. Four rectangular heating elements are near the bottom of the room. This geometry is extended over the full depth D. The origin of the coordinate system is defined in the left, lower corner with the x-direction along the length L, the y-direction along the height H and the z-direction along the depth D. The model room has a length of $L = 400$mm, a height of $H = 300$mm and a depth of $D = 500$mm. Thus, the aspect ratios of the model room are $\Gamma_{xy} = L/H = 1.33$ and $\Gamma_{zy} = D/H = 1.67$. The inlets has a size of $h_{in}/H = 0.0067$ and $h_{out}/H = 0.05$. The inlets and outlets have the same depth as the model room ($d_{in}/D = d_{out}/D = 1$). The heating elements within the room have a cross-section of $h_{HE}/H = 0.2$ and $l_{HE}/L = 0.1$ and are arranged at the positions $x/L = [0.1, 0.3, 0.6, 0.8]$ related to the origin and the left side of the heating elements in Fig. 2a. The distance from the bottom is equal to the height of the outlet $h/H = h_{out}/H$. The depth of the heating elements is almost of the same size as the depth of the model room. Only a small gap of $d/D = 0.01$ at each side of the model room exists.
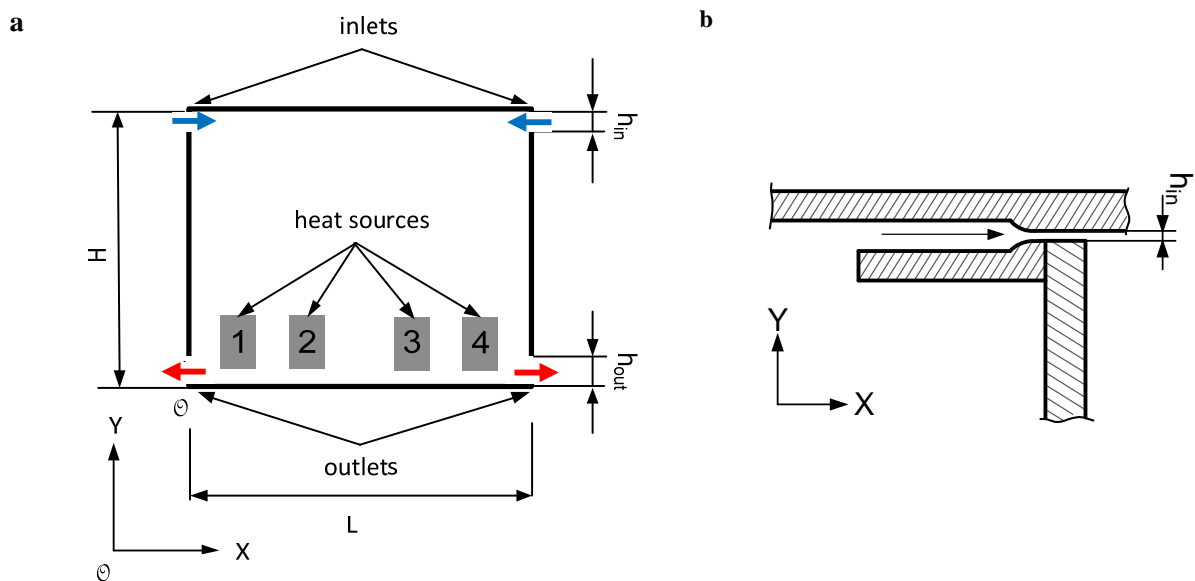
Fig. 2 a Dimensions of the model room geometry in the x-y-cross-section; **b** Shape of the inlet nozzle

As depicted in Fig. 2b and Fig. 3a, a nozzle and prechambers in front of the inlets shall provide a uniform velocity distribution in *y*- and *z*-direction. A characteristic of the prechambers found during pretests of the model room is the occurrence of large-scale flow structures that disturb the homogeneity of the velocity distribution along the z-axis, i.e. the flow in the middle of the inlet is slightly reduced in comparison to its boundaries. In order to realize a fully homogeneous inlet flow it is necessary to disturb the large-scale flow structures inside the prechambers. This is realized by implementing deflector plates directly in front of the inlet opening of each prechamber. As shown in Fig. 3b the model room is made of Plexiglas and the heating elements are made of aluminum. The wall thickness of the Plexiglas is 8mm. The usage of Plexiglas allows optically accessing the complete model room, which reflects a major advantage of small-scale experiments.
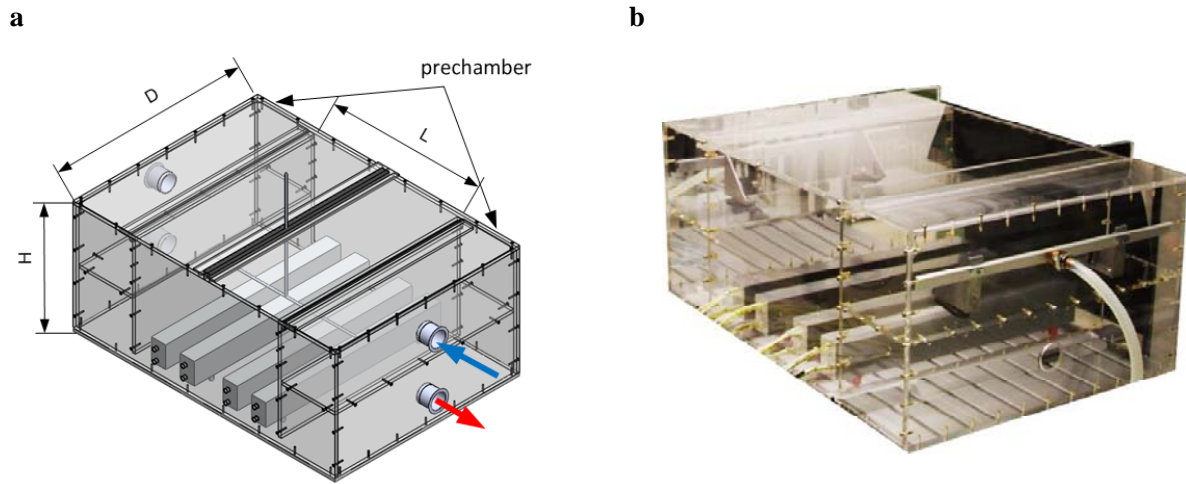
Fig. 3 a 3D Schematic of the model room showing the realistic shape; **b** photography of the model room in the laboratory at Ilmenau University of Technology

3.2 Application of the similarity theory

According to section 2.3, the similarity theory is the basis to setup and perform small-scale experiments. The geometric scale *m* is defined as the ratio between the geometric dimensions of the prototype (I) in the full-scale and the model room (II):

$$m = \frac{L_{\mathrm{I}}}{L_{\mathrm{II}}} \tag{21}$$

with L_I as a characteristic length of the prototype and L_{II} as the one of the model room. The scale *m* has to meet every dimension of the room and has to be regarded for balancing the dimensionless numbers

between the model room and its prototype. Here, balancing means a compensation of the scale m by adjusting the parameters of the dimensionless numbers to meet the requirement of the similarity theory in eq. (20). However, for the case of mixed convection the similarity theory is fulfilled when

$$\frac{Re_I}{Re_{II}} = 1 \tag{22}$$

$$\frac{Ra_I}{Ra_{II}} = 1 \tag{23}$$

$$\frac{Pr_I}{Pr_{II}} = 1 \tag{24}$$

According to eqs. (15) - (17), these relations can be expanded to

$$\left(\frac{\rho_I}{\rho_{II}}\right)\left(\frac{\eta_{II}}{\eta_I}\right)\left(\frac{u_I}{u_{II}}\right)\left(\frac{L_I}{L_{II}}\right) = 1 , \tag{25}$$

$$\left(\frac{\rho_I}{\rho_{II}}\right)^2\left(\frac{\beta_I}{\beta_{II}}\right)\left(\frac{c_{p,I}}{c_{p,II}}\right)\left(\frac{\eta_{II}}{\eta_I}\right)\left(\frac{\lambda_{II}}{\lambda_I}\right)\left(\frac{g_I}{g_{II}}\right)\left(\frac{\Delta T_I}{\Delta T_{II}}\right)\left(\frac{L_I}{L_{II}}\right)^3 = 1 , \tag{26}$$

$$\left(\frac{\eta_I}{\eta_{II}}\right)\left(\frac{c_{p,I}}{c_{p,II}}\right)\left(\frac{\lambda_{II}}{\lambda_I}\right) = 1 . \tag{27}$$

The eqs. (25) - (27) reflects that the possible parameters for balancing the dimensionless numbers are the temperature difference ΔT, the inlet velocity u_{in} or the material properties ρ, λ, η, β and c_p. Changing the gravity acceleration g should be neglected from the outset due to the very high technical effort especially for achieving significant high scale factors m. The most significant dimensionless number for determining the balancing parameters should be that one, for that the scale has the highest impact. Regarding eq. (21) and eqs. (22) - (27), the scale m has the highest impact on the Rayleigh number, because

$$\frac{Ra_I}{Ra_{II}} \propto m^3 \, .$$
(28)

Thus, the Rayleigh number Ra is used for the determination of the parameters for balancing the dimensionless numbers.

With respect to eq. (28), balancing Ra for the aspired scale $m = 10$ would imply to compensate a factor of 1000 in order to meet the similarity. The usage of the temperature difference ΔT for the compensation could not be realized due to very high temperature differences in the range of $10^3 K \leq \Delta T \leq 10^4 K$. In fact, it is more applicable changing the material properties of the working fluid, especially the density ρ, to balance the geometrical scale m.

In order to reduce the effort for the estimation of the correct balancing parameters with respect to eq. (21), the following assumption has to be made

$$\left[\left(\frac{\beta_I}{\beta_{II}} \right), \left(\frac{c_{p,I}}{c_{p,II}} \right), \left(\frac{\eta_{II}}{\eta_I} \right), \left(\frac{\lambda_{II}}{\lambda_I} \right), \left(\frac{g_I}{g_{II}} \right), \left(\frac{\Delta T_I}{\Delta T_{II}} \right) \right] \equiv 1$$
(29)

Consequently, the relation between the chosen balancing parameter ρ and the scale m can be obtained as

$$\frac{\rho_I}{\rho_{II}} = m^{-\frac{3}{2}}$$
(30)

This relation is the basis for estimating the needed working fluid and experimental technique according to the scale factor m for balancing the minimum set of dimensionless numbers.

To balance the scale m for isothermal flows, only the Reynolds number has to be considered. Thus, the Reynolds number relation has a linear proportionality with respect to the scale m, which reads

$$\frac{Re_I}{Re_{II}} \propto m \, .$$
(31)

Therefore, the balancing can be realized by linearly adjusting the inlet velocity u_{in} in accordance to the scale m. That means that the aspired scale $m = 10$ can be reached by increasing the inlet velocity of the model room by a factor of 10 with respect to the prototype.

3.3   Determination of the working gas properties

According to eq. (30) and the aspired scale factor $m = 10$, the density relation between the model room and its prototype can be coarsely estimated for the case of mixed convection to

$$\frac{\rho_{II}}{\rho_I} = m^{\frac{3}{2}} = 10^{\frac{3}{2}} \approx 31.62 \,. \tag{32}$$

That means that for achieving physical similarity the working fluid in the 10-times smaller model room should have an approximately 30-times higher density compared to the prototype. For balancing the Reynolds number Re in the case of mixed convection the determined density relation in eq. (30) and the assumptions made in eq. (29) will give the relation between the inlet velocities of the model room and the prototype as follows

$$\left(\frac{u_{II}}{u_I} \right) = m^{-\frac{1}{2}} \tag{33}$$

With $m = 10$ this will give

$$\left(\frac{u_{II}}{u_I} \right) = 10^{-\frac{1}{2}} \approx 0.32 \,. \tag{34}$$

That means for achieving similarity with respect to the Reynolds number in the case of mixed convection a 3-times lower inlet velocity is necessary.

The obtained scaling of the density and the inlet velocity is only an approximation for the choosing of the scaling technique and the working fluid. Detailed scaling factors of the variables of the dimensionless numbers can only be determined with the knowledge of detailed material properties of the chosen working fluid.

Most prototypes are using air as the working fluid with $\rho \approx 1.3 \text{kgm}^{-3}$ at $p \approx 1\text{bar}$. So, in order to achieve a 30-times higher density and with respect to the equation of state of an ideal gas

$$\rho = \frac{p}{RT} \tag{35}$$

with p as the working gas pressure, R as the specific gas constant and T as the working gas temperature, it is most applicable to use a compressed gas as working fluid. In principle this works with every gas. Using air as the working gas, the pressure has to be increased up to $p \approx 30\text{bar}$ to achieve a 30-times higher density. This relatively high pressure would cause very expensive equipment and high efforts for conducting the small-scale experiments, because the use of special customized measurement equipment would become necessary. Thus, choosing a gas being different from air, which allows achieving the required density relation at lower pressures, would be more promising.

Beyond the maximum needed pressure, further aspects like price and safety has to be considered for choosing a suitable working gas. To avoid high pressures it is most applicable to choose a gas with a high density at normal pressure, for instance Xenon (Xe). Although Xenon indeed fits the requirements concerning the thermo-physical properties, it is also a very expensive gas. Also Radon (Rn) would theoretically fit the thermo-physical requirements, but this gas is radioactive and therefore difficult to handle. Though there is a broad variety of fitting gases, a lot of gases are either very expensive or difficult to handle. Another very important aspect is the availability of detailed information of the material properties in order to allow calculating the required working gas pressure. Sulfur hexafluoride (SF_6) is one of the gases, which achieve the requirements with a comparable low effort and acceptable costs. Furthermore, SF_6 is a gas, which has one of the highest densities at normal conditions ($p = 1\text{bar}$, $T = 273.15\text{K}$), i.e. the necessary pressure to achieve a 30-times higher density should be comparably low. But although SF_6 is a non-toxic gas and has almost properties of an inert gas, it has to be handled with caution due the global-warming potential (GWP) of SF_6 of GWP = 22800 (for 100 years), which is the highest one calculated by the intergovernmental panel on climate change (IPCC) in 2007 [43]. Another suitable working gas is Octafluoropropane (C_3F_6), which is often used as refrigerant under the name R218. Its density at normal conditions is slightly higher than the one of SF_6, thus the needed pressure should be lower. The reactivity of R218 is comparable to that of SF_6 but it has a lower GWP index of 7000. So, both gases would be suitable for realizing the similarity requirements of the present work. Nevertheless SF_6 is the preferred working gas, because in contrast to the use of R218 there exist extensive experience in using SF_6 as working gas for the investigation of convective airflows as documented in references [44–47].

To determine the correct working pressure p it is necessary to use precise data of the thermo-physical material properties, which are involved in the Rayleigh number Ra for the prototype and the model room. Considering the material properties of eq. (26) as a function of the working pressure p yields

$$\left(\left(\frac{\rho_I(p_0)}{\rho_{II}(p)}\right)^2 \frac{\beta_I(p_0)}{\beta_{II}(p)} \frac{c_{p,I}(p_0)}{c_{p,II}(p)} \frac{\eta_{II}(p)}{\eta_I(p_0)} \frac{\lambda_{II}(p)}{\lambda_I(p_0)}\right)^{\frac{1}{3}} = m^{-1} \tag{36}$$

with p_0 as the working pressure of the prototype. This will give a functional correlation $p = f(m)$. Therefore, the pressure dependent material properties $\rho(p)$, $\beta(p)$, $\eta(p)$, $\lambda(p)$, $c_p(p)$ at a constant temperature T has to be calculated for the working gas of the model room and the prototype. Then, the pressure dependent material properties has to be applied to eq. (36). Using a fit function for $p = f(m)$ allows calculating the exact working gas pressure at $m = 10$.

The determination of the material properties is mainly based on empirical equations, which are available in the open literature. In order to simplify the calculation, air is assumed to be an ideal gas with zero humidity, which is also called dry air. Thus, the ideal gas law can be used for the calculation of the density and the volume expansion coefficient yields $\beta = 1/T$. The findings of Kadoya et al.,1985 [48] are used for determining the heat conductivity λ and the dynamic viscosity η as functions of p and T. The calculation of the specific heat capacity c_p as a function of p and T is based on the findings of Lemmon, 2000 [49]. The material properties of SF_6 are calculated using the findings of the references [50–52]. Guder and Wagner [52] provide an equation for the density ρ and the specific heat capacity c_p which is based on a multi-parameter equation of state. The heat conductivity λ and the dynamic viscosity η are calculated by fit functions of measurement data determined by Kestin & Imaishi, 1985 [50] and Hooghland et al., 1985 [51], respectively. The volume expansion coefficient of SF_6 is calculated using

$$\beta = \frac{1}{\rho(T)}\left(\frac{\Delta\rho*}{\Delta T*}\right), \quad \text{with } \Delta\rho* = \rho(T + \Delta T*) - \rho(T), \ \Delta T* = 0.5\text{K}. \tag{37}$$

The density difference $\Delta\rho*$ needed for the calculation of β has been determined by using the multi-parameter equation of state of Guder & Wagner, 2009 [52]. Due to its complexity, the calculation of the pressure and temperature dependent material properties of dry air and SF_6, $[\rho, \beta, \eta, \lambda, c_p] = f(p, T)$, is shifted to the appendix of this work. The material properties of R218 are taken from the open access NIST WebBook of Chemistry for isothermal properties with $T = 296.9\text{K}$, $1\text{bar} \leq p \leq 10\text{bar}$ and $\Delta p = 1\text{bar}$ [53].

Fig. 4 depicts the summary of the determination of the working pressure p as a function of the scale m. The material properties are evaluated at pressures of 1bar $\leq$ p $\leq$ 10bar and at the mean temperature between the aspired temperatures of the inlet flow and the heating elements for the case of mixed convection $T = T_h - T_c = 0.5 \cdot (300.65K - 293.15K) = 296.9K$. The reference for the scale m is air at $T = 296.9K$ and $p = 1$bar. The data points in Fig. 4 reflect the calculated scale m with respect to eq. (36).
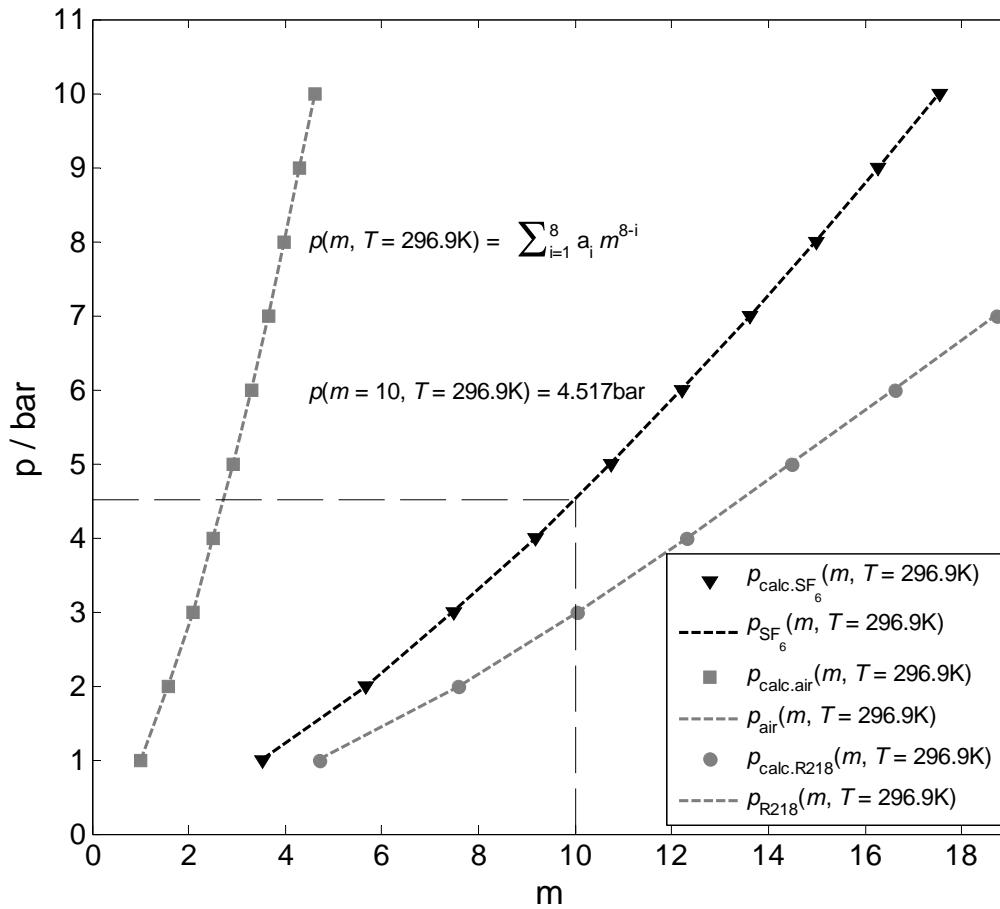
Fig. 4 Determination of the necessary pressure p for achieving the chosen scale factor m at the temperature $T = 296.6K$

Fig. 4 approves the previously made estimation that air is not applicable to achieve scales $m > 4$ with a moderate technical effort. But due to the steep slope the working gas air allows adjusting the material properties in the range of $1 \leq m \leq 4$ more precisely with respect to SF$_6$ or R218. Using SF$_6$ as the working gas the necessary working pressure can be determined by an empirical function for $p = f(m, T)$. As inferred from the data points of Fig. 4, the pressure p has a seventh-order polynomial dependence on the scale m, which reads

$$p(m,T) = \sum_{i=1}^{8} a_i m^{8-i} \tag{38}$$

with the coefficients a_i given in Tab. 1. For the scale factor of $m = 10$ and the mean temperature $T = 296.9K$, the function yields $p(m = 10, T = 296.9K) = 4.517bar$.

$a_1 =$	-6.6412×10^{-4}
$a_2 =$	0.0492
$a_3 =$	-1.6277
$a_4 =$	32.5802
$a_5 =$	-450.4602
$a_6 =$	5.5235×10^3
$a_7 =$	1.5004×10^4
$a_8 =$	-5.7388×10^3

Tab. 1 Coefficients of $p(m, T = 296.9K)$ according to eq. (38)

So, SF$_6$ at a pressure of $p = 4.517bar$ and a temperature of $T = 296.9K$ allows achieving similarity for the scale $m = L_I/L_{II} = 10$ according to eq. (23). The Reynolds number has to be adjusted through the inlet velocity u_{in}. The inlet velocity u_{in} for the determined material properties of SF$_6$ amounts to

$$\frac{u_{in.II}}{u_{in.I}} = \frac{\rho_I^{air} \eta_{II}^{SF_6}}{\rho_{II}^{SF_6} \eta_I^{air}} m = 0.3891 . \tag{39}$$

The Reynolds numbers can be fully balanced with respect to eq. (22) by decreasing the inlet velocity $u_{in.II}$ to $0.3891 \cdot u_{in.I}$. The found velocity relation for the chosen working gas is slightly higher regarding the estimation made in eq. (34). The Prandtl number Pr cannot be balanced by any value in order to achieve similarity, because it only depends on the material properties of the working gas. The Prandtl number of SF$_6$ at $p = 4.517bar$ and $T = 296.9K$ yields $Pr = 0.905$ and is thus slightly higher than the one of the prototype $Pr = 0.712$. However, the similarity theory requirement is fulfilled regarding the Rayleigh number and the Reynolds number but has slight deviations with respect to the Prandtl number. Thus, it can be concluded that using compressed SF$_6$ provides nearly full similarity with moderate technical efforts for realizing the experimental setup and conducting the measurements.

3.4 Experimental setup for the investigation of mixed convection in a scaled down model room

3.4.1 Requirements of the experimental setup

According to the findings of section 3.3, equipment for increasing the pressure p of the working gas SF_6 is needed. Thus, the setup facility must comprise a pressure vessel. A SF_6 service device is needed in order to adjust the necessary pressure p and to handle the environmentally risky and costly SF_6. Furthermore, to conduct experiments of mixed convection within a small-scale model room inside the facility, several supply and measurement systems are required. That means the setup facility mainly consists of three parts, the pressure vessel, the SF_6 service device and the general measurement and supply system (GMSS).

The most important requirement of the pressure vessel is that it has to allow the integration of a 1:10 model room. Assuming a normal prototype with a size of the order of 10^0m, the pressure vessel should therefore allow containing a model room with a size of the order of 10^{-1}m. Furthermore, the pressure vessel must at least resist the working pressure $p = 4.517$bar and should have connections to the working gas supply systems. It also must comprise a door along with an easy access for integrating the model room. The pressure vessel should have the ability to use external power and coolant supplies as well as data acquisition systems to remotely operate the model room within the vessel, i.e. there have to be some feedtroughs of electrical power and coolants but also for sensor data. In order to conduct measurements of the flow velocity using optical measurement techniques like laser Doppler velocimetry (LDV) or laser light-sheet systems from the outside of the vessel, an optical access to the model room within the pressure vessel is required. Because most of the optical flow measurement techniques are based on the usage of particles, the pressure vessel must allow implementing particles to the flow.

The SF_6 service device must allow setting up the needed working gas pressure p inside the pressure vessel. Therefore, the SF_6 service device has to be connected to the pressure vessel and must comprise a pump to achieve the necessary pressure of the working gas. The reuse of the SF_6 is very important due to environmental and financial issues, which is why the service device has to prevent the contamination of the working gas. Thus, the device must allow the evacuation of the pressure vessel, i.e. the ambient air has to be removed from the pressure vessel. Moreover, the service device must contain a storage vessel and at least a simple filter system to remove impurities like dust or humidity from the working gas.

In order to setup stable working gas material properties the GMSS should allow to collect and store time-resolved pressure and temperature data of the working gas inside the pressure vessel. Furthermore, it

should be possible to control the temperature of the working gas in order to guarantee stable gas properties. While the requirements for setting up stable gas properties are always the same for every experiment, the following requirements of the general supply system regarding the operation of the model room are only valid for the case documented in the present work. However, for the operation of the model room several supply devices and measurement systems are required. The GMSS have to comprise power supplies for operating the heating elements and the fan. A cooling system is needed for tempering the inlet flow. Several temperature sensors are necessary in order to collect and store time-resolved data, mainly for control purposes. So, the experimental setup has to fulfill manifold requirements, which necessitate a longsome engineering process and a precise integration of all systems. Due to the complexity of the engineering process, the present work only contains the successful fulfillment of the requirements as described in the following.

3.4.2 Result of the development process – the SCALEX-facility

All the above discussed requirements are realized in the SCALEX-facility (SCALEX = scaled convective airflow laboratory experiment) as depicted in Fig. 5 and Fig. 6. The setup of the SCALEX-facility is based on a patent by Thess & Wagner, 2007 [54] and represents a major result of the present work. Its technical details are described in the following.
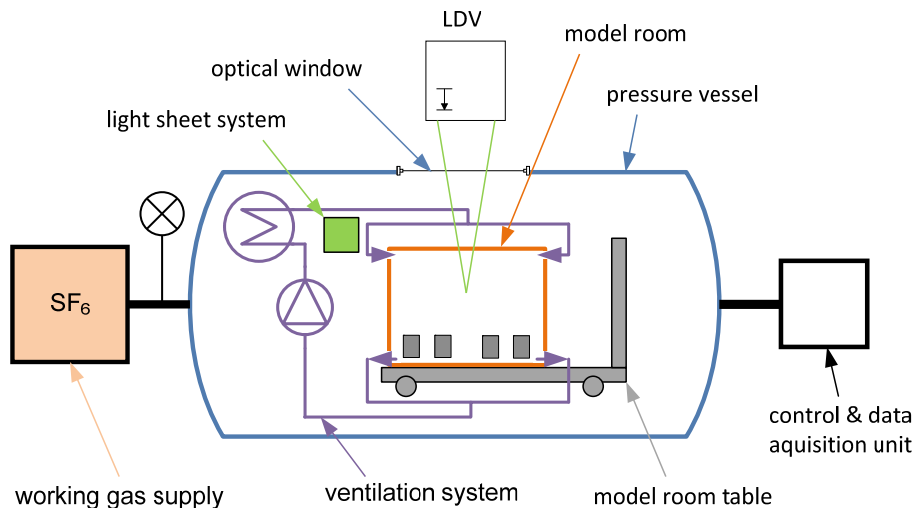
Fig. 5 Schematic of the experimental setup of the SCALEX-facility with the model room inside the pressure vessel and the laser Doppler velocimetry (LDV) system in front of one of the side windows
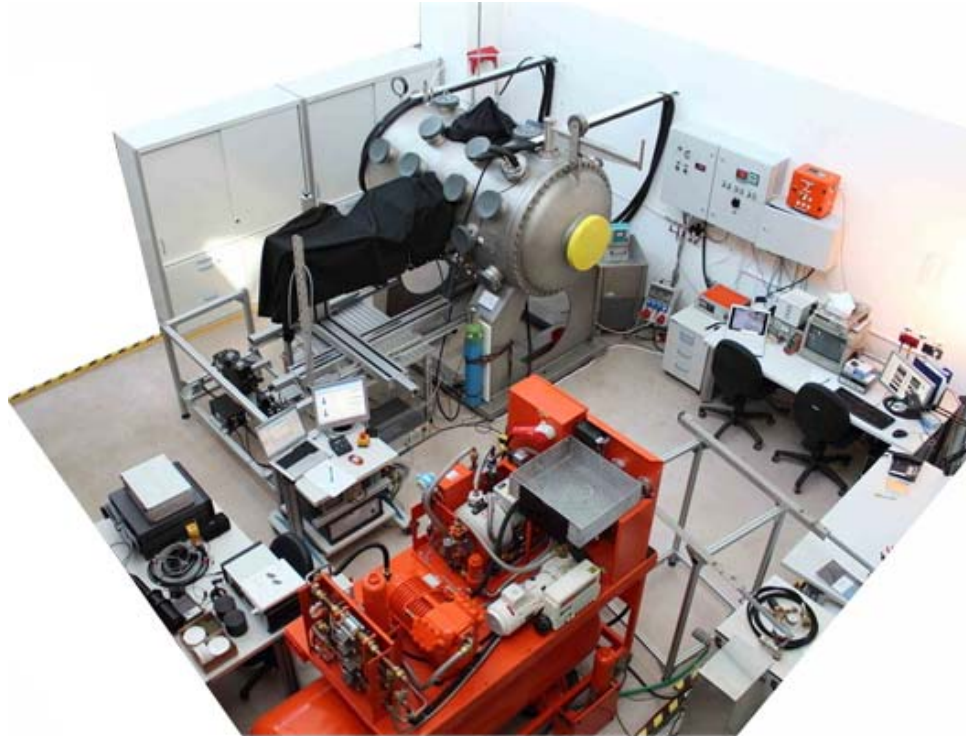
Fig. 6 Overview photography of the SCALEX-facility at the Ilmenau University of Technology

The pressure vessel, manufactured by F. W. Heider GmbH, is made of stainless steel and has a cylindrical shape with a volume of $V \approx 1.5\text{m}^3$ and a diameter of $d = 1\text{m}$. The vessel resists a maximum relative pressure of $p = 10\text{bar}$ and can be operated with air and SF_6 as well. There are two closure heads at each side of the cylinder. One of these closure heads is permanently closed and has the purpose to allow an expansion of the pressure vessel with an additional vessel to perform experiments in very long model rooms, e.g. a full passenger cabin of an aircraft. The other closure head can be opened like a door. Through this door the inside of the pressure vessel is accessible. Inside the pressure vessel there is a rail system, which allows an easy mounting and maintaining of the model room and its supply devices. Several interfaces for the optical access and the operation of the model room, particularly feedthroughs for coolants and electricity, are integrated in the walls of the pressure vessel. The electrical feedthroughs consist of a plate made of steel containing several pins casted in glass. The feedthroughs are mounted in the side wall of the pressure vessel and separated into three types: one feedthrough for the electrical signals of the sensors (152pins), one for low electrical energy and direct current (40pins) and one high power feedthrough for alternating current (24 pins). The main reason for the separation of the electrical feedthrough is the electromagnetic compatibility (EMC). The EMC was the major electrical problem when setting up the facility with respect to a sufficient interference suppression of the sensor signals.

As indicated in Fig. 5 and Fig. 6, the usage of optical flow measurement systems can be realized through five windows with a diameter of $d = 300\text{mm}$ and a thickness of $t = 40\text{mm}$ integrated within the side walls

of the pressure vessel. Additional optical access is based on 30 small windows with the diameter of $d = 150$mm and a thickness of $t = 19$mm. All windows are made of pressure-resistant borosilicate glass, manufactured by TGI GmbH, and are distributed all over the pressure vessel. As shown in Fig. 6, the windows have to be shaded in order to exclude the ambient light inside the pressure vessel, which is important for doing laser light-sheet visualizations. However, the small windows as well as the electrical system and the cooling supply are designed to enable an easy modification to implement a variety of other experiments. This feature allows performing different scientific projects at the same time within the SCALEX-facility.

The working gas SF_6 can be applied to the pressure vessel by the SF_6 service device Economy B120R21 by Dilo GmbH. It comprises a SF_6 storage vessel with a volume of 1m³ and resists a maximum pressure of $p = 25$bar. If the pressure vessel is filled with ambient air, the evacuation is then realized with a vacuum pump. Before filling the pressure vessel with SF_6 a pressure of $p \leq 1$mbar has to be reached. After reaching the SF_6 equilibrium pressure between the pressure vessel and the storage vessel, a compressor is used to achieve the needed pressure of $p = 4.517$bar. The SF_6 service device allows adjusting the pressure inside the pressure vessel by manually operating its pressure reducing valve. Here, the pressure reducing valve is also used for controlling the maximum rate of pressure rise, which is import for avoiding strong temperature rise due to compression of the working gas. Finer adjustment of the pressure is realized through the pressure reducing valve of an additional SF_6 gas cylinder which is additionally connected to the pressure vessel. In order to avoid a contamination of the SF_6 with impurities, e.g. oil, the SF_6 is always filtered before storing it into the storage vessel. The storing of the SF_6 is then realized with the compressor and an additional gas pump. For the usage of air as the working gas in the pressure vessel, compressed air is taken from a compressor which is installed in the laboratory hall. In order to avoid oil deposits inside the vessel, which are caused by the compressor, the air is filtered before entering the pressure vessel. The filtration is realized by using two filters of coarse and fine pore size that in addition comprises a pressure reducing valve, which also allows controlling the maximum rate of pressure rise.

The SCALEX control system comprises a NI PXI1033 chassis with the digital multimeter (DMM) NI PXI 4071 and the switch-matrix-module NI PXI 2533 by National Instruments. The PXI-system is connected to a standard personal computer and controlled by the LabView-based software called SCALEX-OS. This software has been developed during the build-up of the SCALEX-facility. The purpose of the SCALEX control system is the time-resolved acquisition of the temperature and pressure data and the monitoring and controlling of the auxiliary devices.

The pressure is measured with a pressure transducer and two manometers. One of the manometers is mounted on the pressure vessel and one is mounted within the SF$_6$ service device. The manometers are used for coarsely control the pressure inside the pressure vessel. The pressure sensor is used to measure the pressure more precise for the adjustment of the working pressure and for time-resolved monitoring during the measurements. The pressure transducer is the Cerabar T PMC131 by Endress & Hauser GmbH, which works with a ceramic sensor, a measurement range of $0\text{bar} \leq p \leq 10\text{bar}$ and an accuracy of $\Delta p \leq 0.005 \cdot p_{\max}$ with $p_{\max} = 10\text{bar}$. The pressure sensor is mounted within the side wall at the bottom of the pressure vessel.

All temperatures are measured using resistance temperature devices (RTD) with a nominal electric resistance of $R_{RTD}(T = 273.15\text{K}) = 100\Omega$, a contact area of $A = 2 \times 2\text{mm}^2$ and a temperature accuracy of $\Delta T = \pm(0.3\text{K} + 0.005 \cdot (T - 273.15\text{K}))$. All RTD's are setup in the four-wire (4w) configuration in order to compensate the resistance of the connecting cable, which in some cases has a length of around 10m. The current source is the NI PXI 4071 DMM. Due to the properties of the switch matrix module NI PXI 2533 it was possible to use a series connection in order to setup groups of RTDs, e.g. all RTDs of the heating elements are combined to one group. This method allows saving a lot of the limited electrical feedthroughs.
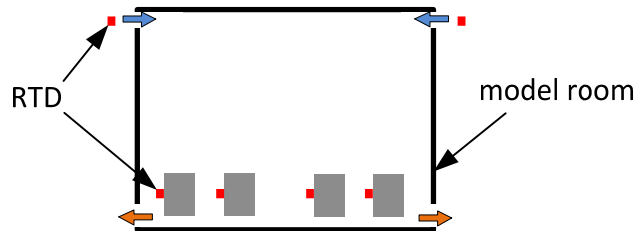
Fig. 7 Positions of the resistance temperature devices (RTD) within one x-y-cross-section of the model room

Five RTDs are installed around the outside of the model room for monitoring and controlling of the working gas temperature. Further RTDs are installed in the inlets and on the heating elements as depicted in Fig. 7. These RTDs are arranged in three *x-y*-cross-sections that are distributed in *z*-direction and arranged in the front, the middle and the back of the room at $z/D = [0.17, 0.49, 0.874]$. So, according to Fig. 7, there are three RTDs on each inlet and three RTDs on each heating element. The RTDs on the heating elements are arranged only on the left side. Due to the symmetry of the model room and assuming a large-scale flow structure with respect to the middle *y-z*-cross-section it is possible to get information of every gap between the heating elements with only a few sensors. The RTDs monitoring the inlet flow temperature are mounted in front of the inlet nozzle in the same *x-y*-cross-section as the ones of the heating elements.

With the purpose of reducing the influence of thermal radiation, the heating elements are made of aluminum. Each of them comprises two electrical heating cartridges, which are connected by a parallel circuit and are operated using a constant electrical power. As depicted in Fig. 8, the air conditioning system 1 (AC1) is setup for generating and controlling the inlet flow inside the model room, i.e. it is the ventilation system of the model room. The inlet flow is generated by a frequency controlled fan with the maximum volume flow rate $\dot{V} = 29.8$l/s. The frequency of the fan is controlled by a Siemens Sinamics G110 frequency converter, which keeps the volume flow rate of the fan constant. A direct measurement of the flow rate is not possible, because there is no measurement system available for determining the flow rate of the inlet flow, which fits the environmental conditions of compressed SF_6 contaminated with particles. Consequently, the inlet velocity is determined by velocity measurements within the inlet using the laser Doppler velocimetry (LDV) system. A detailed description of the measurement of the inlet velocity is given in section 3.6.1. The heat exchanger ($P = 865$W) installed within the AC1 downstream from the fan for controlling the temperature of the inlet flow is hydraulically connected to the thermostat KB10C20 by PD-Industriegesellschaft mbH on the outside of the pressure vessel. The temperature is controlled by a PID-controller in the SCALEX-OS, which uses the mean of all six RTDs of the model room inlets as the actual value. As shown in Fig. 8, the AC1 is designed as a closed circulation system, i.e. the flow circulates from the outlets of the model room over the fan and the heat exchanger to the inlets of the room. To prevent high pressure differences between the circulation system and the environment while increasing or decreasing the pressure of the working gas, three remote controlled valves are installed in the circulation system and the particle generator part. As depicted in Fig. 8, a nozzle is integrated in the AC1 downstream from the heat exchanger for applying the seeding.
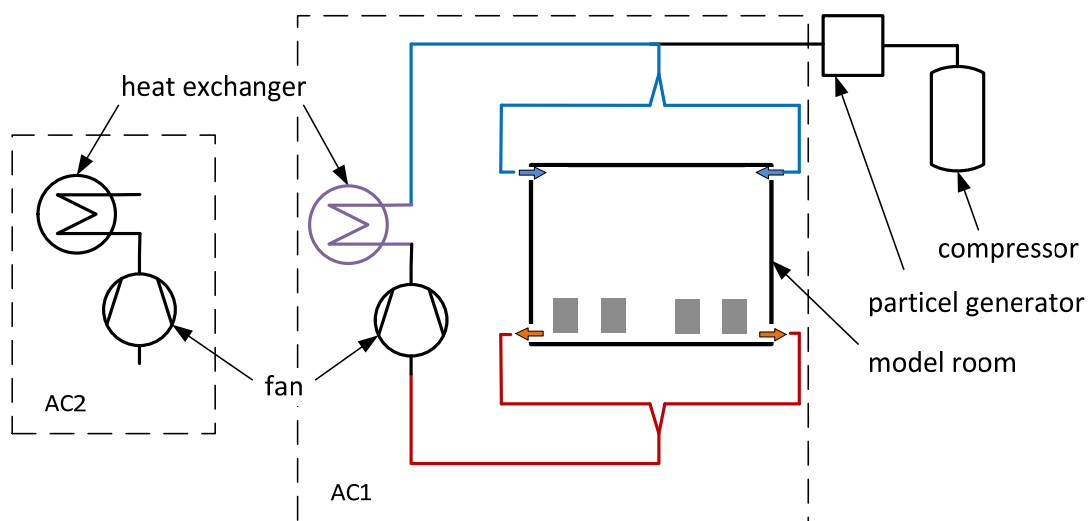
Fig. 8 Schematic of the ventilation system of the model room (AC1), the environmental control system (AC2) and the devices for particle generation

The temperature of the working gas is controlled through the second air conditioning system (AC2), which is installed in the back of the pressure vessel and depicted in Fig. 8 and Fig. 9. The AC2 is designed as an open system with a heat exchanger (P = 518W) connected to a fan ($\dot{V}$ = 29.8l/s). The heat exchanger itself is hydraulically connected to the thermostat HAAKE Phoenix II P1-C40P by Thermo Fisher Scientific on the outside of the pressure vessel. The thermostat is again controlled by a PID-controller in the SCALEX-OS with the mean of the five RTDs around the model room as the actual value of the ambient temperature. In order to keep the temperature of the working gas constant the AC2 has to dissipate the heat from all the electric devices inside the pressure vessel and the heat which results from the compression of the working gas.
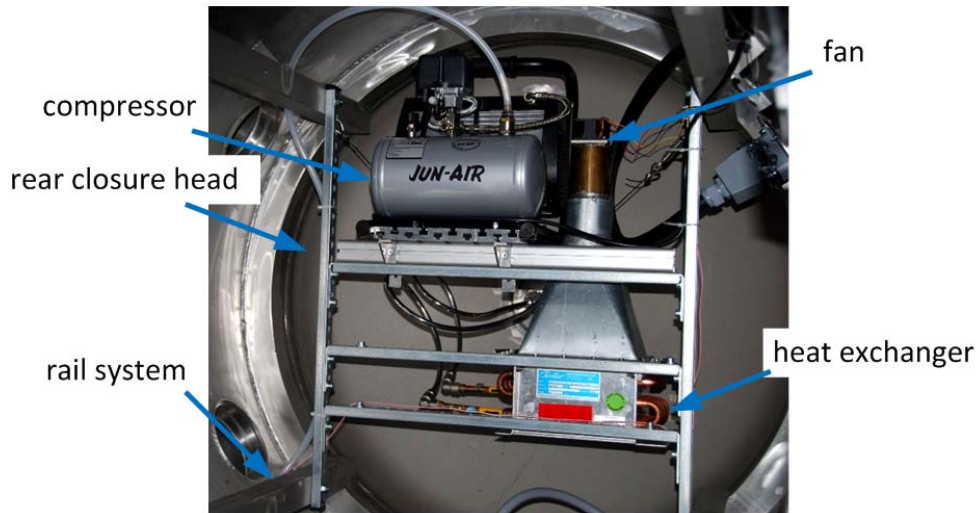
Fig. 9 View on the back of the pressure vessel with the heat exchanger and the fan as part of the air conditioning system 2 (AC2) along with the compressor as part of the particle generator assembly

The achievable range of the Rayleigh number *Ra* and Reynolds number *Re* of the SCALEX-facility as a function of the working gas pressure between 1bar $\leq p \leq$ 10bar for SF_6 and dry air are shown in Fig. 10. The material properties are calculated assuming a constant ambient temperature of *T* = 295.15K, a temperature difference range of 1K $\leq \Delta T \leq$ 50K, a range of the characteristic height of 0.05m $\leq L \leq$ 0.5m, an inlet velocity range of 0.05m/s $\leq u_{in} \leq$ 1m/s and a gravitational acceleration of *g* = 9.81m/s². Using dry air as the working gas, the ranges of the Rayleigh number and the Reynolds number yield $1.2 \times 10^4 \leq Ra \leq 5.9 \times 10^{10}$ and $160 \leq Re \leq 3.2 \times 10^5$. The working gas SF_6 allows within the same pressure range almost two magnitudes higher Rayleigh numbers and one magnitude higher Reynolds numbers, which is $5.22 \times 10^5 \leq Ra \leq 3.24 \times 10^{12}$ and $976 \leq Re \leq 1.39 \times 10^6$. So, in the SCALEX-facility a Rayleigh number range of $1.2 \times 10^4 \leq Ra \leq 3.24 \times 10^{12}$ and a Reynolds number range of $160 \leq Re \leq 1.39 \times 10^6$ can be

achieved. The Prandtl numbers Pr for air has the range of $0.706 \leq Pr \leq 0.712$. When using SF_6, the Prandtl number range is increased and yields $0.8 \leq Pr \leq 1.312$.
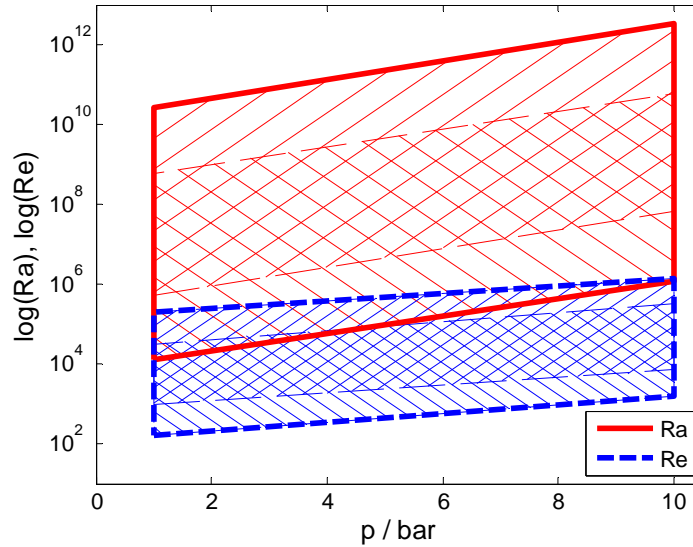
Fig. 10 Ranges of the Rayleigh number and the Reynolds number in the SCALEX-facility as a function of the pressure for the working gases SF_6 and dry air

So, the set up SCALEX-facility provides a very broad range of achievable dimensionless numbers, which allows the investigation of realistic indoor airflow problems. Or in other words, the SCALEX-facility allows performing fundamental as well as applied research of indoor airflows using small-scale experiments with very high scale-factors.

3.4.3 Flow measurement systems

The particles, required for flow visualization and the LDV technique, are generated by a PIVpart14 seeding device from PIVTec GmbH. This device uses 14 Laskin nozzles for the atomization of an oil-like liquid, which is in this case di(2-ethylhexyl)sebacte (DEHS). According to the producers specifications the average particle diameter is $d_p = 1\mu m$. The needed over pressure is generated by the compressor OF302-4B from Jun-Air, as shown in Fig. 9. Both, the particle generator and the compressor are mounted inside the pressure vessel as schematically shown in Fig. 8. Thus, they do not have to be modified to meet the tightness and pressure resistance requirements. The particle concentration in the measurement volume can be remotely controlled by a time relay controlled magnetic valve within the connection between the compressor and the particle generator, i.e. the particle concentration is adjusted through the duration of generation and the time between the generation phases. The magnetic valve method is working for gas

densities below $\rho \approx 15\text{kg/m}^3$. For higher densities, which is the case for the calculated SF_6 working pressure $p = 4.517\text{bar}$ with $\rho \approx 28\text{kg/m}^3$, the power of the compressor is not sufficient to generate a high enough pressure difference within the small pressure reservoir. So, the magnetic valve is permanently open and the compressor is used as a time relay controlled pump. Additionally, the usage of solid particles allows a much better illumination, but it is not very useful with respect to the maintenance of the facility, because the model room has to be cleaned more often.

The laser light sheet system (LLS), shown in Fig. 11, is used for visualization of the large-scale flow structures within the model room and is setup within the pressure vessel. The LLS-System consists of a laser source, a tilted dielectric mirror and an oscillating mirror. According to the specification sheet, the laser source is a constant wave diode pumped solid state (CW-DPSS) laser with a maximum light power of $P = 500\text{mW}$, a wave length of $\lambda = 532\text{nm}$ and a diameter at the aperture of $d = 2\text{mm}$. The tilted mirror has a laser line dielectric coating optimized for the wavelength of $\lambda = 532\text{nm}$ and an angle of incidence of $0° \leq \alpha \leq 45°$ in order to assure a minimum loss of light power. The oscillating mirror is a very thin broadband mirror which is driven by a magnetic system. The oscillation is generated by a digital function generator through adjusting the frequency and the amplitude of the electric voltage of the magnetic system. In order to illuminate the full x-y-cross-section of the model room, very high amplitudes of the oscillation are required. This can be achieved by driving the mirror at its resonance frequency at $f \approx 67\text{Hz}$. This frequency is much higher than the frame rate of the camera system of $f = 25\text{Hz}$, which allows a homogeneous exposition of the camera sensor within one single frame. The used camera system consists of the consumer digital single-lens reflex (DSLR) camera Canon EOS600d with the Canon EF-S 18-135mm 1:3.5-5.6 IS II lens. The complete LLS-System is setup on the linear axis PICO LTP80/550 by FMD Dresden GmbH in order to allow the traversing of the light sheet through nearly the whole room. The linear axis is controlled using the traverse extension of the SCALEX-OS from the control computer outside the pressure vessel. The camera system is positioned along the normal vector of the *x-y*-cross-section, which is illuminated by the laser light sheet as depicted in Fig. 11a.
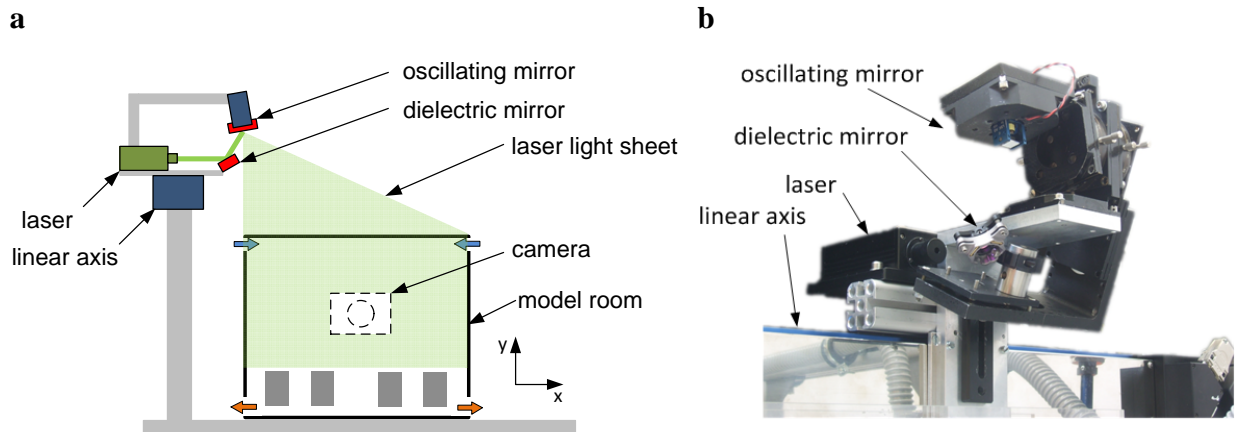
Fig. 11 a Schematic of the laser light sheet system (LLS); **b** realization of the LLS in the SCALEX-facility

The horizontal and vertical velocity component u and v in the x-y-cross-section are measured using a 2D FiberFlow laser Doppler velocimetry (LDV) System from Dantec Dynamics. The generic setup and measurement principle of a LDV is described in Tropea *et al.*, 2007 [39]. Its implementation at the SCALEX-facility is depicted in Fig. 12. A programmable 3D traverse system is used in order to perform automatic measurements within the full model room. The LDV and the traverse system are controlled with the BSA flow software from Dantec Dynamics. The laser light source of the LDV-system is an Argon multi-mode laser with a maximum light power of $P \approx 430mW$. Although it is not necessary to modify the system itself, it has to be pushed to its limits to perform velocity measurements inside the pressure vessel with reliable data rates. A main reason is the complex optical path of the laser light, arising from reflection and transmission effects of the thick window and the compressed SF_6. Another reason arises from the large distance between the LDV-probe and the measurement volume inside the model room. Both issues are responsible for a reduced sensitivity of the LDV.

The loss in sensitivity due to reflection and transmission effects can be reduced by exhausting the maximum laser power and the maximum sensitivity of the receiving optics. Thus, the laser power used to perform velocity measurements inside the pressure vessel amounts to $P \approx 400mW$. Increasing the sensitivity of the photo detector to its maximum is another possibility to achieve a reduction of the loss in sensitivity. Due to the usage of the LDV-system from the outside of the pressure vessel, a large focal length f has to be used. The necessity of a large focal length f results in an increased measurement volume, which again affects a decreased spatial resolution. So, in order to minimize the measurement volume a beam expander is applied to the LDV-probe. All four beams of the 2D-LDV-system are feed through this single probe, which itself is mounted on a goniometer. The goniometer again is mounted on the 3D-traverse system with the rotation axis in horizontal x-direction. This configuration allows an off-axis-alignment of the LDV-probe around the x-axis, which is necessary to measure flow velocities directly

underneath the ceiling of the model room. The LDV is setup in front of one of the big windows in the side wall of the pressure vessel, as shown in Fig. 12.
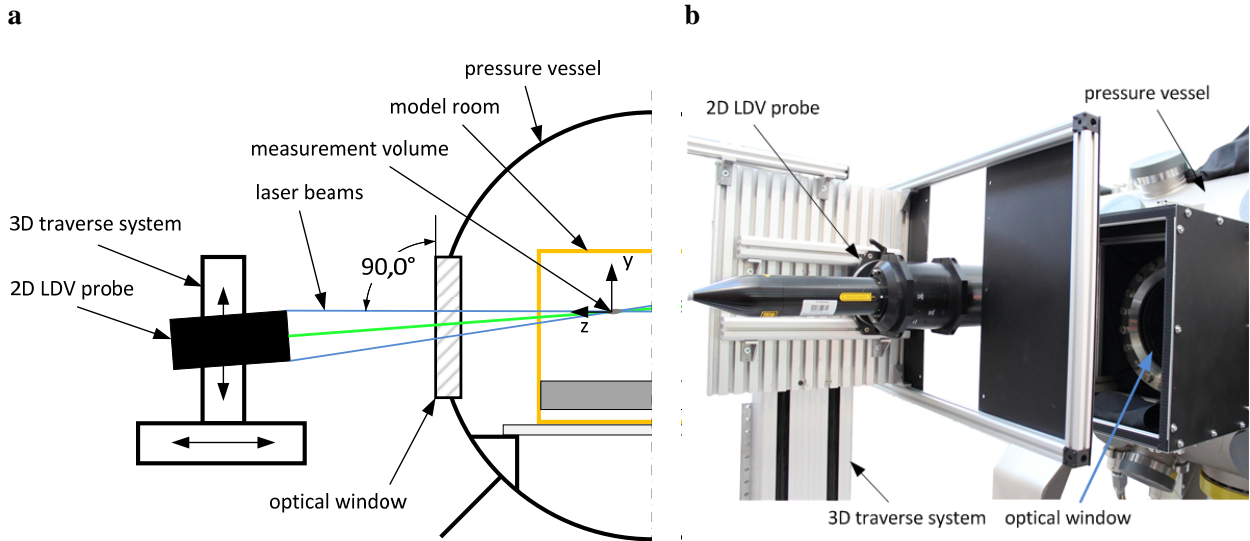
Fig. 12 Schematic (**a**) and realization (**b**) of the LDV setup at the SCALEX-facility

The two used wavelengths of the 2D-LDV-system are $\lambda = 488$nm for the vertical component of the velocity vector and $\lambda = 514.5$nm for the horizontal component, respectively. The focal length of the LDV-probe is $f = 1000$mm. The beam spacing before the beam expander is $b = 38$mm and the beam diameter amounts to $d = 2.2$mm. With the expander ration of $E = 1.858$ the beam spacing at the front lens of the beam expander is than $b' = b \cdot E = 70.6$mm. All geometrical configurations are identical for both wavelengths. According to Tridimas *et al.*, 1978 [55], these geometrical information of the probe allow the determination of the properties of the measurement volume and therefore the determination of the maximum measurement resolution, as shown in Tab. 2. As a result of the used optical system the beam half-angle is $\alpha = 2.022°$. As shown in Fig. 12a, the angle of the off-axis alignment is chosen to be equal to the half-angle α. Thus, the topmost laser beam ($\lambda = 488$nm) is perpendicular to the x-y-cross-section of the model room, which allows 2D velocity measurements very close to the ceiling of the model room.

	$\lambda = 488$nm	$\lambda = 514.5$nm
$x_{mv} = y_{mv}$ [mm]	0.1521	0.1604
z_{mv} [mm]	4.309	4.543
d_f [μm]	6.916	7.292

Tab. 2 Dimensions of the measurement volumes of the LDV-system for the wavelengths $\lambda = [488, 514.5]$nm and the focal length of f = 1000mm

The maximum dimensions of the LDV-measurement volume $x_{mv} = y_{mv} = 0.1604$mm and $z_{mv} = 4.543$mm are the maximum resolution of the velocity measurements. The measurement resolution within the x-y-cross-section is one magnitude higher than in z-direction. The minimum fringe spacing of the measurement volume is $d_f = 6.92$μm, which therefore fulfills the requirement $d_f > d_p$.

An optical power meter was used to adjust the laser beam of the laser light source with respect to the fiber and the probe. The LaserCAM HR, a laser diagnostic system from Coherent, was used to adjust the beam expander, i.e. that the laser beams has to be adjusted to the focal length of the front lens to intersect in the focal point. Therefore, the LaserCAM was setup within the pressure vessel in order to compensate the 40mm thick side window in the beam path.

The usage of a 3D-LDV-system instead of a 2D-LDV would allow measuring more details of the flow. But on the other hand, it would have a disproportionately higher configuration effort, particularly concerning the alignment, the feed through of the laser beams inside the pressure vessel and especially the traversing. This is caused by a second LDV probe, which is necessary when using a 3D system. If the laser beams of the second probe are feed through the same window there would be no problems with the traversing. But the possible measurement range is very limited due to the size of side window and the accuracy is decreased, because the angle between the 2D and the additional 1D probe is very small. The most accurate measurement of the third component could be realized by using a perpendicular alignment of the 1D probe with respect to the 2D probe. This would mean that the 1D probe has to feed through the top most window, which makes a constant alignment in combination with the traversing nearly impossible. So, it would only be possible to measure just one point. However, a 2D-LDV-system is much easier to implement in the SCALEX-facility and is sufficient for characterizing the large scale flow structures.

3.5   Experimental setup for the isothermal case

The investigation of the isothermal case is conducted in the same model room as described in section 3.1 within the Reynolds number range $1.0 \times 10^4 \leq Re \leq 7.0 \times 10^4$. Using ambient air at ambient pressure and room temperature as the working gas allows performing the experiments outside the pressure vessel. Except for some slight modifications, the setup of the model room and the flow measurement technique is comparable to the one for the case of mixed convection as described above.

The main modification concerns the generation of the inlet flow. To reach inlet velocities in the range of 0.5m/s $\leq u_{in} \leq 3.5$m/s, air from a compressed air supply of the laboratory hall is used. As depicted in Fig.

13a, the setup is designed as an open system, i.e. the outlet flow is not recycled. The inlet velocity is adjusted by adjusting the pressure of the air supply and measuring the maximum inlet velocity directly after the inlets at $x/L = 0.00125$, $y/H = 0.9967$ and $z/D = 0.02$.
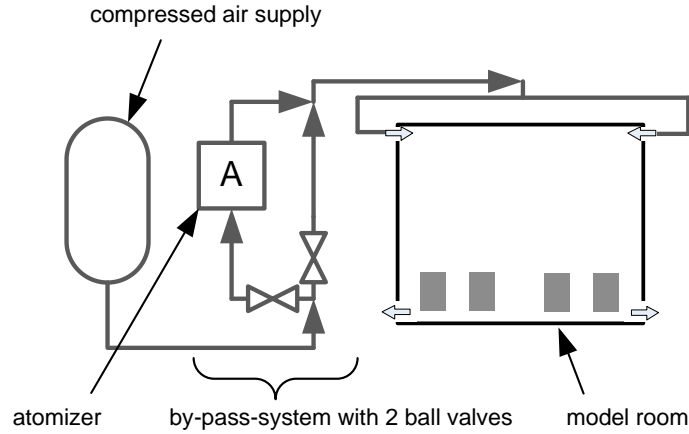
Fig. 13 Schematic of the modified AC1 setup for the investigation of the large-scale flow structure in the isothermal case $Ar \rightarrow 0$

The velocity measurements are conducted using the same LDV setup like the one used for the case of mixed convection. Only the focal length is reduced to $f = 310$mm, which can be justified by the increased optical accessibility and especially by the assumption of a nearly two-dimensional behavior of the flow. The assumption of the two-dimensional behavior of the flow is based on the findings of Nielsen *et al.*, 1978 [56] and is valid if the room is two-dimensional, too.

Furthermore, the smaller focal length of $f = 310$mm results in a reduced LDV measurement volume. The estimation of the measurement volume is also based on the work of Tridimas *et al.*, 1978 [55] using a focal length $f = 310$mm, a beam separation of $b = 72$mm and the two wavelength of $\lambda = [488, 514.5]$nm. The maximum size of the measurement volume is $\Delta z_{mv} = 419.2\mu m$ and $\Delta x_{mv} = 48.7\mu m$, as shown in Tab. 1. As realized in the setup for the case of mixed convection shown in Fig. 12a, the LDV is also setup in an off-axis alignment, tilted around the *y*-axis. But because of the decreased focal length, the angle is increased to $\alpha = 6.62°$. Furthermore, the higher optical accessibility allows the usage of a reduced laser light power of $P \approx 250$mW.

Wave length λ	488 nm		514.5 nm	
Focal length f	Δz_{mv} [mm]	Δx_{mv} 10^{-2} [mm]	Δx_{mv} [mm]	Δz_{mv} 10^{-2} [mm]
310 mm	0.3976	4.617	0.4192	4.868

Tab. 3 Estimation of the maximum width Δx_{mv} and length Δz_{mv} of the measurement volume

The tracer particles, needed for LDV measurements are generated by an atomizer in a by-pass-system inside the inlet flow system as shown in Fig. 13a. The tracer particles consists of DEHS atomized to drops of the average size of $d_p = 0.4\mu m$ with a PALAS AGF 10.0. The average particle size was taken from the user manual of the atomizer. With respect to a minimum fringe spacing of $d_f = 2.1\mu m$ for $\lambda = 488nm$ the size of the particles is small enough to achieve reliable LDV-signals.

In order to visualize the flow for the isothermal case, a laser light sheet with an average thickness of the light sheet of 2mm and a laser light power of $P = 100mW$ has been used. This laser light sheet system is based on a cylindrical lens to establish the light sheet. The DEHS-particles are used as tracer particles. The pictures are taken with a consumer digital single-lens reflex (DSLR) camera system by Nikon.

3.6 Boundary conditions and evaluation methods

3.6.1 Boundary conditions for the mixed convection case

For the case of mixed convection the measurement positions are distributed over three x-y-cross-sections within the full depth of the model room. The positions of the x-y-cross-sections are $z/D = [0.17, 0.49, 0.874]$. So, it is possible to determine data from the back, the middle and the front region of the model room. Within one x-y-cross-section, there are 10 rows of measurement points that are distributed equidistant between $x/L = 0.1254$ and $x/L = 0.8746$ with a distance of $x/L = 0.0833$. Within each row there are 6 measurement points between $y/H = 0.3667$ and $y/H = 0.9$ with a distance of $y/H = 0.1067$. Consequently, there are 60 measurement points in each x-y-cross-section. Long term measurements are performed at $(x/L, y/H, z/D) = (0.375, 0.687, 0.49)$ and $(x/L, y/H, z/D) = (0.542, 0.687, 0.49)$. The acquisition time for the investigation of the flow velocity field is $t = 10min$, which was determined with respect to the boundary conditions of the full-scale experiment described in the following. The acquisition time for the investigation of the temporal behavior of the flow is $t = 8h$. With respect to the Shannon theorem the minimum data rate amounts to $f = 2Hz$.

In order to do a first validation of the new experimental scaling method, the flow velocity fields of the small-scale experiment will be compared with data from an independently performed full-scale experimental of the prototype of the 1:10 model room. The setup of the prototype can be found in Kandzia et al., 2011 [57]. The reference parameter set for the comparison are fixed to the temperature difference $\Delta T = 7.5K$ between the inlet flow and the heating elements and the inlet velocity in the full-scale room $u_{in} = 0.8ms^{-1}$. The characteristic length is the height of the room H. In full-scale $H = 3m$ and according to the scale factor $m = 10$ in the small-scale model room $H = 0.3m$. With $T_{min} = 293.15K$ as the mean

temperature of the inlet flow, the material properties are calculated at $T_m = T_{min} + 0.5 \cdot \Delta T = 296.9$K. The material properties of the prototype are calculated for dry air at $p = 1.0$bar. The material properties of the working gas SF_6 are calculated for the pressure determined in section 3.3 at $p = 4.517$bar. A summary of the boundary conditions, material properties and dimensionless numbers can be found Tab. 4.

	prototype	model room	
boundary conditions			
working gas	dry air	SF_6	
p / bar	1.0	4.517	
T_m / K	296.9	296.9	
ΔT / K	7.5	7.5	
u_{in} / m s^{-1}	0.8	0.2929	
L / m	3	0.3	
material properties			
ρ / kg m^{-3}	1.1734	28.223	
β / K^{-1}	3.4×10^{-3}	4.0×10^{-3}	
λ / W m^{-1} K^{-1}	2.60×10^{-3}	1.31×10^{-3}	
η / Pa s	1.842×10^{-5}	1.724×10^{-5}	
c_p / J kg^{-1} K^{-1}	1004.6	685.233	
dimensionless numbers			deviations $d\xi_{SF6}$/ $d\xi_{dry\ air}$
Ra	1.933×10^{10}	1.933×10^{10}	1.00
Re	1.5292×10^{5}	1.4414×10^{5}	0.9426
Pr	0.7116	0.9048	1.2715
Ar	1.1616	1.0319	0.8852

Tab. 4 Overview of the boundary conditions, the material properties and the dimensionless numbers of the prototype and the scaled model room for the case of mixed convection

According to Tab. 4, there are some slight deviations of the Reynolds number and the Archimedes number between the model room and the prototype. These deviations are caused by the different material dependent Prandtl numbers Pr of air and compressed SF_6, i.e. it is not possible to achieve full similarity regarding all dimensionless numbers. But the deviations of the Reynolds number and the Archimedes number can be minimized by adjusting the inlet velocity. The inlet velocity of the model room amounts to $u_{in} = 0.293$ms^{-1}, which has the effect that the deviation of the Archimedes number is two times higher than the deviation of the Reynolds number. These deviations can also be obtained from Tab. 4. The relation between the inlet velocities amounts to $u_{in.II}/u_{in.I} = 0.366$ and is thus lower than the calculated one in

section 3.3. However, the Rayleigh number, Reynolds number, the Prandtl number and the Archimedes number for the reference conditions of the model room amounts to $Ra = 1.933 \times 10^{10}$, $Re = 1.4414 \times 10^5$, $Pr = 0.9048$ and $Ar = 1.0319$, respectively. In order to enable the comparison between the data of the full-scale and the small-scale experiment, the data is normalized to the mean value of the inlet velocity of each experiment.

The inlet velocity of the small-scale experiment is determined by using the LDV in an on-axis alignment. Assuming that $\boldsymbol{u} = (u_{in}, 0, 0)$ within the inlet, only one component of the LDV has to be used. So, beside the on-axis alignment and the usage of only one component of the LDV, the setup is equal to the one described in section 3.4.2. The mean value of the velocity is determined by measuring the vertical profile of the inlet velocity within the inlet. Because of the height of 2mm and the depth of 500mm it was not possible to measure the velocity profile at any arbitrary position. But with respect to the Reynolds number of the inlet flow in horizontal z-direction $Re_{in.z} = 2.4 \times 10^5$ the velocity profile can be assumed to be rectangular, i.e. the velocity distribution is nearly constant over the depth D of the room. By contrast, the velocity profile in vertical y-direction can be assumed to be parabolic, because $Re_{in.y} = 1.92 \times 10^3$ is below the critical Reynolds number $Re_c = 2.3 \times 10^3$ for the transition between laminar (parabolic profile) and turbulent flow (rectangular profile). The Reynolds number $Re_{in.y}$ is based on the material properties ρ and η, the inlet velocity u_{in} and twice the height of the inlet h_{in}, which must be assumed for $h \ll D$.

3.6.2 Boundary conditions and evaluation methods for the isothermal case

Due the fact that the inlets and outlets have the same depth as the model room and according to the findings of Nielsen *et al.*, 1978 [56] and some preliminarily visualizations, it can be assumed that the large-scale flow for the isothermal case $Ar \rightarrow 0$ is nearly 2-dimensional. Thus, the measurement positions in the isothermal case, shown in Fig. 14, are distributed in the central *x-y*-cross-section of the room at $z/D = 0.5$ and $x/L = [0.08, 0.25, 0.50, 0.75, 0.92]$. In vertical direction the velocity is measured at 11 points from underneath the ceiling at $y/H = 0.997$ to the top of the heating elements at $y/H = 0.347$. The long term measurements are performed at 5 points at $x/L = [0.08, 0.25, 0.50, 0.75, 0.92]$, $y/H = 0.63$ and $z/D = 0.5$, as depicted in Fig. 14.
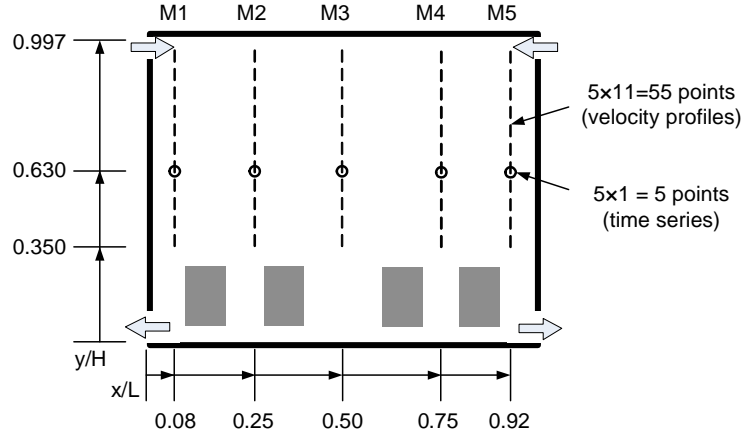
Fig. 14 Schematic of the measurement positions in the isothermal case; 11 measurement positions for the characterization of the velocity field are distributed along each of the 5 dashed lines (= 55 points); the five circles show the measurement positions for the time series of the long term measurements

The minimum acquisition time to ensure a statistical uncertainty of 10% from the real velocity value is determined by analyzing a test time series of the flow. At a Reynolds number of $Re_{ref} = 2.4 \times 10^4$ the correlation time τ_c, the mean velocity u and the standard deviation $\sigma(u)$ is determined. So, the calculated minimum acquisition time amounts to $t_{min} \approx 8$min, which results in a reasonable acquisition time for the velocity profiles of $t = 10$min. The acquisition time for long term measurements of the velocity has been chosen as $t = 60$min. Using a characteristic inlet velocity $u_c = u_{in} = 1.25$m/s and the characteristic length scale $l_c = H = 0.3$m, the characteristic time scale of the system amounts to $t_c = l_c/u_c = 0.24$s. Regarding the time scale t_c and the Shannon theorem, $f_s = 2/t_c = 8.33$Hz is the minimum data rate for the LDV-velocity measurements for characterizing the large-scale flow structures in the isothermal case. The typical data rates in the experiments are between $f_s = 20 - 100$Hz.

The cross check of the experimental results for the isothermal case is also done by comparing the results with an independent investigation of the model room, which is done by conducting a direct numerical simulation (DNS). The DNS can be applied to the problem, because the computational effort of the DNS is on an acceptable level, which is again caused by low Reynolds numbers and $Ra = 0$. Due to the fact that the realization of the DNS is not a part of the present work, the basics of the DNS are concluded in the following. The DNS is conducted on a mesh which is non-equidistant in every direction and is getting finer close the walls and especially near the inlets. In order to decrease the computational effort of the DNS, the depth of the model room is decreased by a factor of $D/D_{num} = 6.25$. As a boundary condition of DNS, the velocity profiles of the inlet flow are assumed to have a parabolic shape in vertical y-direction and a rectangular shape in horizontal z-direction. Further details regarding the DNS can be found in Körner *et al.*, 2013 [58].

In order to compare the results between the small-scale experiment and the DNS for the isothermal case, the velocity values are normalized to the maximum velocity of the inlet velocity u_{in}. The comparison of the velocity distributions between the experiment and the DNS is done for the reference Reynolds number $Re_{ref} = 2.4 \times 10^4$. The reference Reynolds number is based on a maximum inlet velocity of $u_{in} = 1.25$m/s, the height of the room H and the viscosity of air of $v(\vartheta = 22°C) = 1.55 \times 10^{-5}$m²s^{-1}. Although the computational effort is low for the isothermal case, the DNS is not able to provide information about the temporal behavior of the flow. Thus, the dependency of the flow on the Reynolds number with $Re = [1.0; 1.5; 2.4; 4.0; 6.0; 7.0] \times 10^4$, which corresponds to the maximum inlet velocities of $u_{in} = [0.52; 0.77; 1.25; 2.06; 3.10; 3.61]$ms^{-1}, as well as the temporal behavior of the flow has been studied only experimentally.

The measurement method of the LDV only provides velocity data that is non-equidistant in time, which do not permit the calculation of the power spectral density (PSD). The necessary resampling of the LDV-data to create equidistant time steps between the measurement samples is done by a linear interpolation of the LDV-data with a constant time step of $t_{lin} = 2 \times 10^3 \cdot t_{min}$ with t_{min} as the minimum measured time step of the raw data. A typical minimum time step is $t_{min} = 1 \times 10^{-5}$s. The resampled velocity time series is analyzed by determining the frequency distribution $P(\boldsymbol{u}')$, the probability density function (PDF) $P^G(\boldsymbol{u}')$ and the $PSD(\boldsymbol{u}')$ of the velocity fluctuations $\boldsymbol{u}'$. The frequency distribution $P(\boldsymbol{u}')$ is determined out of the resampled LDV-data with 5000 intervals of the velocity. The PDF $P^G(\boldsymbol{u}')$ is determined out of the mean velocity $\boldsymbol{u}$ of the time series and its standard deviation $\sigma(\boldsymbol{u}')$. The PSD's are obtained with the fast Fourier transformation (FFT) out of the autocorrelation function of the resampled LDV-data. In the FFT 2048 data points are used and the maximum frequency amounts to $f = 1/t_{lin}$.

In order to provide data for the definition of the inlet flow as a boundary condition for the experiment and particularly for the numerical investigation the velocity distribution $u(y,z)$ inside the inlet has been measured. Nearly the same experimental setup as described in section 3.5 has been used to realize this task. For geometrical reasons, an on-axis-alignment of the 2D-LDV-System with the optical axis pointing in vertical y-direction was more reasonable. The vertical profile $u(y)$ of the inlet velocity was measured at $z/D = 0.2$ and in between $0.986 \leq y/H \leq 1.002$. The horizontal velocity distribution of the inlet flow was measured in between $0.01 \leq z/D \leq 0.99$ at the maximum of the vertical velocity profile at $y/H = 0.997$. Both the vertical and horizontal measurements are performed at $x/L = 0.00125$. The Reynolds number $Re_{in.y} = u_{in} \cdot h_{in}/v$ of the inlet flow, which is based on the maximum inlet velocity $u_{in} = 4.5$m/s, which can be achieved in the experimental setup and twice the height of the inlet h_{in}, which must be assumed for $h << D$, gives $Re_{in.y} = 1.2 \times 10^3$. The Reynolds number $Re_{in.z} = u_{in} \cdot D/v$, which is based on the depth D of the

room, gives $Re_{in.z} = 1.5 \times 10^5$. Thus, a turbulent inlet flow with a rectangular shaped velocity distribution in z-direction and a parabolic distribution in y-direction is expected.

4 Results

In the following section, the results of the investigation of the velocity distribution of the large-scale flow structures are described and discussed for the isothermal (4.1) and the mixed convection case (4.2). Both sections begin with the characterization of the boundary conditions. For the isothermal case, the boundary condition comprises only the inlet velocity. For the mixed convection case it is necessary to characterize the operating conditions of the SCALEX-facility. Thus the data of the pressure, the heating elements and the inlet velocity are discussed before the behavior of the flow is discussed. Furthermore, the sections 4.1 and 4.2 contain the basic explanation of the found flow structure and the comparison with the DNS and the full-scale experiment. In addition, each section is separated into the investigation of the spatial and temporal behavior of the flow. The results of the investigation of the isothermal flow has been published in Körner *et al.*, 2013 [58]. The application of parameters important for the characterization of indoor air quality is demonstrated by the determination of the draft risk for both cases. Section 4 ends up with the error estimation of the previously found results.

4.1 Investigation of the flow for the isothermal case

4.1.1 Characterization of the inlet flow

The curves in Fig. 15a and b show the measured horizontal velocity u in front of the inlet as a function of y and z, respectively. The measurement of the vertical velocity profile starts inside the wall of the inlet. The velocity profile $u(y/H)$ in Fig. 15a shows a parabolic velocity distribution. Furthermore, Fig. 15b shows that the inlet velocity is homogenously distributed over the depth D of the model room. The maximum deviation from the mean maximum velocity in z-direction is $(u(z/D) - u(z/D)_{mean})/u(z/D)_{mean} = 0.0336$. So, the results of the velocity measurements within the inlet show that the assumption of a parabolic velocity profile in y-direction and a uniform velocity in z-direction, stated in section 3.6.2, is well satisfied. The chosen boundary conditions regarding the inlet flow of the DNS, as described in section 3.6.2, are also well suited to describe the inlet flow.

a

b
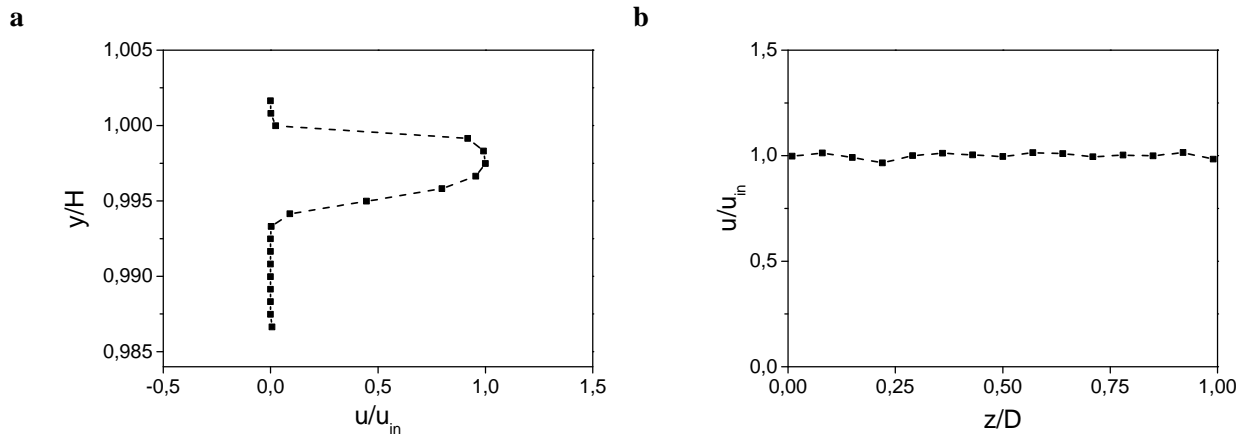
Fig. 15 Distribution of the horizontal velocity component u of the inlet flow normalized to the maximum of the inlet velocity u_{in}: (a) measured along the y-axis between $0.987 \leq y/H \leq 1.002$ and at $z/D = 0.2$; (b) measured along the z-axis between $0.01 \leq z/D \leq 0.99$ at $y/H = 0.997$

4.1.2 Comparison of the large-scale flow structures between experiment and numerical simulation

Fig. 16 shows the visualizations of the flow in the experiment (a) and the numerical simulation (b) in the chosen x-y-cross-sections (s. Fig. 14) at the reference Reynolds number $Re_{ref} = 2.4 \times 10^4$. Both visualizations reflect a distinct large-scale flow structure. The experimental flow visualization in Fig. 16a shows two large counter-rotating eddies driven by the inlet flow. These eddies have equal dimensions and are situated left and right of the center of the room. The cores of the large eddies are assumed to be at $x/L = 0.25$ and $x/L = 0.75$ and $y/H = 0.6$. Thus, the diameter of the large eddies is one half of the width of the room, limited by the walls of the room, the heating elements at the bottom and the contact point of the large eddies in the middle of the room ($x/L = 0.5$). Another finding of the visualization in Fig. 16a is, that the flow from each side moves out of the inlet in x-direction along the ceiling to the core position ($x/L = 0.25$ or 0.75) nearly with the dimensions of the height of the inlet. After passing the core position in x-direction, the flow has a vertical velocity component, as one could obtain from Fig. 16a. Furthermore, there is a stagnation point above the contact point of the two large eddies. Between the stagnation point and the contact point there are two smaller counter-rotating eddies. Fig. 16a also shows that there are smaller eddies, which are carried along by the large eddies, for instance in the left large eddy above the core position. It can be assumed that these smaller eddies are generated by eddy shedding at the sharp edges of the inlets.

Compared to the experiment the visualization of the flow predicted in the DNS in Fig. 16b reveals a similar flow structure. The two large eddies on each side of the room separated by the symmetry axis at

45

$x/L = 0.5$ are as well visible as the stagnation point. In addition to the visualization of the large-scale structures of the flow, the DNS data also provides details of the outlet flow. Figure Fig. 16b shows that the outlet flow mainly runs downwards in the middle of the room and between the side walls and the nearby the heating elements. The flow between the first and second and between the third and fourth heating element is almost zero. The outlet flow is horizontal after reaching the bottom and flows underneath the heating element towards the outlets in symmetry to the middle of the room.
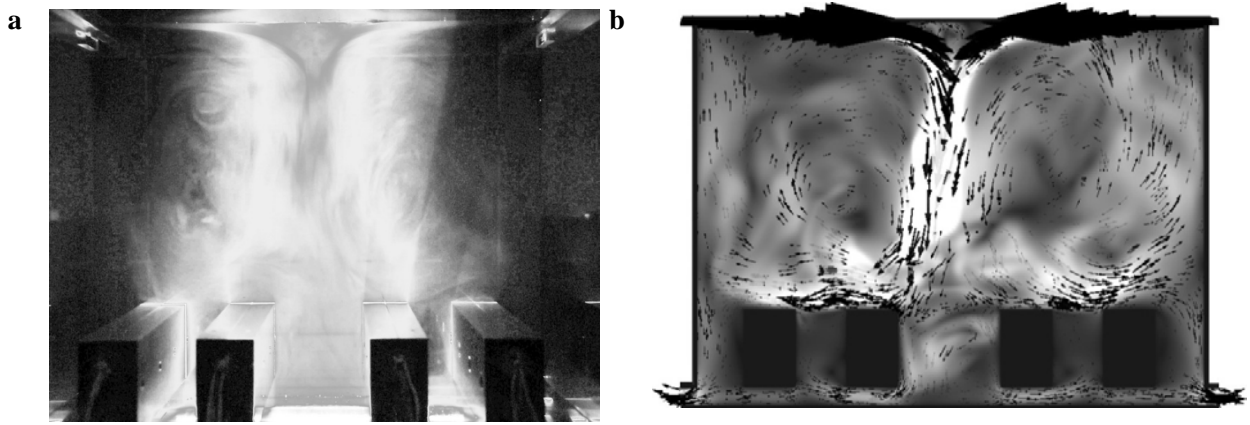

Fig. 16 Flow visualization from the experiment (**a**) and the numerical simulation (**b**) in the *x-y*-cross-section at $z/D = 0.5$

In Fig. 17 and Fig. 18 the profiles of horizontal and vertical velocity, $u(y/H)$ and $v(y/H)$, are presented at various *x*-positions as defined in Fig. 14 for the reference Reynolds number $Re_{ref} = 2.4 \times 10^4$. The experimental (▼) and numerical (solid line) velocity components are time averaged velocities and normalized to the maximum horizontal inlet velocity u_{in}. Fig. 17a and Fig. 18a are a summary of the velocity profiles related to cross-section in Fig. 14. In the diagram in Fig. 17a, the large-scale flow structures from the visualization in Fig. 16 can be easily recognized. That means that near the inlets at $y/H > 0.97$ and at the measurement position M1 and M5, which corresponds to Fig. 17b (position M1) and Fig. 17f (position M5), the horizontal velocity u is very high compared to bulk region. In the center of the room near the contact point at $x/L = 0.5$ and $0.4 \le y/L \le 0.9$, the mean of the horizontal velocity u tends to zero. The backflow of the large eddies over the heating elements can also be determined from the velocity profiles in Fig. 17a-f. That means, in the range of $y/H < 0.6$ at the measurement positions M1, M2, M4 and M5 in Fig. 17b,c,e, and f the flow points in the opposite direction as the inlet flow near the ceiling. These findings of the large-scale flow structures are in a good agreement to those made by Nielsen *et al.*, 1978 [56] regarding only one inlet and one outlet within the room.
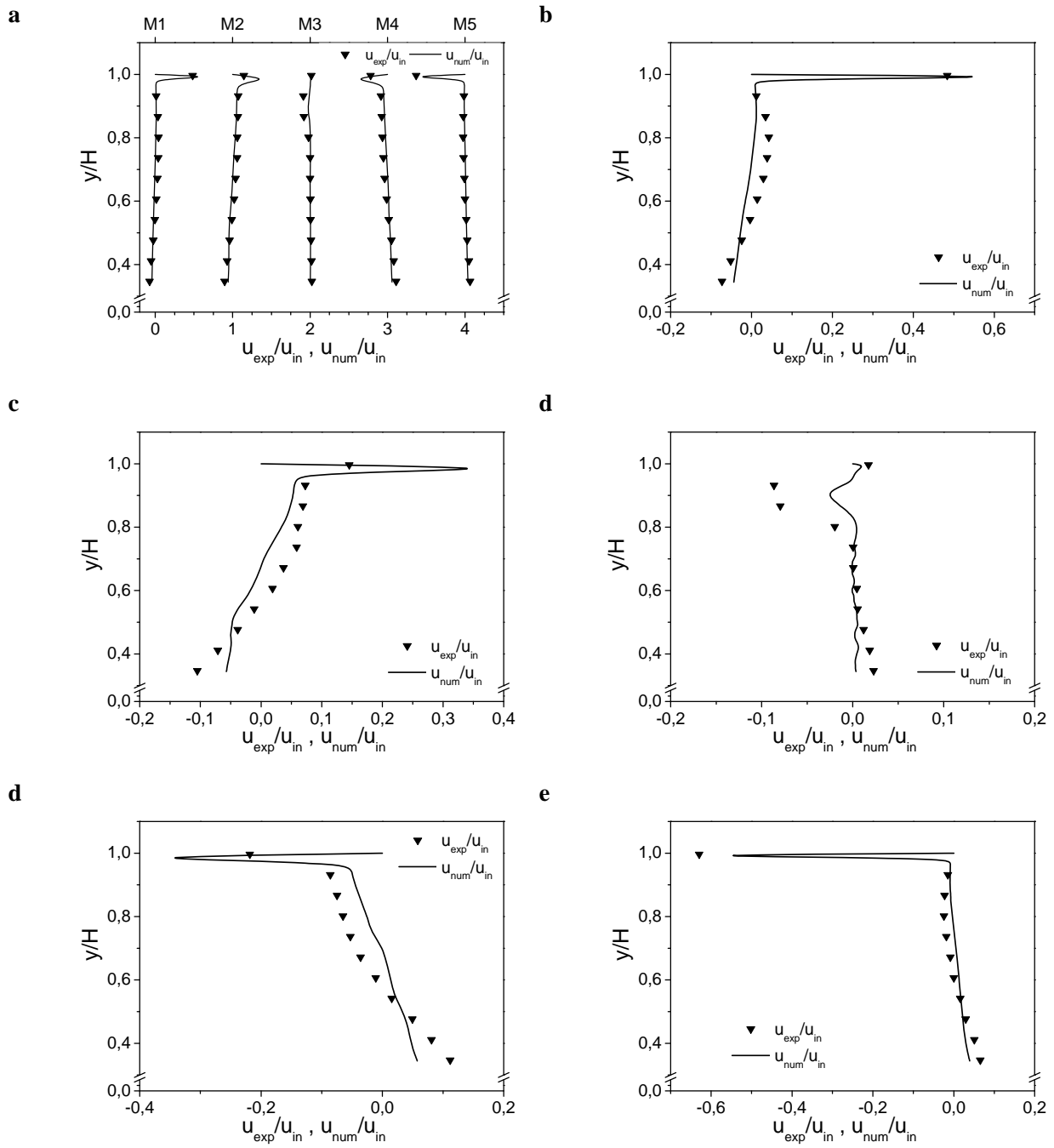
Fig. 17 Experimental (▼) and numerical (solid line) profiles of the horizontal velocity component u as a function of the height y/H at the defined measurement positions (M1 - M5) for the reference Reynolds number $Re_{ref} = 2.4 \times 10^4$; the velocities are normalized to the maximum of the inlet velocity u_{in}; (**a**) summary of the velocity profiles (shifted by +1); (**b-f**) detailed view of the velocity profiles for each measurement position (M1 - M5)
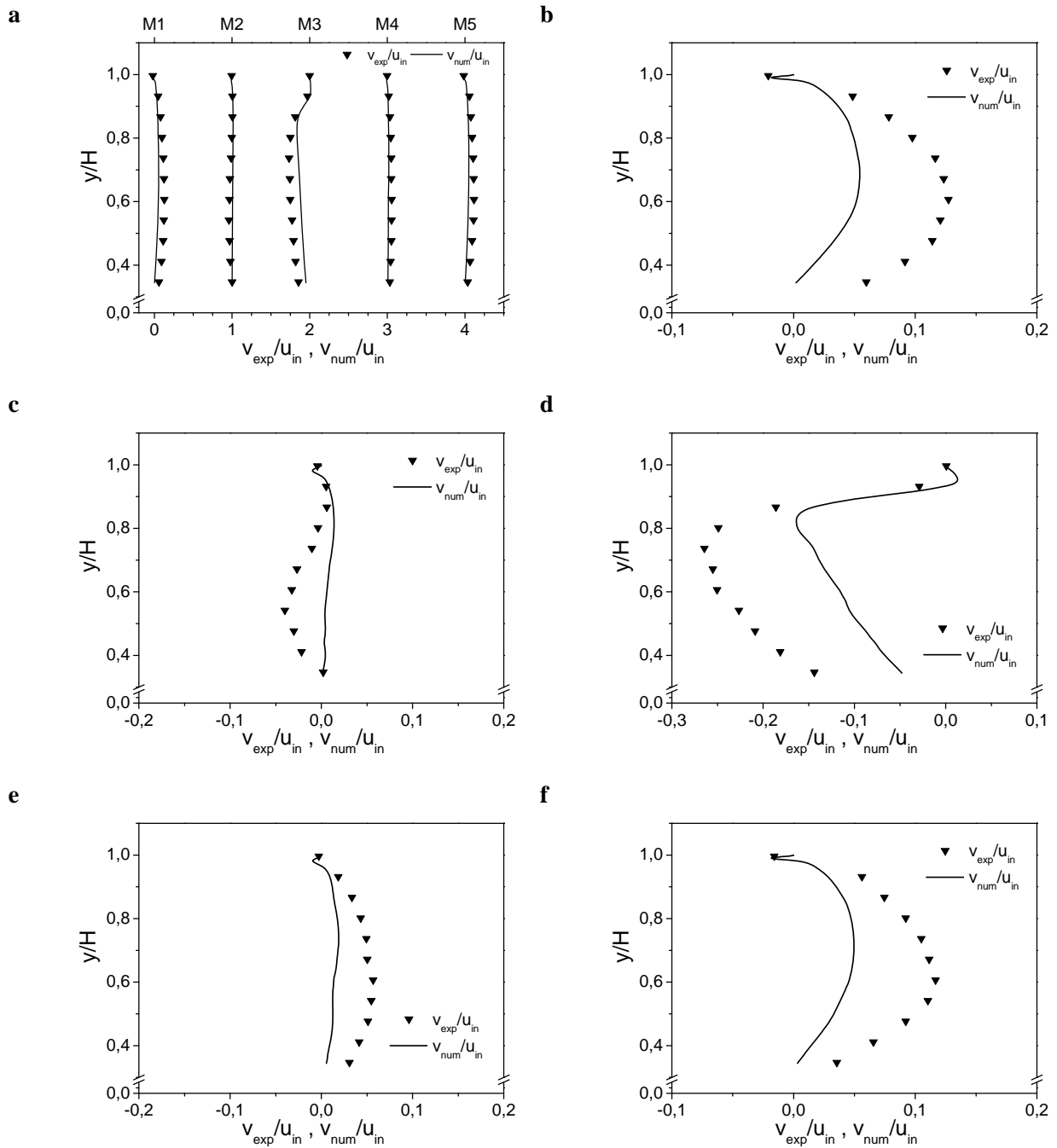
Fig. 18 Experimental (▼) and numerical (solid line) profiles of the vertical velocity component v as a function of the height y/H at the defined measurement positions (M1 - M5) for the reference Reynolds number $Re_{ref} = 2.4 \times 10^4$; the velocities are normalized to the maximum inlet velocity u_{in}; (**a**) summary of the velocity profiles (shifted by +1); (**b-f**) detailed view of the velocity profiles for each measurement position (M1 - M5)

The large-scale flow structures can also be determined from the velocity profiles of the vertical component in Fig. 18a-f. Particularly, the middle measurement position M3, which is shown in detail in Fig. 18d, reflects the downward motion of the flow at the contact point in negative y-direction. The figures also show the upward motion (in positive y-direction) of the flow near the walls of the model room at the

48

positions M1 and M5, shown in Fig. 18b and f. The maximum velocities for the positions M1, M3 and M5 are always at $y/H = 0.63$, the previously assumed vertical position of the vortex cores. The vertical component of the flow velocity at the measurement positions M2 and M4, presented in Fig. 18c and e, is nearly zero over the whole height H of the room.
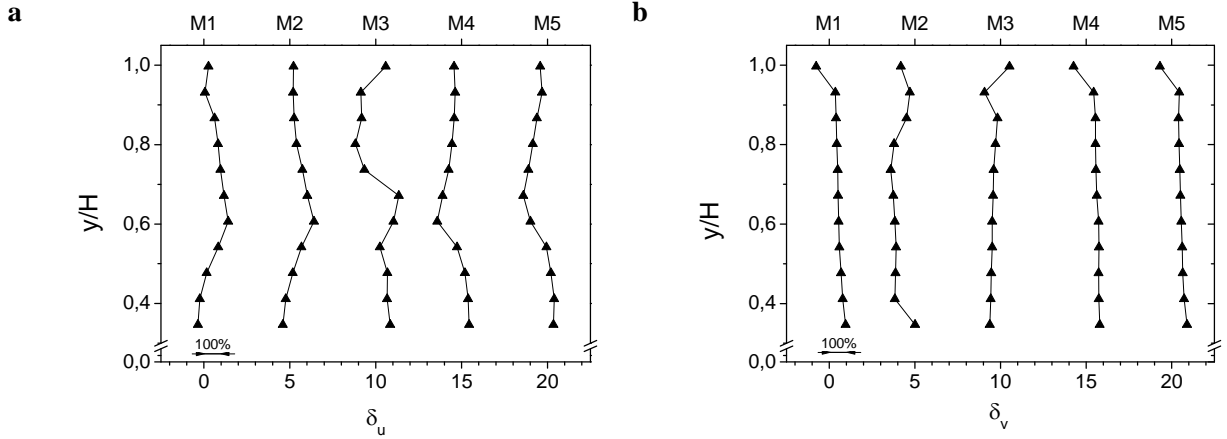
Fig. 19 Relative deviation δ of the velocities between the experiment and the numerical simulation as a function of the height of the room y/H at the reference Reynolds number $Re_{ref} = 2.4 \times 10^4$; data points are shifted by +5; (**a**) deviations of the horizontal velocity component δ_u; (**b**) deviations of the vertical velocity component δ_v

The difference δ between the experimental and numerical results can be quantified with

$$\delta_u = \frac{u_{exp} - u_{num}}{\sqrt{u_{exp}^2 + u_{num}^2}} \qquad (40)$$

for the horizontal component u and for the vertical component v, respectively. Fig. 19 summarizes the deviations at the measurement positions M1 – M5 over the height of the model room. The maximum deviations of the horizontal and vertical profiles are $\delta_u = 1.414$ and $\delta_v = 1.410$. By comparing Fig. 19 with Fig. 17a and Fig. 18a, the largest deviations in the horizontal and vertical component can be found, where the velocity tends to zero. While a qualitative similarity between the DNS and the experiment is given, the quantitative deviations are distinctive for some regions within the room.

The main reason for the deviations between the experimental and the numerical results might be the difference in the depth D of the model room between the numerical model and the experiment of $D_{exp}/D_{num} = 6.25$. This is a major impact on the mean flow inside the room, because the side walls in the z-y-cross-section have a much higher influence on the flow behavior. Another reason could be a slight difference in the value of the measured inlet velocity in the experiment in contrast to the defined inlet

velocity in the numerical simulation. Also the accuracy of the measurements, where the velocity tends to zero, for instance shown in Fig. 18c and e, is not reliable enough to resolve these small velocities. This would cause deviations, which are with respect to the absolute value very high and therefore generates very high relative errors.

4.1.3 Dependence of the flow structures on the Reynolds number Re

Fig. 20 depicts the experimental velocity profiles of the vertical component at the middle of the room at $x/L = 0.5$ (Fig. 20a; measurement position M3) and near the left wall at $x/L = 0.92$ (Fig. 20b; measurement position M5) for $Re = [1.0, 1.5, 2.4, 4.0, 6.0, 7.0] \times 10^4$. The velocities are normalized with the maximum inlet velocity u_{in}, which corresponds to the Reynolds numbers Re.

a **b**
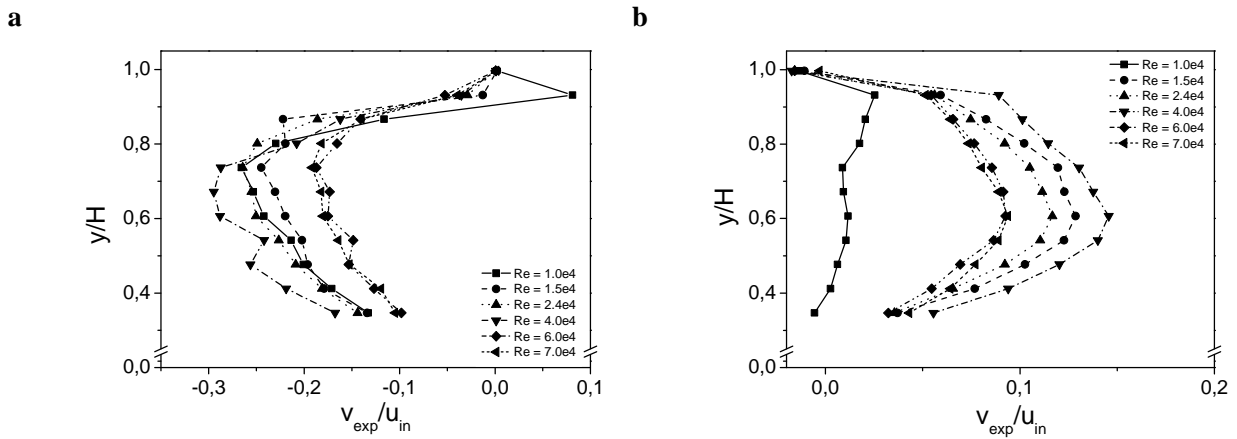
Fig. 20 Velocity profiles of the measured vertical velocity component v normalized to the maximum inlet velocity u_{in} as a function of the height of the room y/H for the Reynolds number range $1.0 \times 10^4 \leq Re \leq 7.0 \times 10^4$; (**a**) velocity profiles in the middle of the room at $x/L = 0.5$ (M3); (**b**) velocity profiles near the wall of the room at $x/L = 0.92$ (M5)

In Fig. 20a, the velocity profiles of the vertical velocity component v, which corresponds to the measurement position $x/L = 0.5$, are similar to each other within the complete range of Reynolds numbers Re. The velocity profiles of the vertical component near the wall at $x/L = 0.92$, documented in Fig. 20b, show a similar behavior except for the lowest Reynolds number $Re = 1.0 \times 10^4$. For this case the velocity tends to zero over the complete height of the room H, i.e. there is no upward flow within the large-scale structure. So, the large-scale flow structures have a Reynolds number dependence. It can be assumed that this behavior depends on the outlet flow and the behavior of the flow with respect to the geometry of the heating elements. In this case a short cut flow from the inlets over the center of the room to the outlets is the most promising explanation of the flow behavior. Thus, for recently low velocities no recirculation is existent.

50

4.1.4 Temporal behavior of the flow structures

Fig. 21 shows the frequency distributions $P(u')$ of the horizontal and vertical fluctuating velocity u'. The frequency distributions $P(u')$ are normalized to the average of ±5 values around the maximum of $P(u')$. In order to compare the measured distribution with the Gaussian probability density function $P^G(u')$ obtained from $\bar{u}$ and the standard deviation $\sigma(u')$, $P^G(u')$ is normalized to $P^G(u'=0)=1$. The velocity range is normalized to the standard deviation $\sigma(u')$.

a

b

c

d
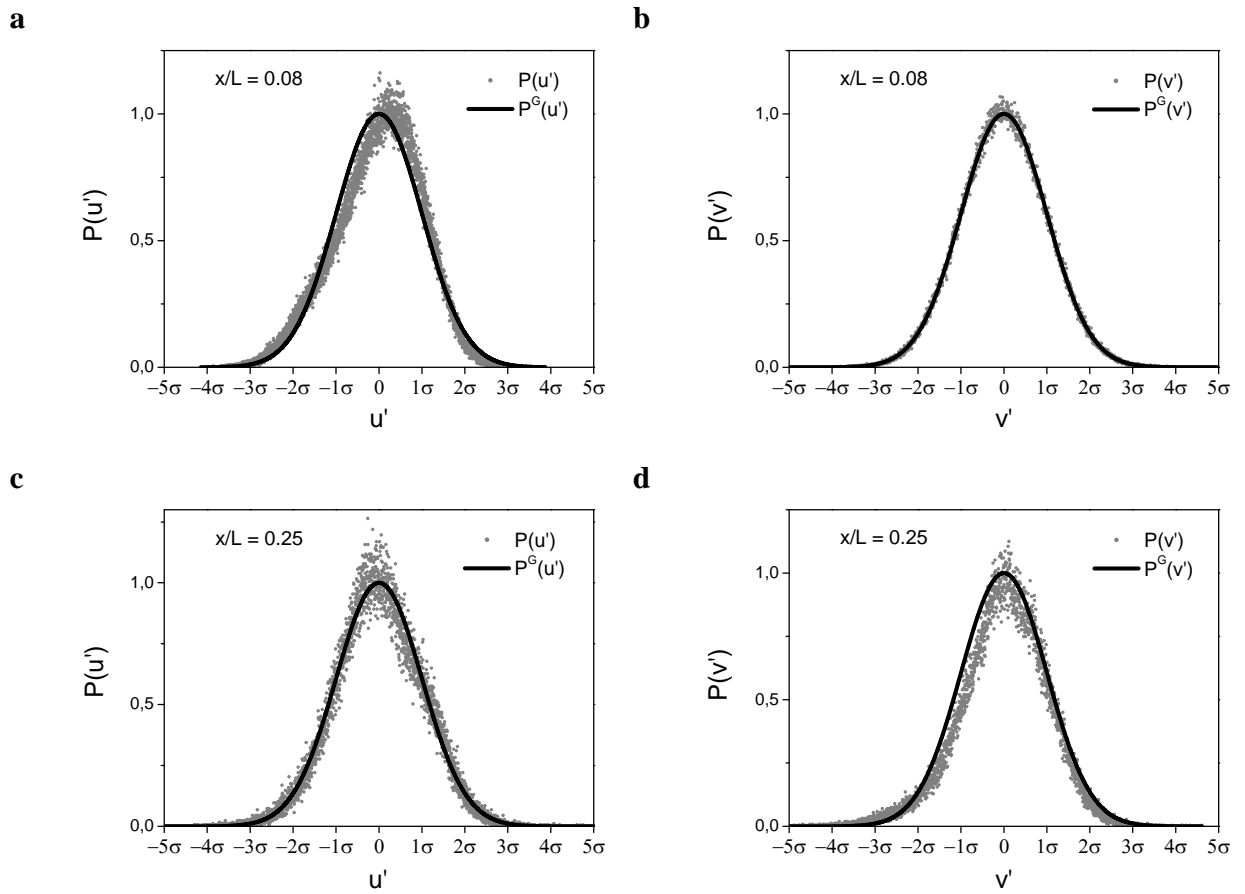
Fig. 21 (**a-j**) Frequency distributions $P(u')$ and $P(v')$ of the measured horizontal and vertical velocity fluctuations u' and v' in comparison with the normalized Gaussian probability density function $P^G(u')$ and $P^G(v')$ for $Re = 6.0\times10^4$ at $y/H = 0.633$, $z/D = 0.50$, and $x/L = [0.08, 0.25, 0.50, 0.75, 0.92]$
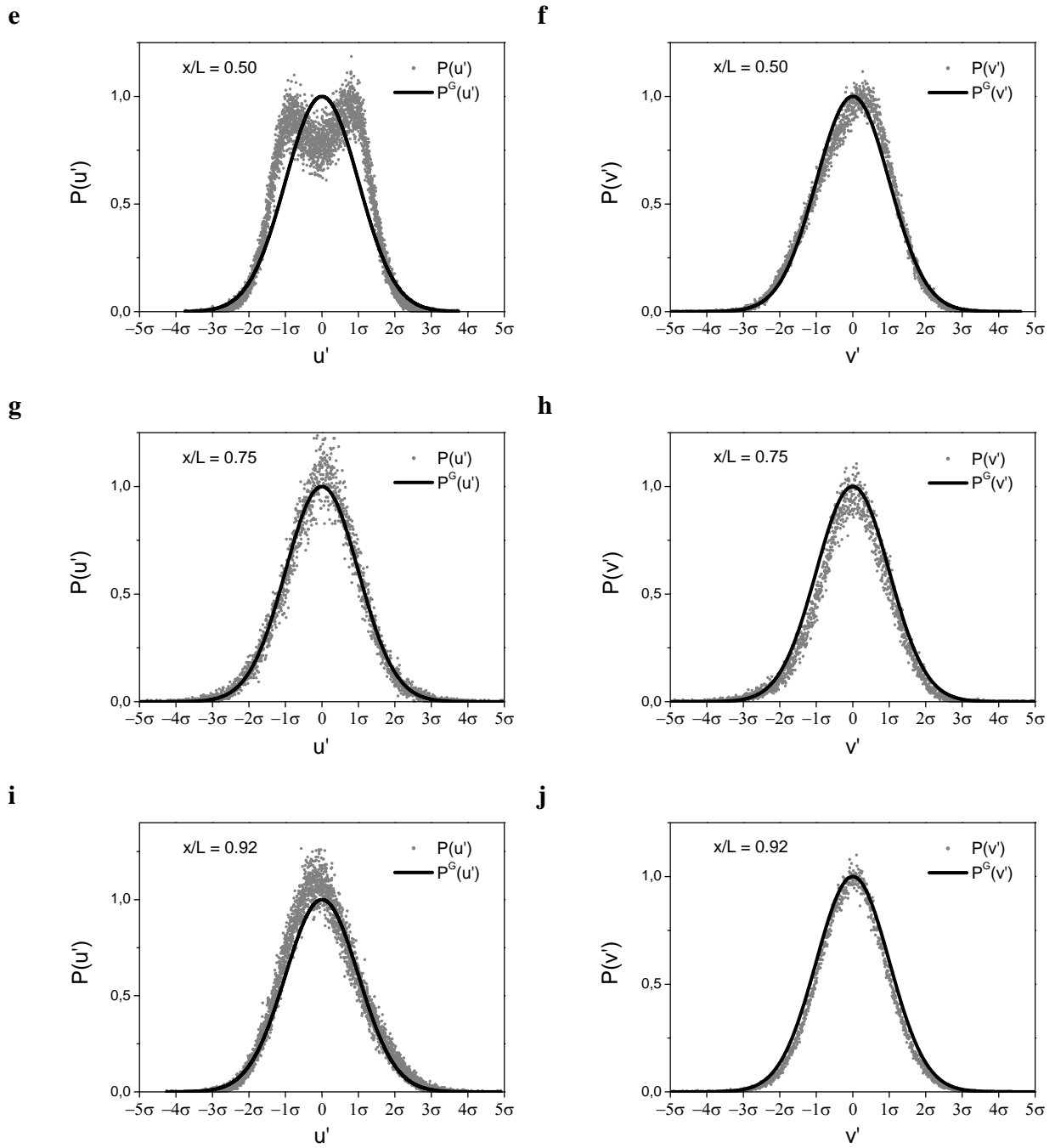
Fig. 21 (a-j) continued

Fig. 21 reflects that the frequency distribution of the horizontal and vertical velocity fluctuations show a nearly Gaussian distribution within the whole room, except for the horizontal fluctuations in the middle position of the room at $x/L = 0.50$, $y/H = 0.63$, and $z/D = 0.50$ which is presented in Fig. 21e. At this middle position the frequency distribution of the horizontal velocity fluctuations $P(u')$ shows two peaks and gives rise to the conclusion, that there are self-induced oscillations of the large-scale flow structures.

Furthermore, it can be found that the phenomenon neither appears in the frequency distribution of the vertical fluctuations $P(v')$ at the same position nor in the other frequency distributions of the horizontal and vertical fluctuations at all the other measurement positions. The reason for the absence of the oscillations in the vertical velocity in the middle of the room might be that the amplitude of the horizontal oscillation of the flow at the chosen measurement point is smaller than the half width of the fully developed vertical flow within the contact point of the counter-rotating eddies.
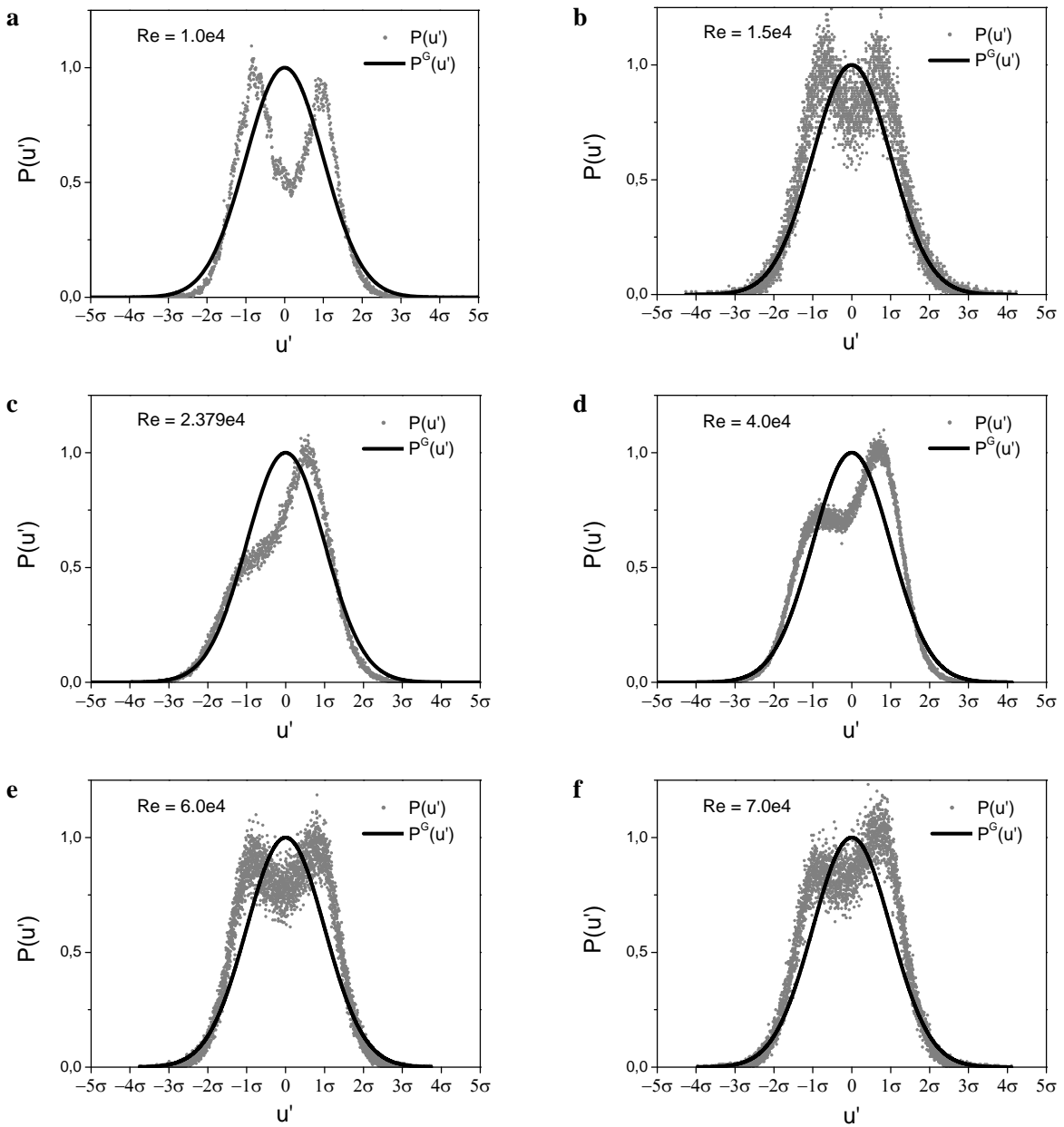
Fig. 22 (**a-f**) Frequency distributions $P(u')$ of the measured horizontal velocity fluctuations u' in comparison with the normalized Gaussian probability density function $P^G(u')$ for $1.0 \times 10^4 \leq Re \leq 7.0 \times 10^4$ at $x/L = 0.50$, $y/H = 0.63$, and $z/D = 0.50$ (M3)

Fig. 22 show the frequency distributions of the horizontal velocity fluctuations at $x/L = 0.50$, $y/H = 0.63$, and $z/D = 0.50$ for the complete investigated set of Reynolds numbers Re. The normalization rules are equal to that used in Fig. 21. From this it can be inferred that the frequency distributions always show two peaks within the complete Reynolds number range $1.0{\times}10^4 \le Re \le 7.0{\times}10^4$. Here, the frequency distributions also reflect a Reynolds number dependence, because for $Re = 2.4{\times}10^4$ and $Re = 4.0{\times}10^4$ the values of the amplitude of the two peaks are not equal, i.e. the left peak is smaller than the right peak. At the moment, there is no reasonable explanation for this phenomenon, which therefore needs further investigation in future studies.
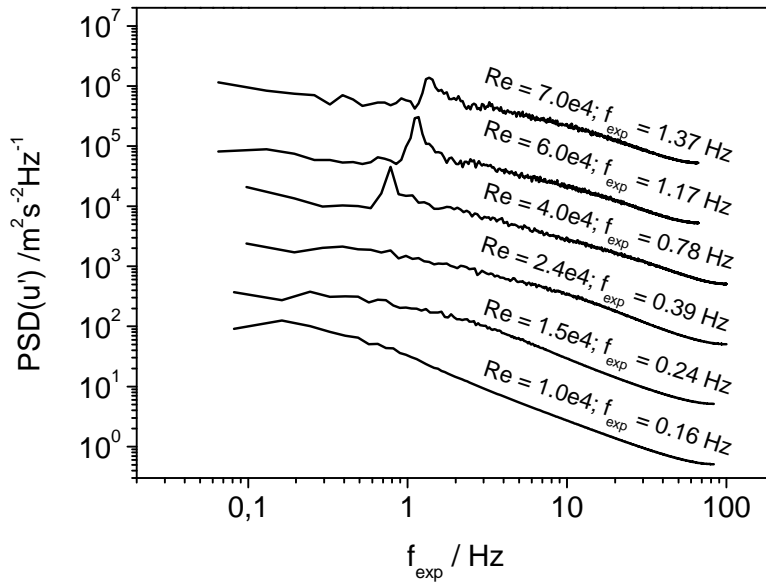
Fig. 23 Power spectral density PSD of the measured time series of the fluctuation of the horizontal velocity component u at $x/L = 0.5$ and $y/H = 0.63$ for $1.0{\times}10^4 \le Re \le 7.0{\times}10^4$; the curves are shifted by 10^1 and sorted with respect to the Reynolds number from low to high.

The PSD's of the horizontal velocity fluctuations u' for the investigated Reynolds number range of $1.0{\times}10^4 \le Re \le 7.0{\times}10^4$ are shown in Fig. 23. A significant peak can be found for all Reynolds numbers $Re \ge 4.0{\times}10^4$, which confirms the preliminarily assumed coherent oscillation of the large-scale flow structure in the horizontal direction x. In the Reynolds numbers range $1.0{\times}10^4 \le Re \le 2.4{\times}10^4$ there is no significant peak in the PSD. But for each Reynolds number two peaks in the PDFs in Fig. 22a-c can be found, which gives rise to the assumption that there also must be an oscillation of the flow in the region of the contact point. Thus, the frequency of the oscillation in the Reynolds number range $1.0{\times}10^4 \le Re \le 2.4{\times}10^4$ is estimated from the highest peak of the corresponding PSD. So, the frequencies of the coherent oscillations are in the range of $0.16 \le f \le 1.37$Hz and are proportional to the Reynolds

number. The amplitudes of the peaks have a maximum at $Re = 6.0 \times 10^4$, that means that around $Re = 6.0 \times 10^4$ there probably exists a resonance case. In contrast to the horizontal oscillations, the oscillations in vertical direction are negligible.

For a first explanation, it can be assumed that the found oscillations are an auto-oscillation of the system of the two opposed planar wall-jets that occurs from the inlet flow. The phenomenon of the auto-oscillation was first described by Denshchikov et al., 1978 [60], 1983 [61] and investigated numerically by Pawlowski *et al.*, 2006 [61] for two planar jets without a wall. The wall, i.e. the ceiling of the model room, has doubtless the effect that instead of an oscillation in two vertical directions, as reported by Denshchikov *et al.*, 1978 [59] and Pawlowski *et al.*, 2006 [61], an oscillation in horizontal direction establishes. This auto-oscillation influences the coherent oscillation of the large-scale flow structures. In order to check this assumption, the frequencies from the measurements are compared with the empirically found correlation for the period T of the oscillation suggested by Denshchikov *et al.*, 1983 [60] as follows:

$$\frac{T}{T^*} = 0.34 \cdot Re_{in}^{-1.0} \cdot \left(\frac{\delta}{L} \right) \tag{41}$$

with $Re_{in} = \rho u_{in} \delta \eta^{-1}$, $\delta \equiv h_{in}$ as the height of the inlets and L as the distance between the inlets. T^* is defined by

$$T^* = \frac{\rho L^2}{\eta} \tag{42}$$

with ρ as the fluid density and η as the dynamic viscosity. The calculated frequency of the auto-oscillation f_{AO} is than determined by

$$f_{AO} = \frac{1}{T} \tag{43}$$

The equations (41) and (42) are valid for $Re_{in} \leq 4800$, so they are also valid for the investigated case with the inlet Reynolds number in a range of $67 \leq Re_{in} \leq 464$.
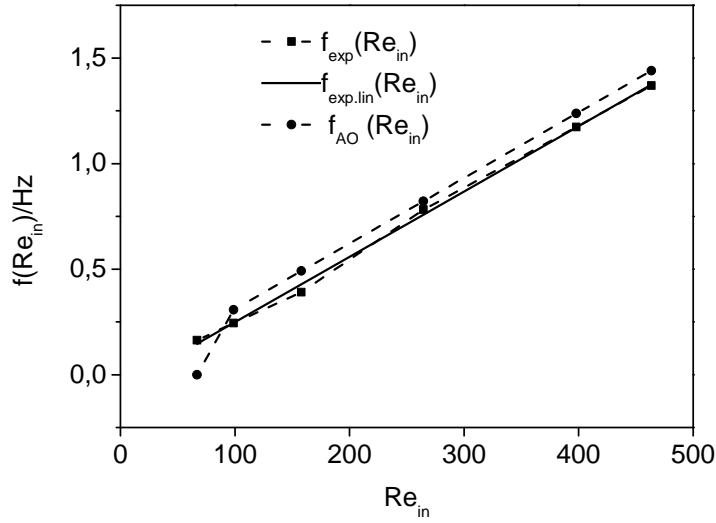
Fig. 24 Measured frequencies f_{exp} of the coherent oscillation of the large-scale flow structure inside the model room as a function of the Reynolds number Re_{in}; the experimental results (■) and its linear fit function (solid line) are compared with the correlation in equation (9) describing the frequencies of the auto-oscillation of two planar colliding jets f_{AO} (●) as a function of Re_{in}, L, and h_{in}

The comparison between the empirical model and the measured frequencies f_{AO} and f_{exp} in Fig. 24 shows that they are similar. The calculated frequencies and the linear interpolation of the experimental data, as presented in Fig. 24, are nearly congruent. That means that the found experimentally determined frequencies f_{exp} fit very well to the suggested empirical model. The deviations in the found frequencies of the oscillation between the experimental data and the theoretical model could be caused on the one hand by deviations in the boundary conditions, i.e. that the flow in the experiment is in contrast to the theoretical model blocked by the ceiling. Furthermore, the shape of the nozzle of the experiment is also different compared to that of Denshchikov. On the other hand the differences could be aroused by a superposition of other phenomena, which causes a coherent oscillation within the large-scale flow structure. A possible phenomenon could be the elliptical vortex instabilities, which were studied by Crow, 1970 [62] or experimentally visualized by Leweke & Williamson, 1998 [63] and predicted in theoretical models by Pierrehumbert, 1986 [64]. The instabilities can occur within the two large eddies and also in the two smaller eddies near the stagnation point and influence the complete flow inside the room.

4.1.5 Characterization of the draft risk *DR*

Fig. 25 shows the results of the determination of the draft risk within the model room for the isothermal case in which Fig. 25a shows the spatial distribution of the draft risk *DR* within the *x-y*-cross-section at $z/D = 0.5$ and $Re = 7.0 \times 10^4$. Fig. 25b shows the dependency of the draft risk *DR* on the Reynolds number

Re for the two points $(x/L, y/H) = ([0.0825, 0.5], [0.997, 0.607])$ within the *x-y*-cross-section. The draft risk *DR* is calculated on the basis of eq. (5) assuming a uniform air temperature inside the model room of $\vartheta_a = 22°C$. The draft risk is based on the velocities determined in the small-scale experiment, which are converted to the full-scale by $u_{full\text{-}scale} = m \cdot u_{small\text{-}scale}$. The turbulence level *Tu* is determined out of the velocity root-mean-square (r.m.s.) values with respect to eq. (6). The color legend in Fig. 25a is normalized to the maximum value of the draft risk within the *x-y*-cross-section and is depicted as rectangles, which are referred to each measurement position. The points for the evaluation of the Reynolds number dependency, indicated in Fig. 25a as red dots, are assumed to be the most significant within the model room. The topmost point at $(x/L, y/H) = (0.0825, 0.997)$ reflects the maximum draft risk whereas the point in the middle of the room at $(x/L, y/H) = (0.5, 0.607)$ reflect the most draft sensitive region of a standing person. For both points, the draft risk is determined for the full range of the investigated Reynolds numbers $1.0 \times 10^4 \leq Re \leq 7.0 \times 10^4$.
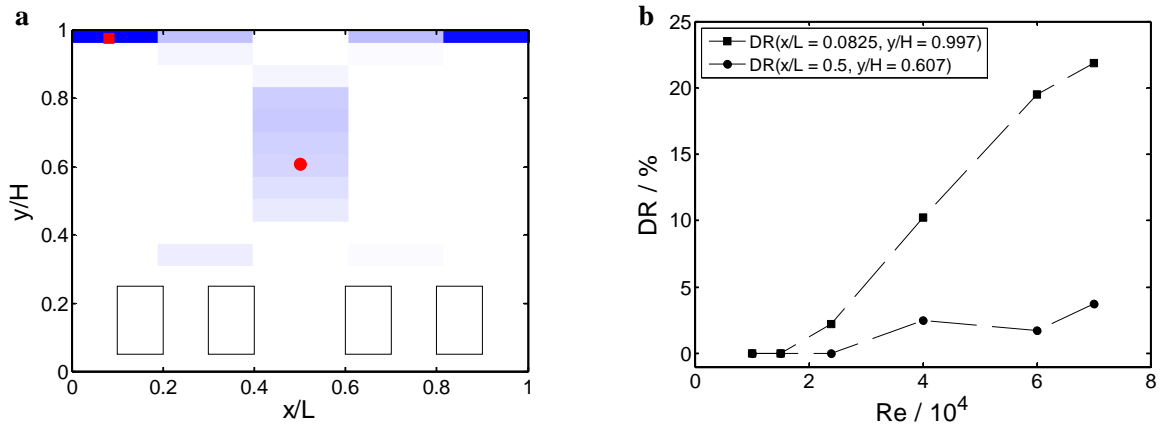
Fig. 25 a Distribution of the draft risk *DR* within the *x-y*-cross-section at $z/D = 0.5$ for the isothermal case at $Re = 7.0 \times 10^4$; the color legend in the *x-y*-cross-section is normalized to maximum *DR* value of each *x-y*-cross-section, with the darkest color depicting the highest value; all *DR* values with $|u| < 0.05ms^{-1}$ are set to $DR = 0$; **b** draft risk in dependency of the Reynolds number *Re* at $(x/L, y/H, z/D) = ([0.0825, 0.5], [0.997, 0.607], 0.5)$ as depicted by the red dots in figure **a**

As shown in Fig. 25a, the draft risk is very high in the region of the inlets near the ceiling of the room. At this region the maximum value of the draft risk occurs. It amounts with respect to Fig. 25b to $DR \approx 22\%$, which is according to DIN 1946 higher than the maximum permissible value of $DR \leq 15\%$ [35]. Beside the region near the inlets, the overall draft risk is very low or even zero over the full *x-y*-cross-section. As shown in Fig. 25a, $DR < 10\%$ in the middle of the room at the contact point of the two large eddies. Moreover, $DR = 0$ in the recirculation region of the large eddies left and right to the middle of the room. The draft risk also shows a Reynolds number dependency, as depicted in Fig. 25b. At $Re \leq 1.5 \times 10^4$ the draft risk is absent for both investigated points. At $Re = 2.4 \times 10^4$ a low draft risk occurs in the region of the

inlets, but there is no draft risk in the middle of the room. In the range of $Re \geq 4.0\times10^4$ the draft risk at both points linearly correlates with the Reynolds number. As a result, a draft risk occurs in the occupied zone at $0 \leq x/L \leq 1$ and $0 \leq y/H \leq 0.6$ when increasing the inlet velocity of the ventilation system above a certain value. But, the draft risk DR does not excess the maximum permissible value $DR = 15\%$ within the occupied region of the room.

4.2 Investigation of mixed convection

4.2.1 Characterization of the boundary conditions

Before characterizing the actual boundary conditions the required fan speed, which is controlled by the frequency converter as described in section 3.4.2, has to be determined. So, Fig. 26 shows the mean inlet velocity inside the inlets with respect to the frequency of the supply voltage of the fan, which is within the AC1. The filled squares (■) show the mean value $u_{in}(f)$ of the measured velocity profiles of the inlet flow at the frequencies $f = [20, 35.9, 36, 40]$Hz. The data points are fitted with a linear curve of the form $u_{in}(f) = af + b$, with $a = 0.0101$ and $b = -0.0125$. The required frequency of the supply voltage of the fan, which is necessary to reach the targeted inlet velocity of $u_{in,t} = 0.293$ms^{-1}, is then calculated using the linear curve. The calculated required frequency (□) amounts to $f_{calc} = 30.3$Hz.
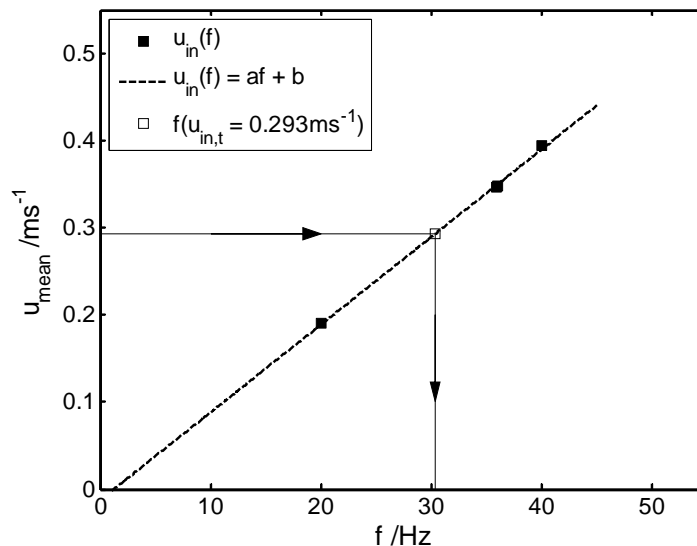
Fig. 26 Inlet velocity as a function of the frequency of the electrical supply of the fan; the frequency f to adjust the target inlet velocity $u_{in,t} = 0.293$ms^{-1} is calculated by linear interpolation $u_{in}(f) = af + b$ of the measured inlet velocities $u_{in}(f)$ with $a = 0.0101$ and $b = -0.0125$

A further measurement of the inlet velocity was performed in order to cross check the calculation of the required frequency. The result is depicted in Fig. 27, which shows the horizontal velocity component $u_{in} = f(y)$ with respect to the height of the inlet of $y = h = 2\text{mm}$. The measured velocity is shown with filled squares (■) and follows a shape, which can be approximated by the superposition of a rectangular and parabolic profile. This fits very well to its Reynolds number of $Re_{in.y} = 1.92 \times 10^3$, which is very close to the laminar-turbulent transition at $Re_c = 2.3 \times 10^3$ as stated in section 3.6.1. The measured velocities can be fitted by a 4th-order polynomial of the form $u(y) = ay^4 + by^3 + cy^2 + dy + e$ with $a = -0.3660$, $b = -0.5023$, $c = -0.2998$, $d = -0.1151$, $e = 0.3509$. Using the data fit $u(y)$ the measured mean inlet velocity for $f = 30.3\text{Hz}$ amounts to $u_{in} = 0.291\text{ms}^{-1}$. Related to the targeted inlet velocity the relative deviation of the measured inlet velocity is $(1 - u_{in} / u_{in,t}) = 0.0068$. So, the measured inlet velocity u_{in}, which is adjusted using the frequency adjustment of the electrical supply of the fan, is almost identical with the targeted calculated inlet velocity $u_{in,t}$.
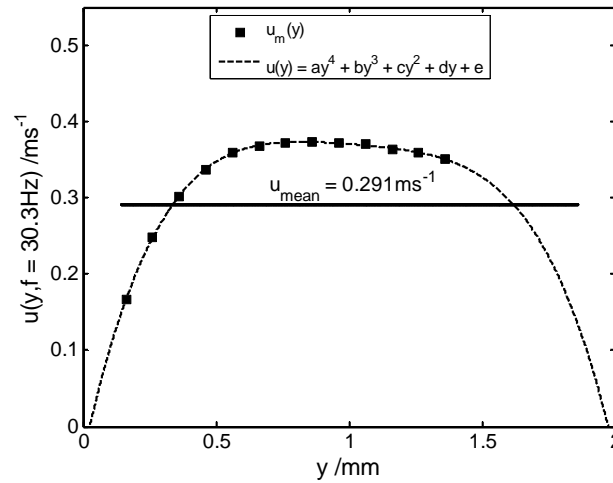
Fig. 27 Measured distribution of the inlet velocity u_{in} at the calculated frequency $f = 30.3\text{Hz}$ of the electrical supply of the fan; the measure velocities are fitted by a 4th-order polynomial with $[a, b, c, d, e] = [-0.366, -0.5023, -0.2998, -0.1151, 0.3509]$; the calculated mean inlet velocity is $u_{in} = 0.291\text{ms}^{-1}$ and $(1-u_{in.meas}/u_{in.target}) = 0.0068$

Fig. 28 shows the temporal behavior of the pressure of the working gas SF_6 inside the pressure vessel of the SCALEX-facility. The period shown in the diagram characterizes a usual time dependent behavior of the pressure during the LDV-measurement of one half of an x-y-cross-section ($= 5 \times 6 = 30\text{points} \times 10\text{min} + t_{trav} \approx 5.5\text{h}$). While $p_I(t)$ depicts the pressure time series from a first measurement campaign, the pressure $p_{II}(t)$ shows the pressure time series of a second one. Because of some technical improvements of the SCALEX-facility, e.g. an improved electromagnetic compatibility (EMC) of the pressure sensor or the PID-control of the ambient temperature, the pressure can be controlled more efficiently. This leads to a more stable pressure measurement in the second and all following measurement campaigns.
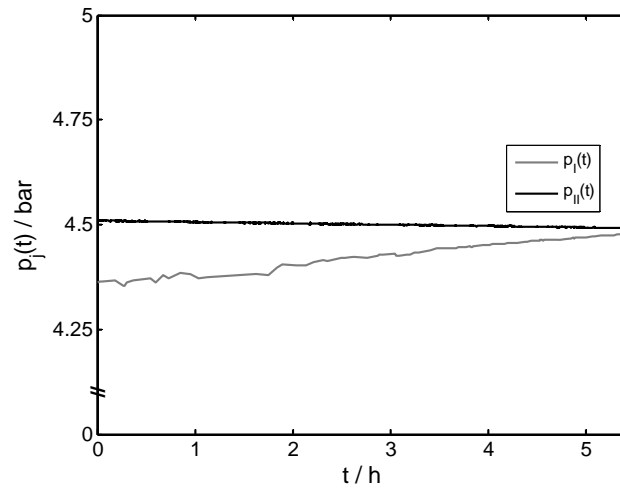
Fig. 28 Time dependent behavior of the pressure p of the working gas during a LDV-measurement of one half of the measurement points of a single x-y-cross-section (= 30points $\times$ 10min + t_{trav} $\approx$ 5.5h) within two measurement campaigns of the reference case (*I, II*); the more stable pressure of the second measurement campaign (*II*) reflects the improvements made on the SCALEX-Facility

The results of the improvements can also be seen in Fig. 29, which depicts the mean heating element temperature ϑ_{HE}, averaged over all RTDs, as a function of time. The period shown is equal to that in Fig. 28 and characterizes also a usual LDV-measurement of one half of an x-y-cross-section. Particularly due to a more stabilized pressure and a PID controlled ambient temperature, the mean heating element temperature is also more stable. The reason for that is that the heating element temperature is a function of the pressure p of the working gas and the ambient temperature ϑ_{amb}, because the heating elements are heated with a constant electrical input power $P = 43\mathrm{W}$ and the heat transfer coefficient depends on the pressure and the temperature of the surrounding gas. This correlation can be easily observed when strongly varying the pressure, e.g. from $p = 1\mathrm{bar}$ to $p = 4.5\mathrm{bar}$.
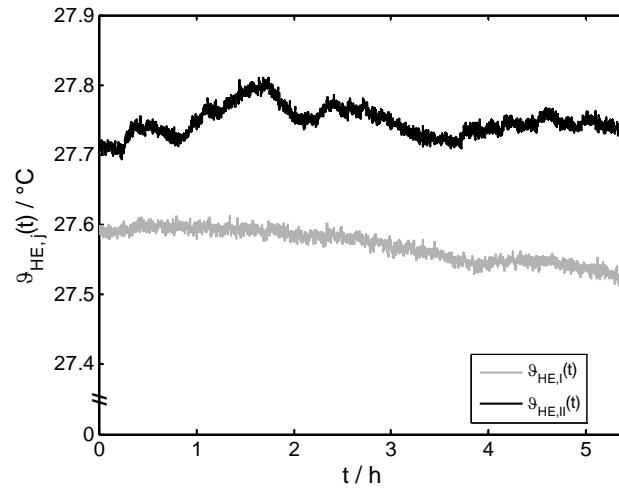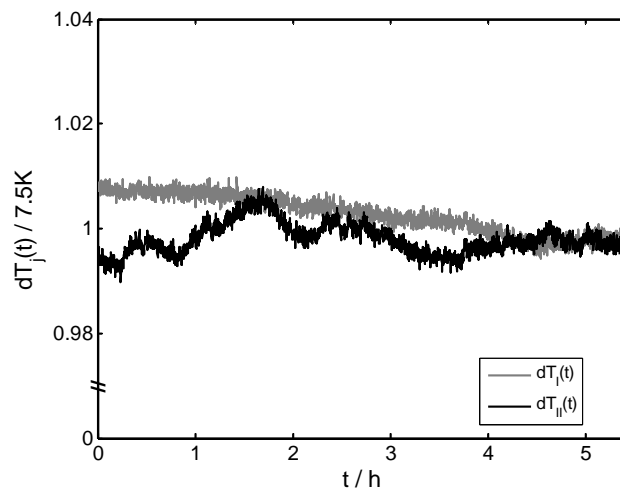
Fig. 29 Time dependent behavior of the mean temperature of the heating elements during a LDV-measurement of one half of the measurement points of a single *x-y*-cross-section (= 30points × 10min + t_{trav} ≈ 5.5h) within two measurement campaigns of the reference case (*I*, *II*); the more stable temperature of the second measurement campaign (*II*) reflects the improvements made on the SCALEX-Facility between campaign *I* and *II*

Fig. 30 shows the usual temporal behavior of the mean temperature difference ΔT, which is obtained by the mean value over all 6 RTDs of the inlet temperature and the mean value over all 12 RTDs of the heating elements. The temperature difference in the second measurement campaign is also more stable than the one of the first campaign. But the temperatures of the second campaign fluctuate more than in the first campaign, which can also be obtained in Fig. 29.

Fig. 30 Time dependent behavior of the mean temperature difference ΔT between the heating elements and the inlet during a LDV-measurement of one half of the measurement points of a single *x-y*-cross-section (= 30 points × 10min + t_{trav} ≈ 5.5h) within two measurement campaigns of the reference case (*I*, *II*); the more stable temperature difference of the second measurement campaign (*II*) reflects the improvements made on the SCALEX-Facility between campaign *I* and *II*

61

4.2.2 Characterization of the large-scale flow structure

According to the boundary conditions described above, Fig. 31 shows the results of the investigation of the large-scale flow structures for the case of mixed convection at $Ra = 1.93 \times 10^{10}$, $Re = 1.44 \times 10^5$, $Pr = 0.905$ and $Ar = 1.03$. The working gas is compressed SF_6 with a mean pressure of $p \approx 4.5$bar and the measurements were performed in a model room with a 1:10 reduced scale using the experimental setup as described in section 3. In Fig. 31a,c,e the results of the LDV-measurement are shown using vector fields on the basis of the measured vertical and horizontal velocity component $\boldsymbol{u} = (u, v)$. All pictures of the velocity flow fields are assembled pictures, where every vector depicts a measurement of $t = 10$min. That means that for generating one complete flow field picture for one x-y-cross-section it is necessary to measure 10×6points$\times 10$min $+ t_{trav} \geq 600$min ≥ 10h. The time t_{trav} represents the traversing time during the measurement. Due to the long measurement time, the vector field of the velocity distribution does neither represent a snapshot nor a temporal mean of the flow field. But because the velocity field is quite stable over a long period of time, the obtained vector fields are representable for the flow field. This can be proofed by the actual snapshots of the visualization of the large-scale flow structures shown in Fig. 31b,d,f. The snapshots of the flow visualization are taken from a greyscale movie of the flow and are depicted with light intensity encoded pseudocolors (violet = high; green = low). The light intensity is also a measure of the tracer particle concentration. The distribution of tracer particle concentration again reflects the large-scale flow structure. The comparison between the snapshots and the vector fields in Fig. 31 shows a very high similarity of the large-scale flow structures. When comparing the vector fields with the visualization movies, the similarity is even more obvious.

The found velocity distributions of the large-scale flow structure of the complete room differ very strong between the three investigated x-y-cross-sections at $z/D = [0.17, 0.49, 0.874]$. In the x-y-cross-section at $z/D = 0.874$, depicted in Fig. 31a,b, the flow runs upwards over almost the complete space between the heating elements and the ceiling of the room, i.e. the mean flow points upwards. In the right upper corner at $0.5 \leq x/L \leq 1$ and $0.7 \leq y/H \leq 1$ there exists two small counter-rotating eddies. The flow visualization in Fig. 31b approves the found velocity flow field in Fig. 31a. In the flow visualization the upward motion of the mean flow over almost the complete cross-section can be recognized by the homogeneous distribution of the tracer particles. Only in the range of the wall jets near the ceiling variations in the concentration of the tracer particles can be observed.
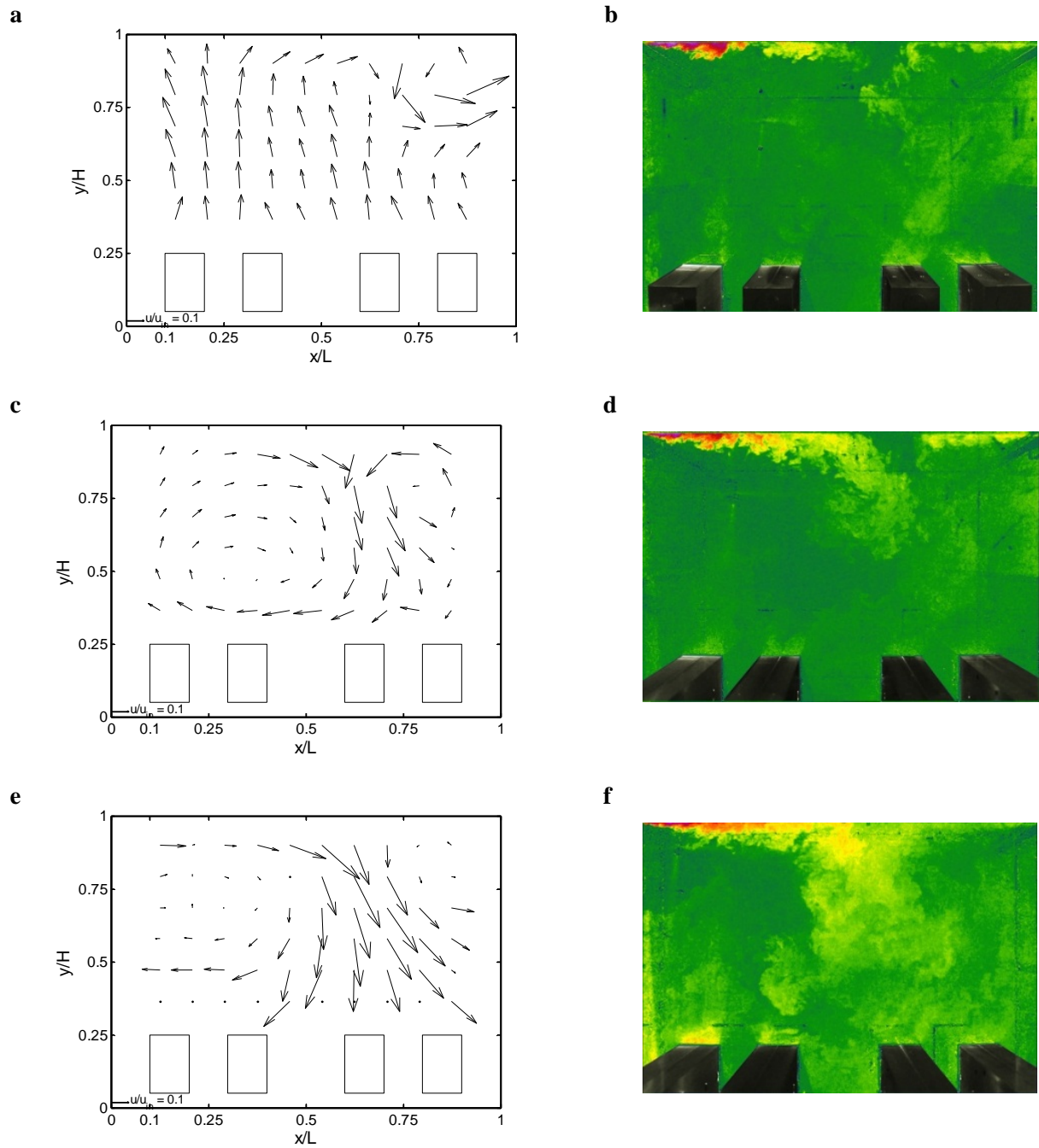
Fig. 31 Measured large-scale flow structures inside the small-scale model room at $p = 4.5$bar of the working gas SF_6 for the mixed convection case at $Ra = 1.93 \times 10^{10}$, $Re = 1.44 \times 10^5$, $Pr = 0.905$ and $Ar = 1.03$; [**a**, **c**, **e**] velocity field measured with LDV in the x-y-cross-section in depths of $z/L = [0.874, 0.49, 0.17]$, respectively; [**b**, **d**, **f**] pseudocolor snapshots of the visualization of the flow structure within the same x-y-cross-sections as the velocity fields

The large-scale flow structure in the middle x-y-cross-section of the room at $z/D = 0.49$ is depicted in Fig. 31c,d. In contrast to the first x-y-cross-section, the flow structure is dominated by two large eddies, which extend over the full space between the heating elements and the ceiling of the room. These two eddies are

63

compared to the results of the investigation of the isothermal flow not symmetrical. There is a smaller eddy on the left upper region at $0.65 \leq x/L \leq 1$ and $0.7 \leq y/H \leq 1$. This small eddy can be considered as a continuation of the one in the first x-y-cross-section. The big eddy spreads over 2/3 of the x-y-cross-section in the region $0 \leq x/L \leq 0.65$ and $0.25 \leq y/H \leq 1$. The core of the eddy is slightly shifted from its middle position to the position $x/L = 0.35$ and $y/H = 0.5$, which is closer to the heating elements. Here, the flow visualization, shown in Fig. 31d, also approves the found velocity flow field. The increased downward flow near the middle of the room can be recognized by the high particle concentration, which is depicted by an increased brightness. Although the snapshot do not show the clear shape of the large-scale flow structure, the counter-rotating asymmetrically dimensioned eddies can be recognized from the movie of the flow visualization.

Fig. 31e, f show the velocity field in the very back x-y-cross-section at $z/D = 0.17$. Similar to the previous described cross-section, the large-scale flow structures mainly comprises two counter-rotating large eddies of unequal size. As depicted in Fig. 31e, the size and the position of the larger one is similar to the one found at $z/D = 0.49$, i.e. in the region $0 \leq x/L \leq 0.65$ and $0.25 \leq y/H \leq 1$ and the smaller eddy has also the same size and position as the one in $z/D = 0.49$. Fig. 31e also shows a little bit different behavior of the absolute values of the velocity vectors. Here, the absolute velocities are slightly higher compared to the x-y-cross-section in the middle of the room ($z/D = 0.49$), i.e. the mean flow points downwards. This behavior of the large-scale flow structure can also be approved by the flow visualization, which is depicted in Fig. 31f. The large area of high particle concentration near the middle of the room shows the dominant downward flow.

In order to get an idea of the complete large-scale flow structure for the reference case $Ar \approx 1$, the flow structures of every single x-y-cross-section has to be considered. So, in the front plane ($z/D = 0.874$) an upward flow is dominant, the flow in the middle of the room ($z/D = 0.49$) is dominated by two unsymmetrically distributed large eddies and in the very back x-y-cross-section ($z/D = 0.17$) the mean flow points downwards. So, although the room has a 2-dimensional shape, i.e. the shape of the cross-section is constant in z-direction, the found large-scale flow structure show a strong 3-dimensional behavior.

An interpretation of the found flow structure might be that it can be separated into two main structures which influence each other by a temporal and spatial superposition. First, the two large eddies are doubtless caused by the forced convection generated by the inlet flow as found in the investigations of the isothermal case as described in section 4.1.2. In this case, the flow is nearly 2-dimensional with respect to

the z-direction and its dominant flow structures are consisting of two counter-rotating large eddies of equal size, which fills the whole room between the heating elements and the ceiling.

The upward and downward direction of the mean flow in the front and back cross-section are caused by a second large-scale flow structure, namely a single large eddy, which has the dimension of the full space above the heating elements. The single large eddy is rotating around the x-axis with the flow running from the front side to the back side near the ceiling and vice versa near the heating elements. This flow structure is caused by thermal convection, which is driven by the temperature difference between the inlet flow and the heating elements. Such flows are often found in classical Rayleigh-Benard-Convection (RBC). Furthermore, the analogy to RBC can also explain the unsymmetrical shape of the two large eddies, which are caused by the forced convection. The reason for that is that in natural convection the flow is always extended over the longest distance. The longest distance is the diagonal of the model room, i.e. from the left vertical edge in the front to the right vertical edge in the back of the model room.
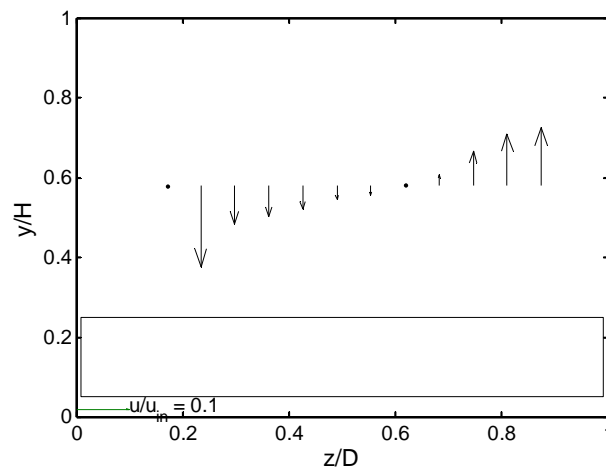
Fig. 32 Distribution of the vertical velocity component v along the z-axis at $x/L = 0.458$ and $y/H = 0.58$ measured in the measurement campaign I

The findings of the 3-dimensional shape of the large-scale flow structure can also be observed by a measurement of the vertical velocity component v along the z-axis of the room at one x-y-position. The result of this measurement is shown in Fig. 32 using a vector plot. Fig. 32 shows an upward motion of the flow in the range of $0.6 \leq z/D \leq 0.9$. In the range of $z/D < 0.6$ the direction of the flow points downwards. The twisted shape of the counter-rotating large eddies can be observed in Fig. 32 by the unsymmetrical velocity distribution, i.e. the zero point is shifted to the right with respect to the middle.

4.2.3 Reproducibility of the found flow structures

In order to check the reproducibility of the found flow structures two repetitions of the experiments were conducted with the SCALEX-facility using the same LDV-setup. While the first repetition of the measurement is done in the same way like the original one, in the second one the measurement procedure is changed in order to exclude a possible time dependence of the flow during the measurement. Therefore, a reduced measurement time of $t = 0.5$min is used for every measurement point. After the completion of all measurement points of a half cross-section, i.e. 5×6points = 30points, the measurement is repeated for each point. This procedure is repeated until a total measurement time of $t = 10$min per measurement point is reached, i.e. 20 repetitions per measurement point. However, this measurement procedure shall provide an averaging of the velocity of each point over a very long time period. In Fig. 33 the result of the first and second repetition (II, III) are compared with the first measurement (I). Here, the two most distinctive flow structures are chosen, the structures of the first cross-section at $z/D = 0.874$ and the ones of the middle cross-section at $z/D = 0.49$.

The flow in the first cross-section, shown in Fig. 33a,c,e, have a similar structure in every measurement campaign. The mean flow points upwards nearly over the complete measurement cross-section and near the right upper corner there are two small counter-rotating eddies. Moreover, every repetition shows the phenomenon that the velocity in the middle of the room has a minimum and increases towards the side walls. The main difference between the original and its repetitions is the different size and position of the two eddies as well as its absolute velocity. In detail, the two small eddies of the original campaign are situated closer to the right inlet than in the two repetitions. But they are always in the right side of the cross-section. In both repetitions, the two eddies are slightly smaller than in the original measurement campaign. In the third repetition, the two eddies are almost absent.

The shifting and the changed size of the eddies can also be seen in the middle cross-section, as depicted in Fig. 33b,d,f. Here, the difference between the found flow structures is more significantly. While the original structure show the two large eddies very clear, in both repetitions the large eddies are more disordered. Particularly in the first repetition, shown in Fig. 33d, the left large eddy is most disordered and shifted the most to the left side. But the basic flow structure, consisting of two large counter-rotating eddies, is always the same in every measurement campaign.
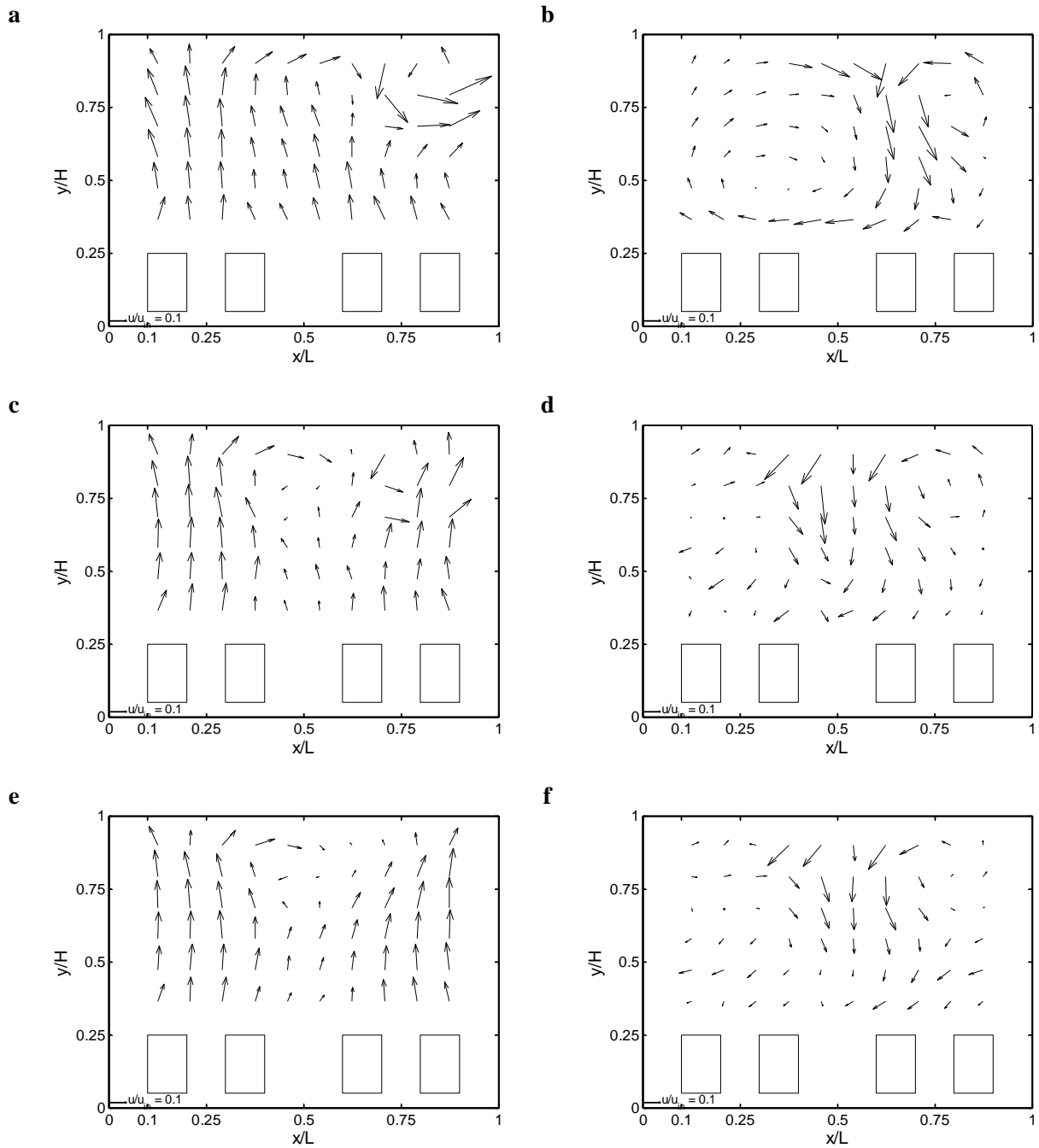
Fig. 33 Velocity fields of the flow structures measured in the *x-y*-cross-section *z/D* = [0.874, 0.49] in three different independent measurement campaigns *I-III* ([**a**,**b**]…*I*; [**c**,**d**]…*II*; [**e**,**f**]…*III*) with equal boundary conditions

Fig. 34 depicts a quantitative comparison of the absolute velocity $|\mathbf{u}| = (u^2 + v^2)^{0.5}$ of all three measurement campaigns. Fig. 34a shows the velocity distribution of one horizontal line at *z/D* = 0.874 and *y/H* = 0.687 over the complete range of *x/L*. All distributions have a similar shape. But particularly the velocity distribution of the original measurement (▼) differs from the others in the range of $0.4 \le x/L \le 0.6$. There, the velocity is much higher than the one of the first (■) and the second (●) repetition and the minimum is

67

slightly shifted to the right. This approves the finding from the full flow field. The first and the second repetition show very equivalent velocity distributions in the front x-y-cross-section at $z/D = 0.874$. The found behavior can also be observed, when comparing the distributions of the absolute velocity $|\boldsymbol{u}|$ in the middle cross-section at $z/D = 0.49$ and at the same height $y/H = 0.687$ over the full x/L-range as shown in Fig. 34b. Here, the first and second repetitions are very similar to each other, but the original data set differs from its repetitions. The maximum of the original set is shifted to the right side of the room and its value is higher than in the repetitions.
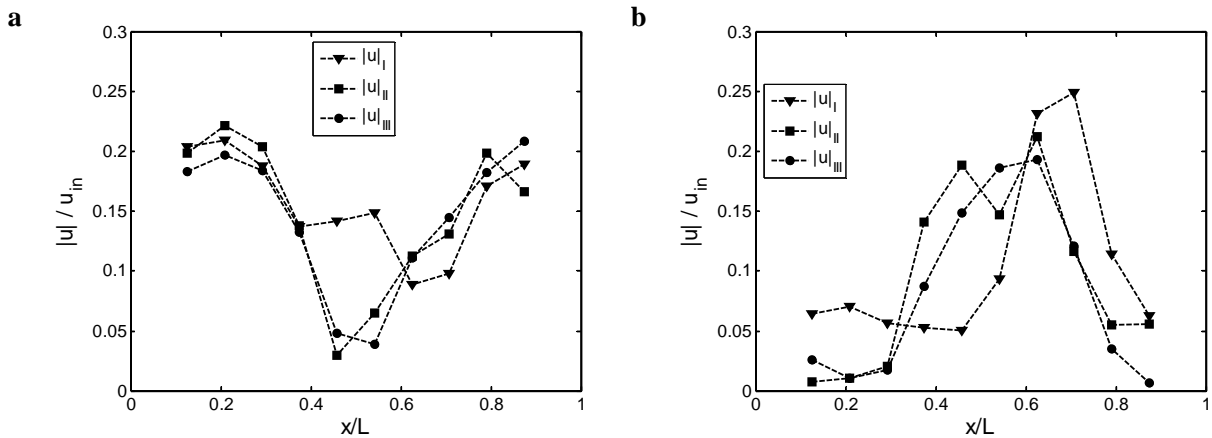
Fig. 34 Distributions of the absolute velocity $|\boldsymbol{u}|$ along the x-axis at $y/H = 0.687$ and (**a**) $z/L = 0.874$ and (**b**) $z/L = 0.49$ for measurement campaigns *I* (▼), *II* (■) and *III* (●)

The reproducibility check shows that it is possible to qualitatively and quantitatively reproduce the large-scale flow structure when considering equal boundary conditions. While there are differences between the original and its repetitions, the comparison of the two repetitions shows a very similar behavior of the flow with very small deviations. Particularly the distributions of the absolute velocities depicted in Fig. 34 show an almost congruent curse of the profiles.

As a methodological result of this consideration, the time averaging measurement procedure has a rather small effect on the results. Only the flow structures do appear more smoothly, when using the averaging LDV-measurement method. Thus, the large-scale flow structures can be assumed to be stationary.

The found differences between the original and the repetitions may result from different stable boundary conditions, because the repetitions were performed in an improved and thus modified setup of the SCALEX-facility. These improvements are the PID controlled ambient and inlet temperature, the improved tightness of the pressure vessel and an improved electromagnetic compatibility of the pressure sensor allowing a more precise adjustment of the pressure.

Thus, the Archimedes number in the original might be slightly lower, i.e. $\Delta Ar = 0.01$, so the flow is more dominated by the forced convection of the inlet flow. Another explanation of the differences in the flow structures between the original and its repetitions might be a minimal misalignment of the model room with respect to the gravitational acceleration. That means if there is a deviation in the alignment, the flow structures are trapped on one side of the room. By contrast, if the gravitational acceleration is perfectly aligned to the z-axis of the room, it would be possible that the flow structures are oscillating, i.e. the position of the large eddy in the middle of the room is frequently flipping from the left side to the right side of the room. However, such an oscillation of the full velocity field cannot be determined by the performed LDV-measurements, which is why the flow structures of the repetitions might show a time averaged velocity field of an oscillating flow structure, or vice versa: the flow is maybe trapped in its position in the original measurement campaign. In order to proof this issue, further measurement campaigns with Archimedes numbers in the range of $0.95 \leq Ar \leq 1.05$ has to be performed using imaging measurement methods.

4.2.4 Temporal behavior of the large-scale flow structures

The temporal behavior of the flow is studied using long-term LDV-measurements performed at single measurement points with a measurement time of $t = 8h$. The chosen measurement time is comparable to the characteristic time of one half of a measurement campaign of the full flow field as described above. The two long-term measurements were done in the middle x-y-cross-section at $z/D = 0.49$, $y/H = 0.687$, and $x/L = [0.375, 0.542]$. During the LDV-measurements the temperature distribution of the heating elements were recorded using the RTDs and the data logger of the SCALEX-facility. The curves shown in Fig. 35a for the first long-term measurement ($x/L = 0.375$) and in Fig. 35b for the second one ($x/L = 0.542$) are the fluctuations of the temperature around the spatially averaged values of the three sensors of each heating element normalized to the temperature at $t = 0$. While the temperatures of the heating elements 3 and 4 (bright lines) show a very stable and smooth behavior, the fluctuations of the temperatures of the heating elements 1 and 2 (dark lines) are very strong. This behavior can be observe in Fig. 35a as well as in Fig. 35b. Typical periods of the fluctuations are in the range of $t = 1h$. But there are also fluctuations with periods of the order of several hours. In Fig. 35a the fluctuations show a strong offset in the range of $3h \leq t \leq 6h$. In Fig. 35b, there also exists an offset but with an inverted time range. There, the temperature is decreased in the range of $2.5h \leq t \leq 5.5h$. The periods of these long-term fluctuations are larger than the measurement time. The unsymmetrical distribution of the fluctuations over the heating elements leads to the assumption that the unsymmetrical large-scale 3-dimensional flow structure also has a fluctuating behavior.
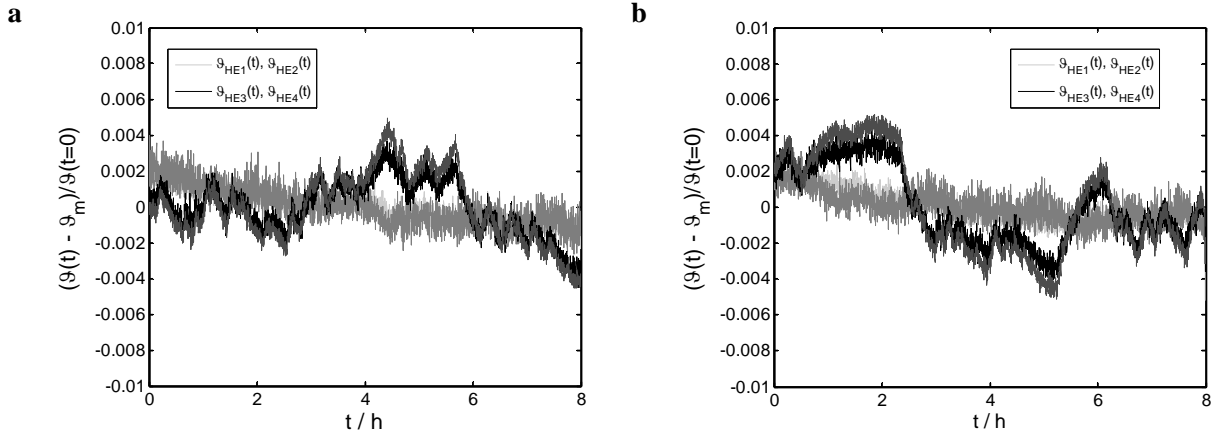
Fig. 35 Fluctuations of the spatially averaged heating element temperatures ϑ_{HE1}, ϑ_{HE2}, ϑ_{HE3}, ϑ_{HE4} as a function of time t for the first (**a**) and the second (**b**) long term measurement campaign

The assumption can be proofed by the results of the LDV-measurements shown in Fig. 36 and Fig. 37, whereas Fig. 36 show the first long-term measurement at $x/L = 0.375$ and Fig. 37 the second one at $x/L = 0.542$, respectively. Fig. 36a and Fig. 37a depict the horizontal velocity component u as a function of time. Fig. 36b and Fig. 37b depict the vertical velocity component v as a function of time. Both values are shown as moving average with an interval of $N = 2.5 \times 10^4$ samples using full overlapping, i.e. that the sample step is $n = 1$. The insets within all figures show the true velocity signal of the LDV-measurement with 9.8×10^5 samples, which includes the turbulent fluctuations of the velocity.
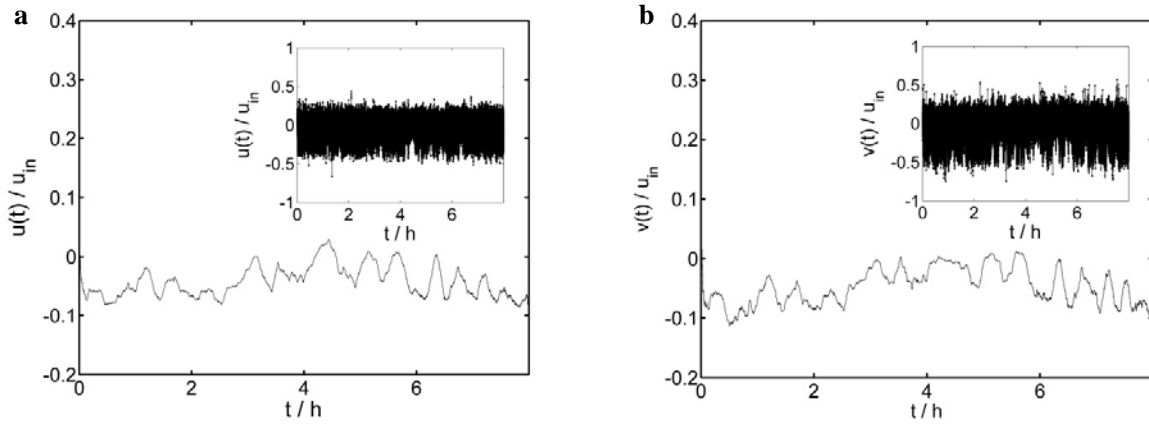
Fig. 36 a horizontal velocity component u as a function of time t using a moving average measured at $(x/L, y/H, z/D) = (0.375, 0.687, 0.49)$ (first long term measurement); **b** vertical velocity component v as a function of time using a moving average; the insets show the raw data; the moving average intervall includes $n = 2.5 \times 10^4$ data points and full overlapping of the intervalls

Fig. 36a and Fig. 36b show a distinct large-scale fluctuation with typical period times of around $t = 1h$. Larger fluctuations cannot be clearly observed from the temporal behavior. The found large-scale fluctuations of the mean velocity are approximately 5-times smaller than the turbulent fluctuations. In

70

contrast to the findings in Fig. 36, Fig. 37 shows a very smooth temporal behavior of the mean velocity of both the horizontal component u as well as the vertical component v. The fluctuations of the horizontal as well as of the vertical velocity component at $x/L = 0.542$ are very small compared to the ones at $x/L = 0.375$. The reason for this unsymmetrical behavior might be that the first measurement position is closer to the unstable region of the vortex core of the large eddy on the left side of the room. The second position is within the colliding wall-jets between both eddies, which implies a more stable flow. This assumption can be approved by the increased vertical velocity component v at $x/L = 0.542$ compared to $x/L = 0.375$.
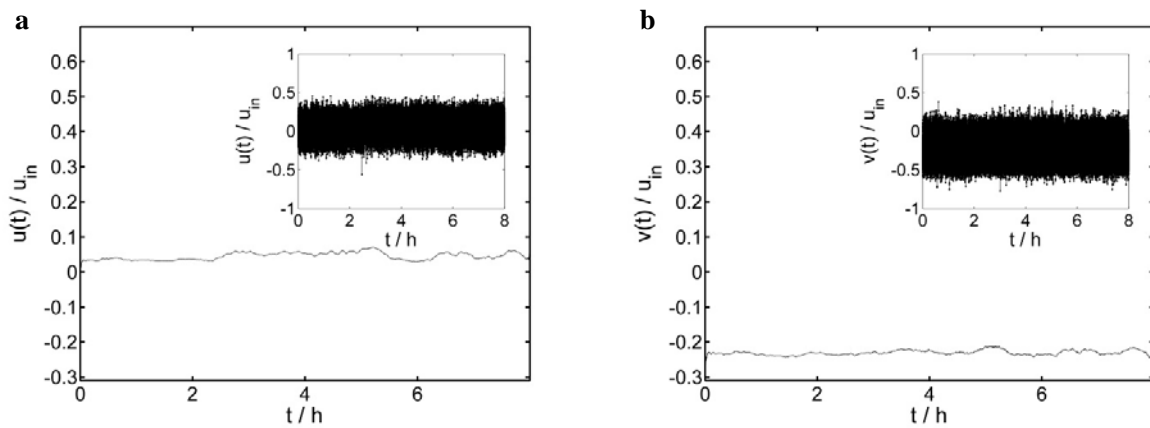
Fig. 37 a horizontal velocity component u as a function of time using a moving average measured at $(x/L, y/H, z/D) = [0.542, 0.687, 0.49]$ (second long term measurement); **b** vertical velocity component v as a function of time using a moving average; the insets show the raw data; the moving average intervall includes $n = 2.5 \times 10^4$ data points and full overlapping of the intervalls

The comparison between the velocity measurements and the temperature measurements is depicted in Fig. 38. The black lines show the fluctuations of the moving average of the velocity components u and v. The red lines show the fluctuations of the spatially averaged temperatures of heating elements 3 and 4. In order to achieve fluctuations of similar value, the temperature fluctuations are multiplied by the factor 10. The measurement time is synchronized afterwards using a reference signal, which can be found in the velocity signal as well as in the temperature signal. The reference signal was generated using the compressor of the particle generator by generating a very huge amount of particles. This leads to a pressure loss of the working gas, which again leads to a significant increase of the temperature due to the pressure dependent heat transfer at the heating elements. The reference signal can be detected on the LDV-system by a sudden increase of the data rate due to the large amount of particles generated with the particle generator. The accuracy of the time synchronization can be estimated to $\Delta t \approx 1\text{min}$, which is compared to the measurement time very small but is not applicable to use a cross-correlation. But the result of the superposition of both signals, depicted in Fig. 38, show that there exists a correlation between both, the velocity and the temperature fluctuation of the heating elements 3 and 4. In this correlation the

temperature and the velocity influence each other directly. That means an increase of the mean temperature of the heating elements results in an increase of the mean velocity. Furthermore, the increase of the mean velocity also leads to a decrease of the mean temperature of the heating elements. As shown in Fig. 38, the correlation of the velocity at position $x/L = 0.375$ and the heating elements 3 and 4 is very strong.
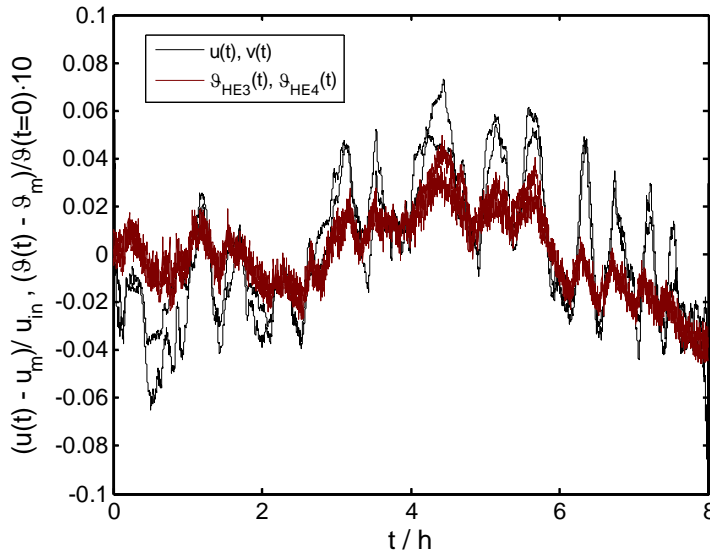
Fig. 38 Superimposed velocity $\boldsymbol{u} = (u, v)$ and heating element temperatures ϑ_{HE3}, ϑ_{HE4} as a function of time for the first measurement campaign at $[x/L, y/H, z/D] = [0.375, 0.687, 0.49]$

The superposition of the fluctuations of the mean temperature and the velocity fluctuations at $x/L = 0.542$ is shown in Fig. 39. The velocity fluctuations at $x/L = 0.542$ show only a weak correlation with the temperature fluctuations compared to the first position at $x/L = 0.375$. The only significant correlation can be found at the range of $4\text{h} \leq t \leq 6\text{h}$.

However, the long-term velocity measurements show a significant oscillation of the complex three-dimensional large-scale flow-structures with very long time-scales. But, because the amplitudes of the oscillations are small, the assumption of a stationary flow structure remains valid. As a phenomenon of the oscillations, they affect the heat flux of the heating elements and cannot be found throughout the whole room, as indicated by the findings of Fig. 39. The most obvious explanation of the origin of the oscillations is the oscillation process found in the isothermal case. But this would not consider the dynamics resulting from the correlation of the heat flux on the heating elements and the flow velocity. So, for the moment, there is no reasonable explanation for the reason of the oscillation, which necessitates further investigations.
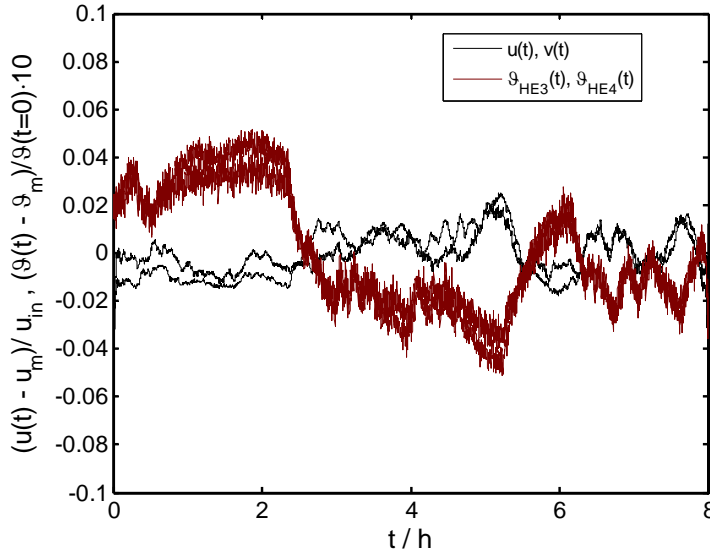
Fig. 39 Superimposed velocity $\boldsymbol{u} = (u, v)$ and heating element temperatures ϑ_{HE3}, ϑ_{HE4} as a function of time for the first measurement campaign at $(x/L, y/H, z/D) = (0.5416, 0.687, 0.49)$

In order to investigate the formation of the large-scale flow structure, the temperature is monitored during the adjustment of the boundary conditions of the reference case of $Ar = 1.03$. Fig. 40 shows the Archimedes number Ar and the temperatures of heating element 4 as a function of time. The time interval shown only reflects a detail of the full adjustment of the boundary conditions, which needs approximately $t = 6$h to reach a stable state. The transient behavior is generated by first switching on the AC1, which gives a flow dominated by forced convection inside the model room. After that the power of the heating elements is switched on, which causes an increase of Ar until the equilibrium is reached, as shown in Fig. 40a. The increasing heating element temperatures are shown in Fig. 40b, which depicts each of the three temperature sensors and the spatially averaged temperature of the heating element 3. There, ϑ_7, ϑ_8, and ϑ_9 represent the temperature in the front, middle and back of the heating element. At the beginning the middle of the heating element has the highest temperature and the front and back are cooler. The temperatures of the front and back are close to each other. The Archimedes number $Ar = 1$ is reached after reaching a sufficient high mean heating element temperature at $t = 3.64$h. At this point the temperature distribution over the heating element changes significantly, as shown in Fig. 40b. Henceforward the temperature difference between the front and the back of the heating element is strongly increased, while the temperature in the middle of the heating element is unchanged. The mean heating element temperature also does not change at this time, as shown in Fig. 40. The reason for this behavior might be a sudden transition of the flow structure from a two roll structure dominated by forced convection to the 3-dimensional structure found in the velocity measurements and visualizations that is dominated by both,

natural and forced convection. Due to the fact that the phenomenon was not reproducible, the mechanisms of the found transition are not fully clear and need further investigations.
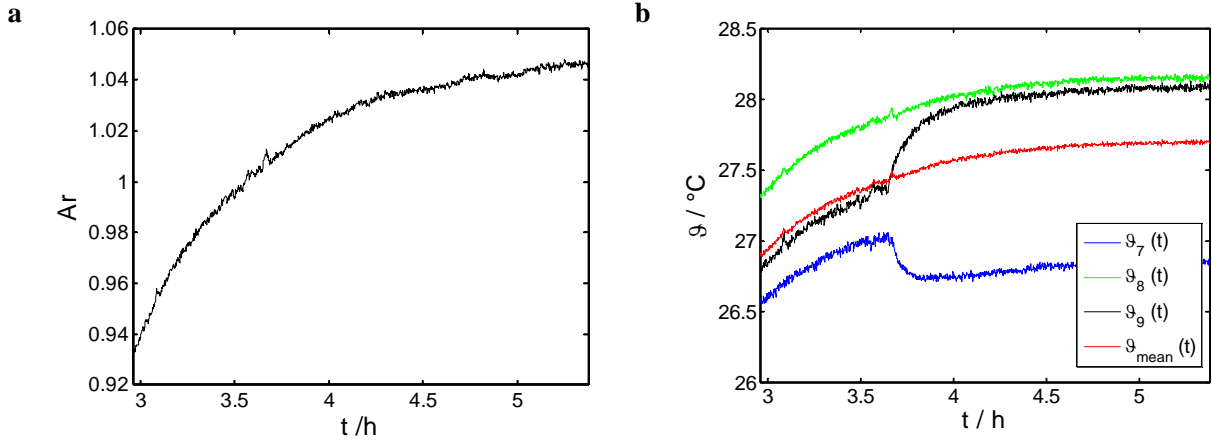
Fig. 40 a Archimedes number Ar as a function of time during the adjustment of the boundary conditions of the mixed convection; **b** temperatures of the heating element 3 as a function of time with ϑ_7, ϑ_8, ϑ_9 as temperatures of the sensors in the back, middle and front cross-section of the model room, repectively; ϑ_{mean} reflects the spatially averaged temperature

4.2.5 Comparison between small-scale and full-scale experiment

A comparison with an experiment in a model room with 10-times larger dimensions is done in order to perform a first validation of the new method for studying mixed convection in a room with reduced size. To realize the comparison between the two velocity data sets, the velocities are normalized to the corresponding inlet velocities, i.e. $u_{in} = 0.8$m/s for the full-scale experiment and $u_{in} = 0.293$m/s for the small-scale experiment. The data of small-scale experiment is taken from the second repetition (measurement campaign III) of the LDV-measurement of the velocity field.

A qualitative comparison of the found large-scale flow structures is shown in Fig. 41 whereas the flow structures found in the small-scale experiment are shown in Fig. 41a and those of the full-scale experiment are shown in Fig. 41b. The shown slices depict an interpolation of the absolute velocity $|u|$ on the basis of the single point measurement shown in Fig. 27. The absolute velocity of the small-scale experiment is based on the u- and v-component of the velocity vector due to the usage of the 2D-LDV-setup. The absolute velocity of the full-scale experiment is directly measured using an omnidirectional velocity sensor, i.e. the full-scale absolute velocity includes all components of the velocity vector u. But it cannot be separated into each velocity component u, v, and w.
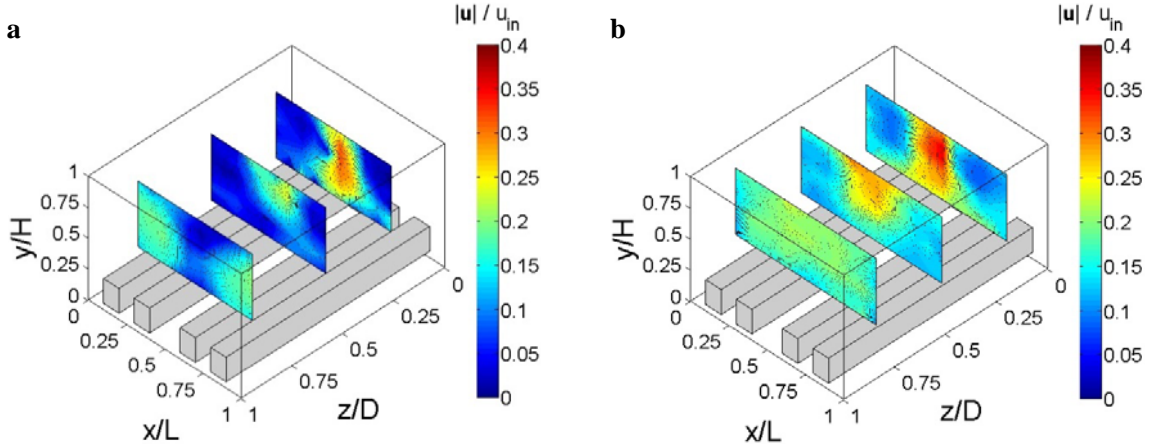
Fig. 41 Comparison of the large-scale flow structures for the parameter set ($Re \approx 1.5 \times 10^5$, $Ra \approx 2.0 \times 10^{10}$, $Ar \approx 1$) found in the small-scale (**a**) and the full-scale experiment (**b**); the absolute velocities $|u|/u_{in}$ are shown for the x-y-cross-sections at $z/D = [0.17, 0.49, 0.874]$; the velocity values are interpolated on the basis of the measurement points and are encoded with the color gradient from red to blue shown next to the diagrams; the cross-sections are shown in 3D-view, the grey bars at the bottom of the room depict the heating elements;

As shown in Fig. 41a, the 3-dimensional large-scale flow structure found from the vector plots in Fig. 31 can be recognized in the distribution of the absolute velocity $|u|$ as well. Particularly the asymmetry in z-direction can be clearly recognized, when comparing the first and the last slice in Fig. 41a. But also the found asymmetry in the x-y-cross-section can be found, especially in the slices at z/D = 0.49 and z/D = 0.17.

The distribution of the absolute velocity $|u|$ found in the full-scale experiment also shows an asymmetrical large-scale flow structure. Particularly the asymmetry in z-direction can be found in the shown velocity distribution, when comparing all slices. At $z/D = 0.874$ the absolute velocity is nearly homogenously distributed over the complete cross-section. The cross-sections at $z/D = 0.49$ and $z/D = 0.17$ show almost the same velocity distribution, i.e. the absolute velocity is small close to the walls with a maximum in the range $0.4 \leq x/L \leq 0.6$, that is near the middle of the room. Furthermore, the distribution of the absolute velocity at $z/D = 0.17$ show a more distinct distribution of the flow with higher velocity values in the range of the maximum than in cross-section at $z/D = 0.49$. Although the results of the full-scale experiment do not provide an information about the direction of the flow, the large-scale flow is very similar to the one found in the small-scale experiment.
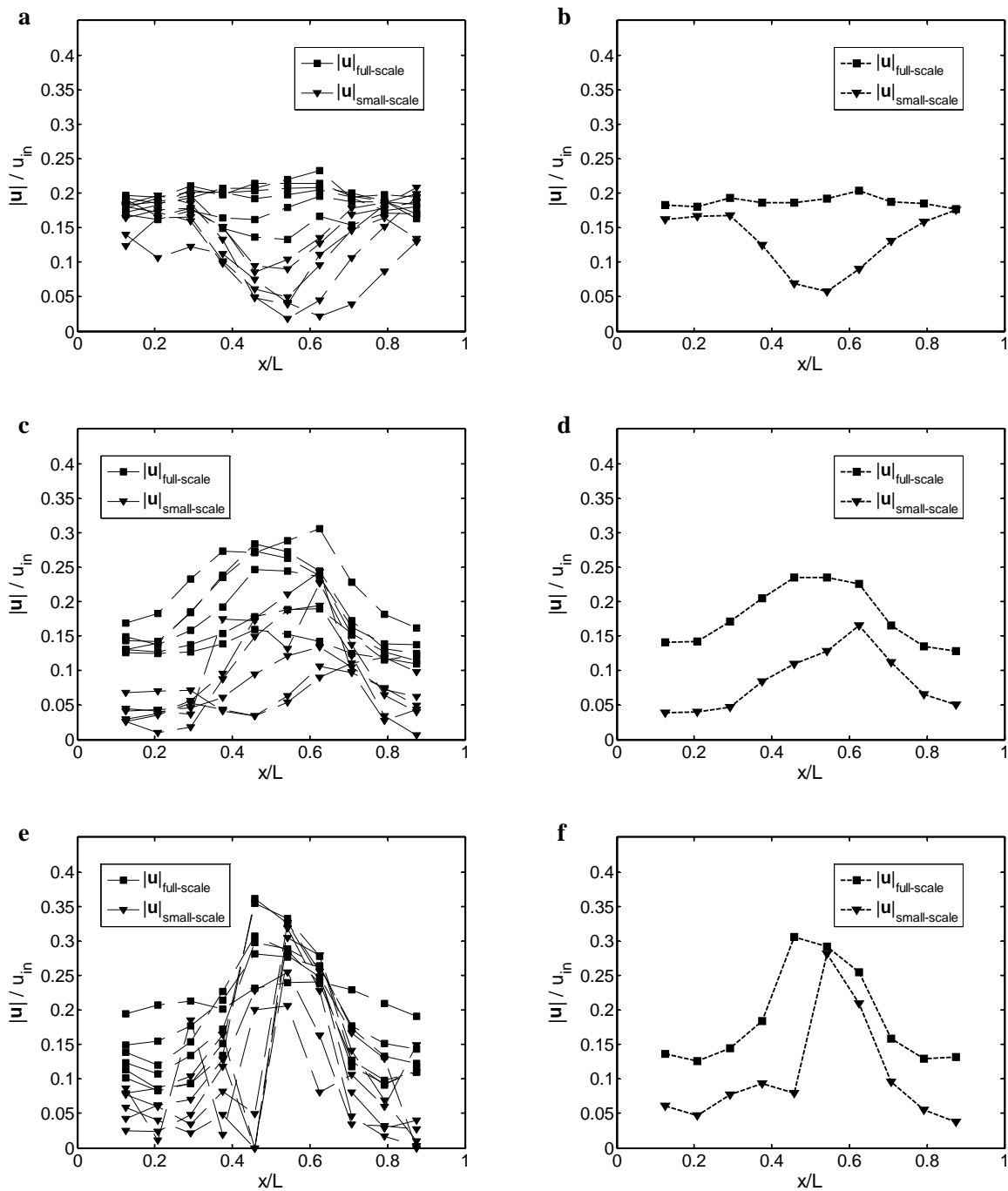
Fig. 42 Comparison of the velocity distributions over the length L between the full-scale and small-scale experiment: **a**,**c**,**e** velocity distributions in every measured height H; **b**,**d**,**f** mean velocity distribution averaged over height H

Fig. 42 depicts a quantitative comparison of the distribution of the absolute velocity $|\boldsymbol{u}|$ in the small-scale and the full-scale experiment in the three x-y-cross-sections. The diagrams in Fig. 42a,c,e show the absolute velocities as a function of x/L for every investigated height y/H. The curves in Fig. 42b,d,f are the

distributions of the absolute velocities averaged over the height of the room, which reflect the mean flow for each x-y-cross-section.

Comparing the velocity distributions for each x-y-cross-section, the 3-dimensional flow structure can be recognized from the results of the full-scale and the small-scale experiment. But there are significant deviations in the velocity values between the full-scale and the small-scale results. In the cross-section at $z/D = 0.874$, shown in Fig. 42a,b, the deviations are high in the range of $0.3 < x/L \leq 0.75$. While the velocity distribution of the flow in the full-scale is nearly constant over the full length of the room, the velocity distribution of the flow in the small-scale has a distinct minimum within the above mentioned range. At $x/L \leq 0.3$ and $x/L > 0.75$, the velocities are very similar.

As depicted in Fig. 42c,d, the velocity distributions at $z/D = 0.49$ show a very similar behavior. Particularly the curves of the spatially average of the absolute velocity show a very similar curse. That means that the absolute velocity of the full-scale experiment as well as the velocity distribution of the small-scale experiment show a maximum near the middle of the room at $x/L = 0.542$. But there is an offset between the absolute values of the velocity, i.e. the velocity of full-scale experiment, which includes all three velocity components, is nearly constantly higher than the velocity of the small-scale experiment. This finding can also be observed when comparing the velocity distribution in the x-y-cross-section at $z/D = 0.17$, as shown in Fig. 42e,f. There, the curse of the velocity with respect to width of the room in the full-scale experiment is similar to the one in the small-scale experiment as well. By contrast to the previous findings, the velocities near the middle of the room at $x/L = 0.542$ are nearly the same. So, there is an offset, but it is not constantly distributed over the length L of the room.

As a conclusion of the comparison, the flow structures are qualitatively the same with quantitative deviations of the absolute velocity $|\boldsymbol{u}|$. Thus, the flow structure of the full-scale experiment can be reproduced in the small-scale experiment, which can be regarded as a qualitative validation of the new scaling method. The most reasonable explanation of the quantitative deviations might be a strong influence of the second horizontal velocity component w. So, due to the fact that the third velocity component is included the full-scale data and neglected in the small-scale data, $|\boldsymbol{u}|_{full\text{-}scale} > |\boldsymbol{u}|_{small\text{-}scale}$ if $|w| > 0$. An indication of this assumption can be obtained from the velocity distributions in Fig. 42e,f. There, the maximum velocities are at the same position $x/L = 0.542$ and have the same value $|\boldsymbol{u}|/u_{in} \approx 0.29$. This is probably caused by the fact that at this the point $w = 0$, which is again caused by the strong downward flow at this position, as found in the velocity fields in Fig. 31 and Fig. 33.

4.2.6 Characterization of the draft risk DR

Fig. 43 depicts the distribution of the draft risk DR for the case of mixed convection with the dimensionless numbers of $Ra = 1.93 \times 10^{10}$, $Re = 1.44 \times 10^5$, $Pr = 0.905$ and $Ar = 1.03$. In detail, Fig. 43a,c,e show the distribution of DR within each x-y-cross-section at $z/D = [0.874, 0.49, 0.17]$ and Fig. 43b,d,f show the distribution of DR in x-direction at $y/H = 0.58$ for every x-y-cross-section. The height $y/H = 0.58$ seems to be most significant within the room concerning the occupied zone. The draft risk DR is again determined on the basis of eq. (5). But, in contrast to the determination of DR for the isothermal case, a linear gradient is applied to the temperature ϑ_a in vertical y-direction between the heating elements and the inlets, which assumes the lowest temperature at $y/H = 0.9$ and the highest temperature at $y/H = 0.3667$. The temperature difference between each point is defined as $dT = (\vartheta_h - \vartheta_{in})/n$ with ϑ_h as the temperature of the heating elements, ϑ_{in} as the temperature of the inlet flow and n as the number of measurement points in y-direction. Thus, the temperature difference $dT = 1.25K$. The absolute velocity data necessary for the calculation of the draft risk is taken from the small-scale experiment and converted to the full-scale using $|\boldsymbol{u}|_{full\text{-}scale} = |u|_{in,full\text{-}scale}/|u|_{in.small\text{-}scale} \cdot |\boldsymbol{u}|_{small\text{-}scale} = 2.73 \cdot |\boldsymbol{u}|_{small\text{-}scale}$. The turbulence level Tu is determined out of the r.m.s.-data of the flow velocity using eq. (6). The color legend of the distributions of the draft risk in Fig. 43a,c,e are each normalized to its maximum value, i.e. dark color refers to high values and bright color refers to low values. Every square in Fig. 43a,c,e relates to one LDV measurement point with the actual point in the middle of the square. The draft risk is set to $DR = 0$ when $|\boldsymbol{u}|_{full\text{-}scale} < 0.05\text{ms}^{-1}$.

The large-scale flow structure can be recognized from the distributions of the draft risk DR in the case of mixed convection at the reference parameter set, shown in Fig. 43a,c,e. So, the draft risk is following the highest velocities, i.e. regions with high velocities causing a high draft risk. Thus, in the x-y-cross-section at $z/D = 0.874$ the draft risk is high over the heating elements and low in the middle of the room. This can also be recognized in the draft risk distribution along x/L at $y/H = 0.58$, shown in Fig. 43b. There, the draft risk has a minimum near $x/L = 0.45$ and show very high values, i.e. $DR \approx 15\%$, on both sides with respect to the middle at $x/L \leq 0.3$ and $x/L \geq 0.7$. By contrast, in the x-y-cross-sections at $z/D = 0.49$ and $z/D = 0.17$, shown in Fig. 43c-f, the maximum of the draft risk is situated very close to the mid-plane. As depicted in Fig. 43d, the maximum draft risk in the middle x-y-cross-section is lower than in the other ones, i.e. $DR < 15\%$. The x-y-cross-section in the back of the room at $z/D = 0.17$, which is shown in Fig. 43e,f, comprises the highest DR values with the maximum of $DR \approx 25\%$.
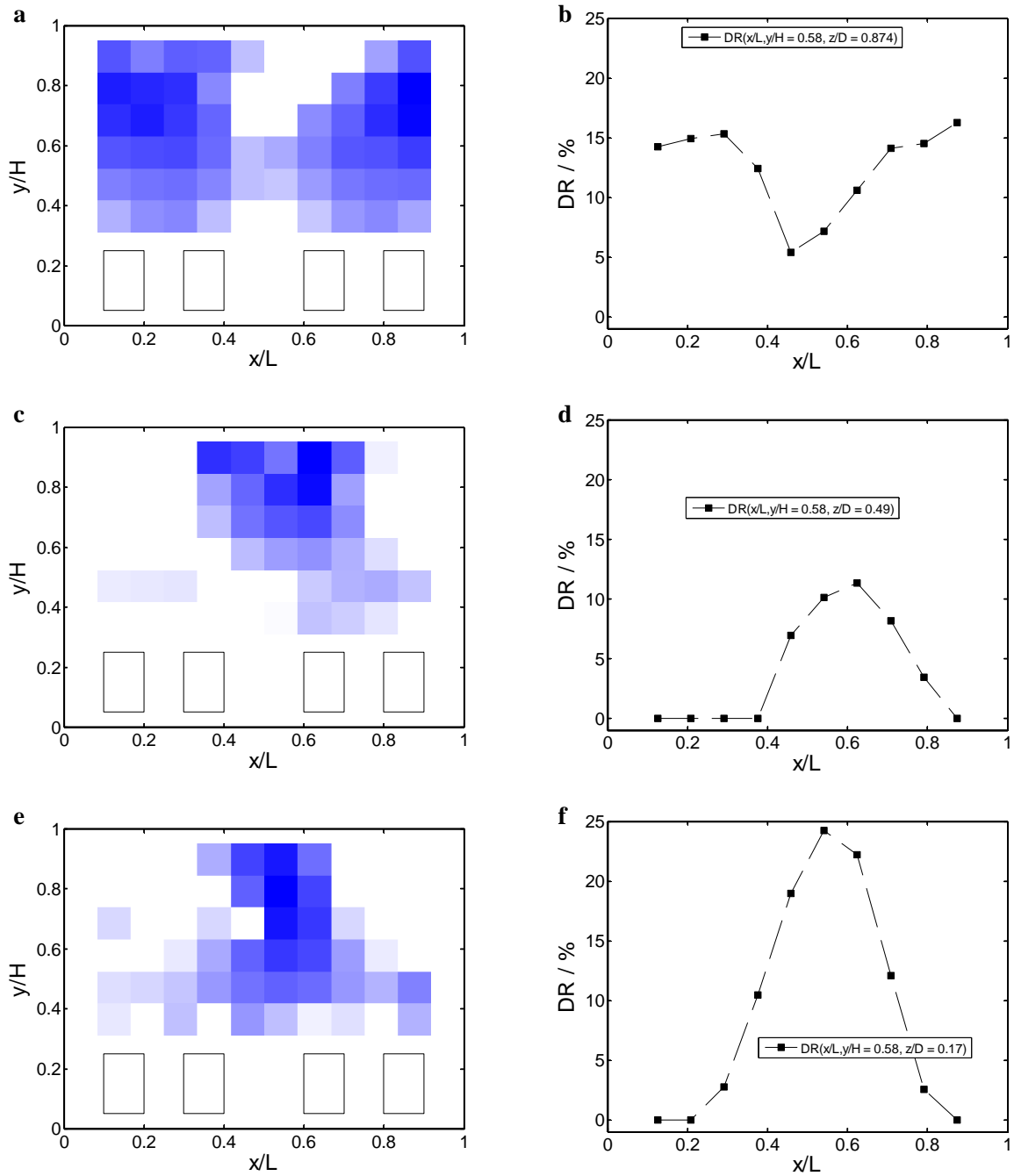
Fig. 43 Distribution of the draft risk *DR* in the case of mixed convection for every *x*-*y*-cross-section (**a**, **c**, **e**) as well as in *x*-direction for the single height *y/L* = 0.58 (**b**, **d**, **f**); the *DR* values refer to the full-scale determined out of the small-scale experiment; the color legend in the *x*-*y*-cross-section is normalized to maximum *DR* value of each *x*-*y*-cross-section, with the darkest color depicting the highest value; all *DR* values with |*u*| < 0.05ms^{-1} are set to *DR* = 0; **a**,**b** *z/D* = 0.874; **c**,**d** *z/D* = 0.49; **e**,**f** *z/D* = 0.17

Related to the maximum permissible value of the draft risk *DR* = 15%, the found flow in the case of mixed convection do not have a comfortable climate in every position of the occupied zone at $0 \leq x/L \leq 1$ and *y/H* = 0.58. In fact, there is a very high draft risk in the back of the room, where the flow has a very strong

downward motion. But, also in the front of the room, where there is a nearly uniform upward flow, the draft risk also exceeds the maximum permissible value. So, the requirements related to the draft risk to achieve a thermally comfortable indoor airflow are not full-filled in the front and the back of the room. A comparison of the draft risk distribution with the full-scale experiment was not possible due to unavailable r.m.s.-data of the absolute flow velocity.

Referring the findings of the draft risk distribution to a passenger cabin, this would mean that the passengers in the front and the back feel uncomfortable due to the draft. Especially the passengers at the windows in the front of the cabin and the one on the aisle seats in the back of the cabin feel very uncomfortable, while the passengers in the middle of the cabin feel more comfortable.

4.3 Possible sources of errors

Due to the complexity of the SCALEX-facility, the used scaling method and the measurement equipment, the occurring errors have a large diversity. In the following section, the possible sources of errors are discussed with the focus on the experimental scaling method and the performed velocity measurements.

Although the scaling method for the case of mixed convection presented in this work has a very high accuracy regarding the full set of dimensionless numbers, there are nevertheless deviations between the full-scale and the small-scale model. First of all, the main deviation can be found in the Prandtl numbers between air and compressed SF_6, which amounts to $(Pr_{SF6}/Pr_{air.0} - 1) = 27.15\%$ as shown in Tab. 4. This error is caused by the material properties of SF_6 and its compression to $p = 4.517bar$. Even the usage of air as the working gas at a pressure of $p = 32.84bar$, which is necessary to achieve $m = 10$, would not solve the problem perfectly due to a deviation of $(Pr_{air}/Pr_{air.0} - 1) = 2.69\%$. Further, a deviation of the Prandtl number leads to a deviation of the Archimedes number Ar. When assuming $(Re_{SF6}/Re_{air.0} - 1) = 0$ and $(Ra_{SF6}/Ra_{air.0} - 1) = 0$, then the deviation of the Archimedes number yields $(Ar_{SF6}/Ar_{air.0} - 1) = 21.35\%$. In order to reduce the deviations of the full set of the dimensionless number, the Reynolds number is reduced by decreasing the inlet velocity u_{in}. The criterion for choosing the deviation of the Reynolds number is defined as $\Delta Ar/\Delta Re = 2$, which yields $(Re_{SF6}/Re_{air.0} - 1) = 5.74\%$ and $(Ar_{SF6}/Ar_{air.0} - 1) = 11.48\%$. Hence, the method of scaling used in the present work do not provide full similarity, but a partial similarity with very low errors with respect to the full set of dimensionless numbers.

Beside the above stated major errors regarding the dimensionless numbers, there are also minor errors concerning the material properties and the characteristic values like the length L, the inlet velocity u_{in} and the temperature difference ΔT. The errors of the material properties are mainly caused by the

determination of the material properties itself and the measurement of the pressure and the temperature. But also the purity of the working gas can have an impact on the accuracy of the material properties. The error of the inlet velocity is mainly affected by the velocity measurement, but also by the shape of the inlet nozzle and the constancy of the fan frequency. Also imperfections of the model room and the model room alignment with respect to the gravity acceleration can influence the results. Anyway, there are a lot more errors regarding the experimental setup. All the above mentioned errors can be regarded as systematically errors, i.e. they can be determined and are always constant throughout each measurement.

Due to the statistical behavior of the velocities in turbulent flows, the measurement of the velocity always comprises statistical errors. These statistical errors are summarized in the confidence interval Δu, which is defined as

$$\Delta \boldsymbol{u} = \pm \frac{2\sigma(\boldsymbol{u})}{\sqrt{N}} \tag{44}$$

with $\sigma(\boldsymbol{u})$ as the standard deviation and N as the number of statistically independent values. The real value of the velocity is with a probability of 95.5% within the above defined confidence interval. The standard deviation and the number of statistically independent values can be determined from the time series of each velocity measurement. The standard deviation is determined using eq. (11). The number of statistically independent values N is defined by

$$N = \frac{t_{mess}}{t_{corr}} \tag{45}$$

with t_{mess} as the full measurement time and t_{corr} as the correlation time. The correlation time can be determined from the auto-correlation function $R_{\phi\phi}$ in eq. (12). As an example, Fig. 44 shows two typical auto-correlation functions $R_{uu}(t)$ for the horizontal velocity component in an arbitrary position within the room for the isothermal and the mixed convection case. Moreover, Fig. 44a and Fig. 44b show the auto-correlation function with and without a distinct oscillation, respectively. In the case of an occurring oscillation in R_{uu}, the correlation time t_{corr} is equal to the first zero of the auto-correlation function $t_{corr} = t(R_{uu} = 0)$. If the oscillation is absent the correlation time is defined by $t_{corr} = 2t_{int}$ with t_{int} as the integral time. The integral time t_{int} is again defined as the time where the areas A_1 and A_2, shown in Fig. 44b, are equal.
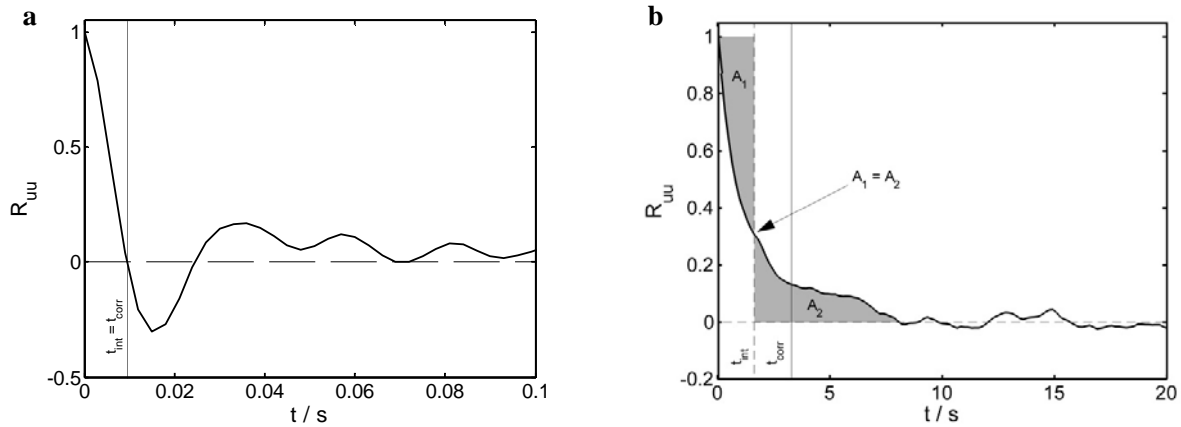
Fig. 44 Auto-correlation functions $R_{uu}(t)$ for **a** the isothermal case at $(x/L, y/H, z/D) = (0.0825, 0.997, 0.5)$ for $Re = 2.4 \times 10^4$ and **b** for the case of mixed convection at $(x/L, y/H, z/D) = (0.8746, 0.58, 0.49)$ for the reference set of dimensionless numbers; the diagrams show the two types of the determination of the correlation time t_{corr}: **a** first zero of R_{uu}; **b** t_{corr} as a function of the integral time t_{int}

Fig. 45 shows velocity profiles, typical for the isothermal and mixed convection case, with respect to the results of the error estimation as described above. The confidence intervals are shown by error bars at each point. Fig. 45a shows the profile of the horizontal velocity u for the isothermal case along y/L at $x/L = 0.0825$, and $z/D = 0.5$ for $Re = 2.4 \times 10^4$. Fig. 45b shows the profile of the vertical velocity v for the case of mixed convection along x/L at $y/L = 0.58$, and $z/D = 0.49$ for the reference parameter set of dimensionless numbers.
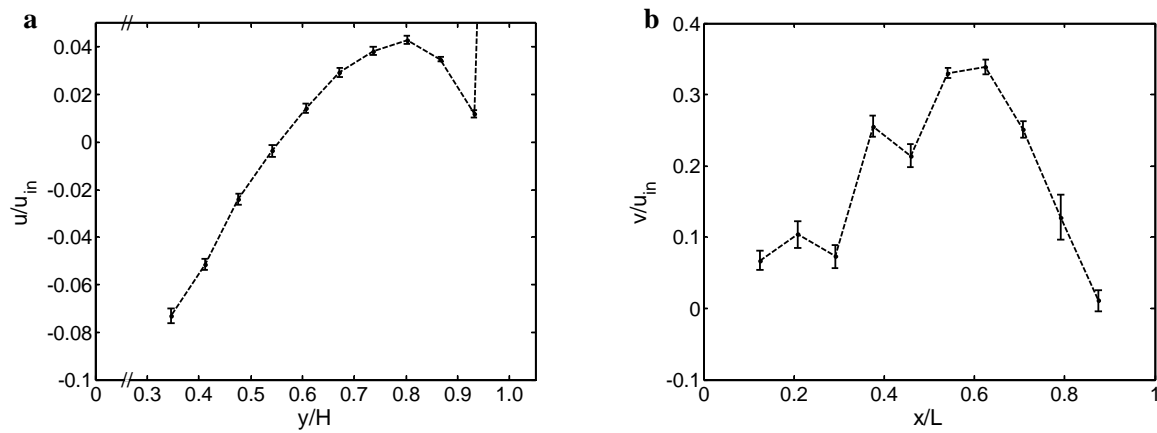
Fig. 45 Velocity profiles with error bars: **a** horizontal velocity component u/u_{in} along y/H at $(x/L, z/D) = (0.0825, 0.5)$ for the isothermal case with $Re = 2.4 \times 10^4$; **b** vertical velocity component v/v_{in} along x/L at $(y/L, z/D) = (0.58, 0.49)$ for the case of mixed convection for the reference set of dimensionless numbers and the 2nd repetition

Both diagrams show that the error of the velocity measurement is nearly constant over the complete profile, especially in the isothermal case in Fig. 45a. For the case of mixed convection the error differs slightly more and the absolute value is also higher compared to the values of the isothermal case. This can

also be found in the values of the velocity and the confidence interval as shown in Tab. 5 and Tab. 6. The tables show the values of the velocity distributions as depicted in Fig. 45a and b. As a result, the absolute error is almost constant for all measurement points, i.e. it do not dependent on the velocity value.

y/H	0.347	0.412	0.477	0.542	0.607	0.672	0.737	0.802	0.867	0.932	0.997
u/u_{in}	-0.073	-0.052	-0.024	-0.004	0.014	0.029	0.038	0.043	0.035	0.012	0.484
$\Delta u/u_{in}$	0.0030	0.0023	0.0023	0.0026	0.0021	0.0019	0.0018	0.0017	0.0010	0.0016	0.0003
$\Delta u/u$	4.1%	4.5%	9.4%	69.7%	14.7%	6.6%	4.7%	3.9%	2.9%	13.4%	0.05%

Tab. 5 Errors of the horizontal velocity u/u_{in} along y/H at $x/L = 0.0825$ and $z/D = 0.5$ for the isothermal case at $Re = 2.4 \times 10^4$

x/L	0.1254	0.2086	0.2919	0.3751	0.4584	0.5416	0.6249	0.7081	0.7914	0.8746
v/u_{in}	0.0673	0.1042	0.0729	0.2556	0.2142	0.3304	0.3386	0.2513	0.1278	0.0113
$\Delta v/u_{in}$	0.0138	0.0187	0.0161	0.0149	0.0160	0.0077	0.0104	0.0116	0.0314	0.0150
$\Delta v/v$	20.5%	17.9%	22.1%	5.8%	7.5%	2.3%	3.1%	4.6%	24.6%	132.9%

Tab. 6 Errors of the vertical velocity v/u_{in} along x/L at $y/L = 0.58$ and $z/D = 0.49$ for the case of mixed convection

The tables give also information about the relative error $\Delta u/u$ and $\Delta v/v$. The relative error amounts to approximately 5%. Only where the absolute value of the velocity tends to zero, the relative error is very high as shown for $y/H = 0.542$ in Tab. 5 or $x/L = 0.8746$ in Tab. 6. Furthermore, the comparison of the relative error between the isothermal and the mixed convection case shows that although there is a deviation of the absolute values, the relative values are nevertheless almost equal.

5 Summary and outlook

In the present work a new experimental method for the investigation of indoor airflows in a reduced scale model room has been developed. This new scaling method has been derived from the similarity theory of mixed convection airflows and provides the possibility to achieve full similarity with respect to the full set of dimensionless numbers. The technical realization of this theoretical approach could be demonstrated by setting up a novel experimental setup, called SCALEX-facility (SCALEX = scaled convective airflow laboratory experiment). Moreover, the feasibility of the new method has been shown by the investigation of the large-scale flow structures of an indoor airflow in a 1:10 scale model room using the new method.

For the case of mixed convection, the new method is based on the manipulation of the material properties of the working gas in order to compensate the geometrical scale factor within the dimensionless numbers Reynolds number Re, Rayleigh number Ra, Prandtl number Pr and Archimedes number Ar. The manipulation is realized by isothermally increasing the pressure p of a working gas. This basically works with every working gas, but in order to achieve high scale factors at a moderate technical effort, sulfur hexafluoride (SF_6) has been used as the working gas. Due to the 5-times higher density of SF_6 with respect to air at ambient pressure, the usage of SF_6 allows reaching very high scale factors of up to 1:20 and even more. A main result of the theoretical consideration of the similarity theory is that although this method is also not able to provide perfect similarity, a partial similarity with very tight tolerances regarding the full set of dimensionless numbers can be achieved for the case of mixed convection. This issue is the main advantage of the new method with respect to hitherto methods.

The successfully technical realization of the new method by setting up the SCALEX-facility has been shown that the technical effort is quite low and comparable to the setup of a wind tunnel. The SCALEX-facility comprises a pressure vessel and a working gas supply. The facility allows the fundamental investigation of small-scale model rooms with arbitrary geometries at constant boundary conditions and a broad range of dimensionless numbers. Moreover, the SCALEX-facility allows the investigation of application-oriented problems of indoor airflows like in a wind tunnel. Another advantage of the SCALEX-facility is the possibility of using common flow measurement techniques.

Investigations of the large-scale flow structures of indoor airflows have been conducted using a 1:10 model room with a comparable complex geometry for the case of mixed convection and for the isothermal case. The small-scale model room has a height of $H = 300mm$ and the aspect ratios $\Gamma_{xy} = 1.33$ and $\Gamma_{zy} = 1.66$. In the mixed convection case the set of dimensionless numbers amounts to $Re = 1.44 \times 10^5$, $Ra = 1.93 \times 10^{10}$, $Pr = 0.9$ and $Ar = 1.03$. The isothermal case was studied for the Reynolds number range

of $1.0 \times 10^4 \leq Re \leq 7.0 \times 10^4$. The large-scale flow structures have been characterized by velocity measurements using a 2D-LDV-system. The flow in the isothermal case is mainly characterized by a 2-dimensional large-scale structure, which is in accordance to the findings reported in open literature. A coherent oscillation of the large-scale flow structure has been found from long term measurements. The origin of this oscillation seems to be the auto-oscillation of two colliding wall-jets, originated from the inlet flow. While the flow structures in the isothermal case are relatively simple, the flow structure in the case of mixed convection is very complex. Although the chosen model room geometry is mainly characterized as 2-dimensional, the flow has a complex 3-dimensional structure. The found flow structure is originated by the superposition of the flow structure found in the isothermal case and the thermal convection arising from the heat input of the heating elements. Furthermore, this complex 3-dimensional flow structure shows a coherent oscillation, which in addition influences the heat flux on the heating elements.

The comparison of the small-scale experiment and a DNS in the isothermal case has been conducted at $Re = 2.4 \times 10^4$ and shows a very high qualitative similarity. The comparison shows relatively high quantitative deviations at positions where the flow velocity is also very low. A difference in the depth of the room in the experiment and the DNS could be found as the main reason for the deviations.

The results of the mixed convection case have been compared to the ones of a full-scale experiment using the same room geometry but with 10-times larges dimensions. The comparison reflects a validation of the new scaling method and show that the flow can be reproduced in the small-scale experiment as well as in the full-scale experiment. The found flow structures are qualitatively identical but show some distinctive deviations in the absolute velocity. The main reason for the deviations might be that in the small-scale experiment the third velocity component w is neglected. Due to the fact that the full-scale experiment only provides the absolute value of the velocity, it was not possible to perform a direct comparison of each velocity component.

So, the validation of the new method should be a main part of the future work and has to be extended to a large variety of boundary conditions and different model room geometries. Particularly the comparison with data accessible in open literature, e.g. data from the Nielsen room, as well as the comparison with high performance numerical simulations might be the most promising way to determine the exact accuracy of the new method. In the near future, the fundamental investigation of the indoor airflow at a broad range of dimensionless numbers seems to be the most reasonable application of the new method and the SCALEX-facility. Other applications might be the investigation of application-oriented questions of indoor airflows like the ventilation problems in the passenger cabin of a new aircraft or a new train. Even the investigation of buildings with complex geometries seems to be a realistic prediction of the application

range. Although designed for the investigation of indoor airflow problems, the SCALEX-facility is not limited to this scope. Moreover, the investigation of fundamental questions concerning the Rayleigh-Bénard-convection in large-aspect-ratio cells is only one future application. The SCALEX-facility also provides the possibility to answer questions regarding heat transfer on complex surfaces or aerodynamic problems of very large structures.

So, the new experimental method for the investigation of indoor airflows in a reduced scale model room provides the possibility to perform small-scale experiments with tight tolerances regarding similarity theory. Moreover, the new method seems to have the potential to raise the significance of small-scale experiments in indoor airflow research. It furthermore has the ability to substitute a lot of expensive full-scale investigations and provides a comprehensive tool for the generation of exact data needed for the validation of all numerical methods. The new method and especially its technical realization in the SCALEX-facility seem to provide similar potentials for the investigation of indoor airflows as a wind tunnel do for aerodynamics. Moreover, the abilities of the SCALEX-facility go far beyond the investigation of indoor airflow problems and will play an important role in a broad range of future studies.

6 References

[1]   P. V. Nielsen, 1974, "Flow in air conditioned rooms", Technical University of Denmark

[2]   A. D. Gosman, P. V. Nielsen, A. Restivo, and J. H. Whitelaw, 1980, "The fow properties of rooms with small ventilation openings", *Journal of Fluids Engineering*, 102, pp. 316–323

[3]   M. Sandberg, 1983, "The use of moments for assessing air quality in ventilated rooms", *Building and Environment*, 18, 4, pp. 181–197

[4]   Q. Chen, 1988, "Indoor airflow, air quality and energy consumption of buildings", TU Delft

[5]   P. F. Linden, G. F. Lane-Serff, and D. A. Smeed, 1990, "Emptying filling boxes: the fluid mechanics of natural ventilation", *Journal of Fluid Mechanics*, 212, pp. 309–335

[6]   P. F. Linden, 1999, "The fluid mechanics of natural ventilation", *Annual Review of Fluid Mechanics*, 31, pp. 201–238

[7]   C. Gladstone and A. W. Woods, 2001, "On buoyancy-driven natural ventilation of a room with a heated floor", *Journal of Fluid Mechanics*, 441, pp. 293–314

[8]   P. Heiselberg and M. Perino, 2010, "Short-term airing by natural ventilation – implication on IAQ and thermal comfort", *Indoor Air*, 20, pp. 126–140

[9]   P. O. Fanger, 2006, "What is IAQ?", *Indoor Air*, 16, 5, pp. 328–334

[10]   P. O. Fanger and N. K. Christensen, 1986, "Perception of draught in ventilated spaces", *Ergonomics*, 29, 2, pp. 215–235

[11]   P. Heiselberg, Y. Li, A. Andersen, M. Bjerre, and Z. Chen, 2004, "Experimental and CFD evidence of multiple solutions in a naturally ventilated building", *Indoor Air*, 14, 1, pp. 43–54

[12]   P. O. Fanger, 1970, "Thermal comfort: analysis and applications in environmental engineering", Copenhagen: Danish Technical Press, pp. 244

[13]   L. Fang, D. P. Wyon, G. Clausen, and P. O. Fanger, 2004, "Impact of indoor air temperature and humidity in an office on perceived air quality, SBS symptoms and performance", *Indoor Air*, 14, 7, pp. 74–81

[14]   D. P. Wyon, 2004, "The effects of indoor air quality on performance and productivity", *Indoor Air*, 14, pp. 92–101

[15]   O. A. Seppänen and W. J. Fisk, 2004, "Summary of human responses to ventilation", *Indoor Air*, 14, 7, pp. 102–118

[16]   P. Strøm-Tejsen, D. P. Wyon, L. Lagercrantz, and L. Fang, 2007, "Passenger evaluation of the optimum balance between fresh air supply and humidity from 7-h exposures in a simulated aircraft cabin", *Indoor Air*, 17, 2, pp. 92–108

[17]   A. Mangili and M. A. Gendreau, 2005, "Transmission of infectious diseases during commercial air travel.," *The Lancet*, 365, 9463, pp. 989–996

[18]   P. O. Fanger, A. K. Melikov, H. Hanzawa, and J. Ring, Apr. 1988, "Air turbulence and sensation of draught," *Energy and Buildings*, 12, 1, pp. 21–39

[19]   R. Krishnamurti and L. N. Howard, 1981, "Large-scale flow generation in turbulent convection", *Proceedings of the National Academy of Sciences of the United States of America*, 78, 4, pp. 1981–1985

[20]   D. Funfschilling, E. Brown, and G. Ahlers, 2008, "Torsional oscillations of the large-scale circulation in turbulent Rayleigh–Bénard convection," *Journal of Fluid Mechanics*, 607, pp. 119–139

[21]   E. Villermaux, 1995, "Memory-induced low frequency oscillation in closed convection boxes," *Physical Review Letters*, 75, 25

[22]   F. Chillà and J. Schumacher, 2012, "New perspectives in turbulent Rayleigh-Bénard convection", *The European physical journal E: Soft matter*, 35, 58

[23]   R. du Puits, 2008, "Wärmetransport in Tubulenten Konvektionsströmungen", Ilmenau University of Technology, Ilmenau

[24]   S. Großmann and D. Lohse, 2000, "Scaling in thermal convection: a unifying theory", *Journal of Fluid Mechanics*, 407, pp. 27–56

[25]   Y. Li and P. V. Nielsen, 2011, "CFD and ventilation research", *Indoor Air*, 21, 6, pp. 442–53

[26]   N. B. Kaye and G. R. Hunt, 2004, "Time-dependent flows in an emptying filling box", *Journal of Fluid Mechanics*, 520, pp. 135–156

[27]   M. Kühn, J. Bosbach, and C. Wagner, 2009, "Experimental parametric study of forced and mixed convection in a passenger aircraft cabin mock-up", *Building and Environment*, 44, 5, pp. 961–970

[28]   D. Schmeling, A. Westhoff, M. Kühn, J. Bosbach, and C. Wagner, 2010, "Flow structure formation of turbulent mixed convection in a closed rectangular cavity", in *New Results in Numerical and Experimental Fluid Mechanics VII*, Springer Berlin Heidelberg, 112, pp. 571–578.

[29]   O. Shishkina, A. Shishkin, and C. Wagner, 2009, "Simulation of turbulent thermal convection in complicated domains", *Journal of Computational and Applied Mathematics*, 226, 2, pp. 336–344

[30]   Q. Chen, 2009, "Ventilation performance prediction for buildings: a method overview and recent applications", *Building and Environment*, 44, 4, pp. 848–858

[31]   E. Lobutova, C. Resagk, and T. Putze, 2010, "Investigation of large-scale circulations in room air flows using three-dimensional particle tracking velocimetry", *Building and Environment*, 45, 7, pp. 1653–1662

[32]   Q. A. Liu and P. F. Linden, 2006, "The fluid dynamics of an underfloor air distribution system", *Journal of Fluid Mechanics*, 554, pp. 323-341

[33] N. B. Kaye and G. R. Hunt, 2007, "Overturning in a filling box", *Journal of Fluid Mechanics*, 576, p. 297

[34] P. F. Linden, 1999, "The fluid mechanics of natural ventilation", *Annual Review of Fluid Mechanics*, 31, pp. 201–238

[35] W. Richter, 2003, "Handbuch der thermischen Behaglichkeit", Dresden: Bundesanstalt für Arbeitsschutz und Arbeitsmedizin

[36] S. B. Pope, 2000, "Turbulent flows", 1st ed., Cambridge University Press, Cambridge

[37] W. A. Stahel, 2008, "Statistische Datenanalyse", 5. ed., Friedr. Vieweg & Sohn Verlag, Wiesbaden

[38] J. L. Lumley, 1970, "Stochastic tools in turbulence", Academic Press, New York

[39] C. Tropea, A. L. Yarin, and J. F. Foss, 2007, "Springer handbook of experimental fluid mechanics", Springer-Verlag, Berlin

[40] E. Buckingham, 1914, "On physically similar systems: illustrations of the use of dimensional equations", *Physical Review*, 4, 4, pp. 345–376

[41] H. Herwig, 2006, "Strömungsmechanik", 2nd ed., Springer-Verlag, Berlin

[42] B. R. Munson, D. F. Young, T. H. Okiishi, and W. W. Huebsch, 2009, "Fundamentals of fluid mechanics", 6th ed., John Wiley & Sons, Hoboken, pp. 784

[43] S. Solomon, D. Qin, M. Manning, Z. Chen, M. Marquis, K. B. Averyt, M. Tignor, and H. L. Miller, 2007, "Climate Change 2007: The physical science basis", Cambridge University Press, New York, p. 996

[44] D. Funfschilling, E. Bodenschatz, and G. Ahlers, 2009, "Search for the 'Ultimate State' in turbulent Rayleigh-Bénard convection", *Physical Review Letters*, 103, 1

[45] J. R. de Bruyn, E. Bodenschatz, S. W. Morris, S. P. Trainoff, Y. Hu, D. S. Cannell, and G. Ahlers, 1996, "Apparatus for the study of Rayleigh–Bénard convection in gases under pressure", *Review of Scientific Instruments*, 67, 6, p. 2043

[46] M. Assenheimer and V. Steinberg, 1994, "Transition between spiral and target states in Rayleigh–Bénard convection," *Nature*, 367, 6461, pp. 345–347

[47] G. Ahlers, D. Funfschilling, and E. Bodenschatz, 2009, "Transitions in heat transport by turbulent convection at Rayleigh numbers up to 10^{15}", *New Journal of Physics*, 11, 12

[48] K. Kadoya, N. Matsunaga, and A. Nagashima, 1985, "Viscosity and thermal conductivity of dry air in the gaseous phase," *Journal of Physical and Chemical Reference Data*, 28, 3, pp. 947–970

[49] E. W. Lemmon, 2000, "Thermodynamic properties of air and mixtures of nitrogen, argon, and oxygen from 60 to 2000K at pressures to 2000MPa", *Journal of Physical and Chemical Reference Data*, 29, 3, p. 331

[50] J. Kestin and N. Imaishi, 1985, "Thermal conductivity of sulfur hexafluoride," *International Journal of Thermophysics*, 6, 2

[51] J. H. B. Hooghland, H. R. Van Den Berg, and N. J. Trappeniers, 1985, "Measurements of the viscosity of sulfur hexafluorid up to 100bar by a capillary-flow viscometer", *Physica A*, 134, pp. 169–192

[52] C. Guder and W. Wagner, 2009, "A reference equation of state for the thermodynamic properties of sulfur hexafluoride (SF_6) for temperatures from the melting line to 625K and pressures up to 150MPa", *Journal of Physical and Chemical Reference Data*, 38, 1, p. 33

[53] E. W. Lemmon, M. O. McLinden, and D. G. Friend, "Thermophysical properties of fluid systems", in *NIST Chemistry WebBook, NIST Standard Reference Database Number 69*, P. J. Linstrom and W. G. Mallard, Eds., National Institute of Standards and Technology, Gaithersburg MD, (retrieved November 14, 2012)

[54] A. Thess and C. Wagner, 2009, "Verfahren und Anordnung zur Nachbildung einer Raumluftströmung", German Patent, DE102006009646A1, (submitted 2007, granted 2009)

[55] Y. Tridimas, M. J. Lalor, and N. H. Woolley, 1978, "Beam waist location and measurement in a dual-beam laser Doppler anemometer", *Journal of Physics E*, 11, pp. 203–206

[56] P. V. Nielsen, A. Restivo, and J. H. Whitelaw, 1978, "The velocity characteristics of ventilated rooms," *Journal of Fluids Engineering*, 100, pp. 291–299

[57] C. Kandzia, M. Schmidt, and D. Müller, 2011, "Room airflow effects applying unsteady boundary conditions," in *Proceedings of the 12th International Conference on Air Distribution in Rooms*

[58] M. Körner, O. Shishkina, C. Wagner, and A. Thess, 2013, "Properties of large-scale flow structures in an isothermal ventilated room," *Building and Environment*, 59, pp. 563–574

[59] V. A. Denshchikov, V. N. Kondrat'ev, and A. N. Romashov, 1978, "Interaction between two opposed jets," *Fluid Dynamics*, 13, 6, pp. 924–926

[60] V. A. Denshchikov, V. N. Kondrat'ev, A. N. Romashov, and V. M. Chubarov, 1983, "Auto-oscillations of planar colliding jets", *Fluid Dynamics*, 18, 3, pp. 460–462

[61] R. P. Pawlowski, a. G. Salinger, J. N. Shadid, and T. J. Mountziaris, 2006, "Bifurcation and stability analysis of laminar isothermal counterflowing jets", *Journal of Fluid Mechanics*, 551, p. 117

[62] S. C. Crow, 1970, "Stability theory for a pair of trailing vortices", *AIAA Journal*, 8, 12, pp. 2172 – 2179

[63] T. Leweke and C. H. K. Williamson, 1998, "Cooperative elliptic instability of a vortex pair", *Journal of Fluid Mechanics*, 360, pp. 85–119

[64] R. T. Pierrehumbert, 1986, "Universal short-wave instability of two-dimensional eddies in an inviscid fluid", *Physical Review Letters*, 57, 17, pp. 2157–2160

A   Calculation of the material properties

The following sections describe the calculation procedures of the material properties and can be regarded as a basis for determining the material properties for future studies. The used equations are mainly based on empirical equations found by experimental research and are at least valid for the temperature and pressure range of the SCALEX-facility, $273.15\text{K} \leq T \leq 343.15\text{K}$ and $1\text{bar} \leq p \leq 10\text{bar}$. The documented material properties are the density ρ, the heat conductivity λ, the volume expansion coefficient β, the dynamic viscosity η and the heat capacity c_p.

A.1   Material properties of dry air

A.1.1 Density $\rho(p,T)$

The calculation of the density of dry air is based on the equation of state for an ideal gas, which reads as follows

$$\rho = \frac{p}{RT} \tag{46}$$

with p as the gas pressure, T as the gas temperature and $R = 287.058 \text{Jkg}^{-1}\text{K}^{-1}$ as the specific gas constant.

A.1.2 Heat conductivity $\lambda(\rho,T)$

The calculation of the heat conductivity λ is based on the empirical equations formulated by [48] and reads as follows

$$\lambda(\rho,T) = \Lambda\left(\lambda_0(T_r) + \Delta\lambda(\rho_r)\right) \tag{47}$$

where

$$\lambda_0(T_r) = C_1 T_r + C_{0.5} T_r^{0.5} + \sum_{i=0..-4} C_i T_r^i \tag{48}$$

and

$$\Delta\lambda(\rho_r) = \sum_{i=1..5} D_i \rho_r^{\,i} \tag{49}$$

The reduced values of the density and the temperature are defined by

$$T_r = \frac{T}{T^*} \tag{50}$$

and

$$\rho_r = \frac{\rho}{\rho^*} \tag{51}$$

with $\rho^* = 314.5\,\mathrm{kgm^{-3}}$ and $T^* = 132.5\,\mathrm{K}$ as the critical density and the critical temperature, respectively. According to [48], the coefficients are defined as shown in Tab. 7.

C_{-4}	0.229414
C_{-3}	-1.07553
C_{-2}	2.00383
C_{-1}	-1.92615
C_0	1
$C_{0.5}$	0.00649768
C_1	0.239503
D_1	0.402287
D_2	0.356603
D_3	-0.163159
D_4	0.138059
D_5	-0.0201725
Λ	$25.9778 \times 10^{-3}\,\mathrm{Wm^{-1}K^{-1}}$

Tab. 7 Coefficients for the calculation of the heat conductivity of air

A.1.3 Specific heat capacity $c_p(\rho, T)$

The calculation of the specific heat capacity $c_p(\rho, T)$ is based on empirical equations formulated by [49] and reads as follows

$$c_p(T) = R\left[\sum_{i=1..5} N_i T^{i-1} + N_3 T^{1.5} + N_6 u^2 e^u \left(e^u - 1\right)^{-2} + N_7 v^2 e^v \left(e^v - 1\right)^{-2} + \frac{2}{3} N_8 w^2 e^{-w} \left(\frac{2}{3} e^{-w} + 1\right)^{-2} \right] \tag{52}$$

with

$$u = \frac{N_9}{T}, \quad v = \frac{N_{10}}{T}, \quad w = \frac{N_{11}}{T}. \tag{53}$$

According to [49] the coefficients are defined as listed in Tab. 8.

N_1	3.49088032
N_2	2.4×10^{-6}
N_3	7.17×10^{-9}
N_4	-3.12×10^{-13}
N_5	2.24×10^{-1}
N_6	7.91×10^{-1}
N_7	2.12×10^{-1}
N_8	1.98×10^{-1}
N_9	3.36×10^{3}
N_{10}	2.24×10^{3}
N_{11}	1.16×10^{4}

Tab. 8 Coefficients for the calculation of the specific heat capacity $c_p(T)$

A.1.4 Dynamic viscosity $\eta(\rho, T)$ of air

Calculation of the dynamic viscosity $\eta(\rho, T)$ is based on empirical equations formulated by [48] and reads as follows

$$\eta(\rho, T) = H\left(\eta_0\left(T_r\right) + \Delta\eta\left(\rho_r\right)\right) \tag{54}$$

where

$$\eta_0\left(T_r\right) = A_1 T_r + A_{0.5} T_r^{0.5} + \sum_{i=0..-4} A_i T_r^{i} \tag{55}$$

$$\Delta\eta\left(\rho_r\right) = \sum_{i=1..4} B_i \rho_r^{i} . \tag{56}$$

According to [48], the coefficients are defined as shown in Tab. 9.

A_{-4}	0.00770147
A_{-3}	-0.197846
A_{-2}	0.662534
A_{-1}	-0.709661
A_0	-1
$A_{0.5}$	2.60661
A_1	0.128517
B_1	0.465601
B_2	1.26469
B_3	-0.511425
B_4	0.2746
H	6.16×10^{-6}

Tab. 9 Coefficients for the calculation of the dynamic viscosity $\eta(\rho, T)$ of air

A.1.5 Volume expansion coefficient $\beta(T)$ of air

The volume expansion coefficient for an ideal gas is defined as follows

$$\beta(T) = \frac{1}{T} \tag{57}$$

and thus independent with respect to the density ρ.

A.2 Calculation of the material properties of SF$_6$

The calculation of the material properties of SF$_6$ is mainly based on the multi-parameter equations of state developed by [52]. Due to its complexity of the coefficients and their derivatives only the basic equations are documented in the following.

A.2.1 Density $\rho(p,T)$

The determination of the density $\rho(p, T)$ of SF$_6$ is based on the multi-parameter equation of state found by [52] and can be calculated by using

$$\rho(p,T) = \frac{p}{RT\left(1 + \delta\alpha_\delta^r\right)} \tag{58}$$

with p as the working gas pressure, T the working gas temperature and $R = 5.69268987\,\mathrm{Jkg^{-1}K^{-1}}$ as the specific gas constant for SF_6. Furthermore, δ is the reduced density

$$\delta = \frac{\rho(p,T)}{\rho_c} \tag{59}$$

with $\rho_c = 742.3\,\mathrm{kgm^{-3}}$ and α_δ^r is the 1st-order derivative with respect to δ of the residual part of the Helmholtz energy equation [52]. Due to its non-closed-form, eq. (58) has to be solved iteratively.

A.2.2 Specific heat capacity $c_p(\rho, T)$

The calculation of the specific heat capacity of SF_6 is also based on the multi-parameter equations found by [52] and reads as follows

$$c_p(\delta,\tau) = R\left(-\tau^2\left(\alpha_{\tau\tau}^0 + \alpha_{\tau\tau}^r\right) + \frac{\left(1 + \delta\alpha_\delta^r - \delta\tau\alpha_{\delta\tau}^r\right)^2}{1 + 2\delta\alpha_\delta^r + \delta^2\alpha_{\delta\delta}^r}\right) \tag{60}$$

with τ as the inverse reduced temperature, defined as

$$\tau = \frac{T_c}{T} \tag{61}$$

with $T_c = 318.7232\,\mathrm{K}$ as the critical temperature of SF_6 [52]. The variables α_{ij}^0 and α_{ij}^r are the derivatives with respect to δ and τ of the ideal-gas and residual part of the Helmholtz energy equation, respectively.

A.2.3 Heat conductivity $\lambda(\rho, T)$

The determination of the heat conductivity of SF_6 is based on the empirical equation of [50] and reads

$$\lambda(p,T) = \sum_{i=1}^{3} a_{\lambda i}\rho^i + \lambda(T) \tag{62}$$

with

$$\lambda(T) = a_{\lambda 1*}\left(1 + a_{\lambda 2*}\left(\left(T - 273.15K\right) + a_{\lambda 3*}\right)\right) \tag{63}$$

and $a_{\lambda i}$ and $a_{\lambda i*}$ as its coefficients as documented in Tab. 10.

i	$a_{\lambda i}$	$a_{\lambda i*}$
1	1.100×10^{-5}	1.301×10^{-2}
2	-7.615×10^{-9}	5.490×10^{-3}
3	2.887×10^{-10}	-27.50

Tab. 10 Coefficients a_{λ} of the empirical equations $\lambda(p,T)$ and $\lambda(p,T)$ [Eq. (62) and (63)]

A.2.4 Dynamic viscosity $\eta(\rho,\ T)$

The dynamic viscosity is determined by using the empirical equation of [51], which is defined as follows

$$\eta(p,T) = \sum_{i=1}^{7} a_{\eta i}\rho^{i} + \eta(T) \tag{64}$$

with

$$\eta(T) = e^{\left(a_{\eta 1*}\log(T) + a_{\eta 2*}T^{-1} + a_{\eta 3*}T^{-2} + a_{\eta 4*}\right)} \tag{65}$$

The coefficients $a_{\eta i}$ and $a_{\eta i*}$ are documented in Tab. 11 according to the findings of [51].

i	$a_{\eta i}$	$a_{\eta i*}$
1	1.386500×10^{-2}	0.51460
2	2.850990×10^{-3}	-190.10
3	-4.168480×10^{-5}	10500
4	6.446345×10^{-7}	0.31140
5	-4.997040×10^{-9}	
6	1.970048×10^{-11}	
7	$-2.961807 \times 10^{-14}$	

Tab. 11 Coefficients a_η of the empirical equations $\eta(p,T)$ and $\eta(T)$ [Eq. (64) and (65)]

A.2.5 Volume expansion coefficient $\beta(T)$

The volume expansion coefficient of SF_6 is determined by

$$\beta(T) = -\frac{1}{\rho(T)}\left(\frac{d\rho(T+dT)}{dT}\right) \tag{66}$$

with $d\rho = \rho(T + dT) - \rho(T)$ as a very small density change, which is calculated by applying a temperature difference to the working gas of $dT = 0.5K$. Thus, the volume expansion coefficient of SF_6 has a density dependency.

Erklärung

(gemäß Anlage 1 der Siebten Änderung der Promotionsordnung der TU Ilmenau – Allgemeine Bestimmungen)

Ich versichere, dass ich die vorliegende Arbeit ohne unzulässige Hilfe Dritter und ohne Benutzung anderer als der angegebenen Hilfsmittel angefertigt habe. Die aus anderen Quellen direkt oder indirekt übernommenen Daten und Konzepte sind unter Angabe der Quelle gekennzeichnet.

Bei der Auswahl und Auswertung folgenden Materials haben mir die nachstehend aufgeführten Personen in der jeweils beschriebenen Weise unentgeltlich geholfen:

1. ....Dr. rer. nat. Christian Resagk (Diskussion zu Aspekten einzelner Ergebnisse, des Experimentaufbaus und der Datenauswertung)
2. ....Dr.-Ing. habil. Ronald du Puits (Diskussion zu Aspekten einzelner Ergebnisse, des Experimentaufbaus und der Datenauswertung)
3. ……Prof. Dr. rer. nat. habil. André Thess (Diskussion zu Aspekten einzelner Ergebnisse, des Experimentaufbaus und der Datenauswertung)
4. ……Technische Mitarbeiter: Dipl.-Ing. Klaus Henschel, Dipl.-Ing. Helmut Hoppe, Dipl.-Ing. Vigimantas Mitschunas (Hilfe beim experimentellen Aufbau sowie bei der Datenauswertung)
5. ……Studentische Hilfskräfte: Markus Schmolinsky, Bernd Höhn, Christian Eisele (Hilfe beim experimentellen Aufbau sowie bei der Datenauswertung)

Weitere Personen waren an der inhaltlich-materiellen Erstellung der vorliegenden Arbeit nicht beteiligt. Insbesondere habe ich hierfür nicht die entgeltliche Hilfe von Vermittlungs- bzw. Beratungsdiensten (Promotionsberater oder anderer Personen) in Anspruch genommen. Niemand hat von mir unmittelbar oder mittelbar geldwerte Leistungen für Arbeiten erhalten, die im Zusammenhang mit dem Inhalte der vorgelegten Dissertation stehen. Die Arbeit wurde bisher weder im In- noch im Ausland in gleicher oder ähnlicher Form einer Prüfungsbehörde vorgelegt. Ich bin darauf hingewiesen worden, dass die Unrichtigkeit der vorstehenden Erklärung als Täuschungsversuch bewertet wird und gemäß § 7 Abs. 10 der Promotionsordnung den Abbruch des Promotionsverfahrens zur Folge hat.

Ilmenau, 22.03.2013